AN ABSTRACT OF THE THESIS OF

Jason Michael Dorfman for the degree of Master of Science in Ocean, Earth and Atmospheric Sciences presented on May 17, 2013.

Title: A 37,000-year Record of Paleomagnetic and Environmental Magnetic Variability from Burial Lake, Arctic Alaska

Abstract approved:

_____

Joseph S. Stoner

Burial Lake sediments from the Noatak Basin in the northwest Brooks Range of Arctic Alaska (68.43°N, 159.17°W, 21.5 m water depth) provide the oldest continuous lacustrine record of paleo-environmental change and paleomagnetic secular variation (PSV) in eastern Beringia. A precise radiocarbon chronology, determined through accelerator mass spectrometry (AMS) allows us to independently constrain the region's climatic and geomagnetic evolution over the last ~37,000 years. Progressive alternating field (AF) demagnetization of u-channel samples and additionally acquired physical, geochemical, and rock-magnetic datasets, reveal three distinct lithologic subunits associated with the last glacial period (37.2 – 19.4 ka), the deglacial transition (19.4 – 9.8 ka), and the Holocene (9.8 ka – present).

Rock magnetic variability suggests changes in sediment provenance associated with the transition from glacial to interglacial conditions. This is interpreted to result from a variable flux of aeolian derived sediment, and is supported by complimentary internal proxy data from Burial Lake. Other regional paleoclimate data, various glacial chronologies for the Brooks Range, and a relative sea level reconstruction facilitate a discussion of possible local, widespread, and far-field sources of dust, and the time-dependency of potential forcing mechanisms governing its production, availability, transport, and deposition. Results indicate an overall reduction in dust input from the

glacial period to the Holocene that is largely attributed to increases in terrestrial and aquatic productivity, warming, and moisture availability, which limited widespread landscape deflation and production of dust. Subaerial continental shelves may have provided significant far-field sources of dust to interior Alaska during the glacial period, that were shut off by sea level inundation following the Last Glacial Maximum (LGM; 19 – 26.5 ka), further contributing to diminishing dust emissions. While glacial activity in the Brooks Range may provide local revenue of dust, activation of those deposits and timing of deposition in Burial Lake often appears to be more directly linked with general aridity, lack of vegetative cover, and increased windiness, rather than glacial advances or retreats.

Despite this lithologic complexity, we isolate a stable, single-component characteristic remanent magnetization, carried predominately by low-coercivity (titano)magnetite in the pseudo single-domain (PSD) to multi-domain (MD) magnetic grain size range. We reconstruct directional paleomagnetic secular variation (PSV) over the full length of the record, and relative paleointensity (RPI) for the last ~14,700 years, which are consistent with available regional PSV records and continuous spherical harmonic model outputs. We observe only small deviations from geocentric axial dipole (GAD) predictions during the Holocene, while larger amplitude directional features are prevalent before 10 ka, and inclinations lay significantly shallower than GAD. While this may be related to lithology and the sediment magnetic acquisition process, regional records (including those derived from lava flows) indicate similar Holocene-Pleistocene discrepancies. Following on the "eccentric dipole" hypothesis, subdued secular variation and GAD-like behavior in the Pacific appears confined to the Holocene high-intensity state, showing greater variability as Pleistocene field strength diminishes, and/or the dipole axis is shifted away from the Pacific hemisphere. Long period trends in PSV from in the Alaskan Arctic are also similar in character to far-field sites (e.g., Hawaii and Siberia), suggesting large-scale coherent core-fluid flow regimes, expressed over surface geographical extents >5,000 km, and spanning Holocene-Pleistocene time intervals. The well-dated Burial Lake record fills a significant data gap in the growing Holocene paleomagnetic database, while allowing us to extend our understanding of PSV beyond

the Holocene and into the Pleistocene, and continue the development of regional stratigraphic dating curves.

A 37,000-year Record of Paleomagnetic and Environmental Magnetic Variability from Burial Lake, Arctic Alaska

by

Jason Michael Dorfman

A THESIS

submitted to

Oregon State University

in partial fulfillment of
the requirements for the
degree of

Master of Science

Presented May 17, 2013
Commencement June 2014

Master of Science thesis of Jason Michael Dorfman presented on May 17, 2013

APPROVED:

_____

Major Professor, representing Ocean, Earth, and Atmospheric Sciences

_____

Dean of the College of Earth, Ocean, and Atmospheric Sciences

_____

Dean of the Graduate School

I understand that my thesis will become part of the permanent collection of Oregon State University libraries. My signature below authorizes release of my thesis to any reader upon request.

_____

Jason Michael Dorfman, Author

ACKNOWLEDGMENTS

This research endeavor would not have been made possible without the tremendous help and inspiration from a number of incredible people in my life. I would like to take this opportunity to thank them for their extraordinary support throughout the completion of this thesis, during my time here in Corvallis, and in many places along the road. I am truly grateful…

To my advisor, Dr. Joseph Stoner, for providing me with the opportunity to carry out this research and for bringing me to Oregon. I thank you for your scientific input, your patience, your unwavering support and guidance, and your confidence in my abilities. Thank you for teaching me about paleo and environmental magnetism, the geosciences in general, and for furthering my scientific career. Thank you for the amazing opportunities for travel and fieldwork, which have allowed me visit some of the more beautiful, remote, and mosquito-infested regions on this Earth.

To the members of my committee, Dr. Alan Mix, Dr. Anders Carlson, and Dr. Ed Peachey, for your valuable inputs and comments to this manuscript.

To the National Science Foundation, for funding this research under the grant number: NSF-ARC 0909545.

To the many wonderful faculty and staff here at Oregon State University and the College of Earth, Ocean, and Atmospheric Sciences, who have taught me so much and were so helpful along the way. Thank you to Mysti Weber, Maziet Cheseby, and Bobbi Conard at the OSU Marine Geology Repository for their frequent help with coring-related projects. I also thank Dr. Anthony Koppers for allowing me to participate briefly in his research at sea, and for refreshing my interest in petrology.

To Dr. Mark Abbott and Matt Finkenbinder at the University of Pittsburgh, for your enormous contributions to this work and your tireless efforts to help resolve the Burial Lake paleo-environmental record. I have truly enjoyed collaborating with your lab group over the years, and I appreciate the summer fieldwork opportunities you have provided. Working with you has been truly gratifying.

To Dr. Nathan Stansell at the Byrd Polar Research Center at The Ohio State University, for your assistance during the 2010 field season at Burial Lake. This study would not have been possible without your hard work.

To Guillaume St-Onge, Jacques Labrie, and the lab group at the *Institut des Sciences de la Mer de Rimouski*, in Quebec, for providing me with the opportunity to conduct research at your lab, and for assisting with many of the physical, geochemical, and magnetic measurements and data processing that were crucial in piecing together the Burial Lake sedimentary record. Our collaboration has been truly rewarding. I also thank the staff at the *Institute national de la recherché scientifique, Centre Eau Terre Environement*, in Quebec City for their assistance in CT-scanning my u-channels.

To Dr. Bernard Housen and Russell Bermester at the Pacific Northwest Paleomagnetism Laboratory at Western Washington University, for the use of your laboratory equipment, the measurements from which proved to be crucial for revealing some of the finer details of the Burial Lake sedimentary record.

To my supportive community of peers, friends, and housemates in Oregon and Corvallis – this is a wonderful place, and your friendship and support has made it feel like home. I have had countless adventures, good times, and memories from the past three years, and I hope I can continue to add to them in the coming years. I owe Jeff Beeson and Morgan Erhardt special thanks for their incredible friendship, as well as their cartographical expertise, which helped produce some of the maps in this manuscript.

To Rob Hatfield, Sarah Strano, Chuang Xuan, Leah Ziegler, and Mo Davies at the P-Mag Lab here at OSU – I owe you a tremendous amount of gratitude for your help, insights, friendship, and support. You have contributed more than you can imagine towards this achievement, and continue to be a constant force behind my successes.

To Claire – you have been a source of strength and inspiration throughout my life, particularly in the challenging weeks and months leading up to this moment. The love and support you have given me has been instrumental in allowing me to flourish throughout the final chapters of this thesis. You have been by my side every step of the way, and your care and encouragement has been infinitely comforting. You have enriched my life in more ways than I can express in words. I love you, and you deserve my sincerest admiration for all your continued support.

Lastly, to my family, especially my Mom and Dad and sister, Karen – your unconditional love and support has been influential in keeping me on track and motivating me throughout this journey. You have instilled in me a wonderful set of ideals and values, which I strive to incorporate in my every day existence. I more than appreciate your presence in my life, and invite you to view the results of this thesis and the sum of my accomplishments as your own.

CONTRIBUTION OF AUTHORS

Joseph Stoner and Mark Abbott secured funding for this project from the National Science Foundation (grant number: NSF-ARC 0909545), and were responsible for most of the logistical issues regarding the 2010 field expedition to Burial Lake, and subsequent sediment core sampling and measurement plans. Joseph Stoner served a primary advisory role, overseeing every step of the work presented herein, and contributing substantially to all scientific and literary efforts - specifically with respect to the u-channel paleomagnetic and environmental magnetic aspects of this project. Mark Abbott oversaw select physical, geochemical, magnetic, and radiocarbon measurements, and contributed intellectually to the paleo-environmental interpretation of data. He also contributed to the editing process of Chapters 2 and 3.

Matt Finkenbinder generously measured and provided select physical, geochemical, and magnetic data, and was the main contributor to radiocarbon measurements and results. He also contributed intellectually to the stratigraphic interpretation of the Burial Lake record, to the paleo-environmental interpretation of data, and to the editing process of Chapters 2 and 3.

Chuang Xuan generated the MATLAB™ code for optimizing the paleomagnetic component directional and relative paleointensity data in Chapter 3, and contributed intellectually to some of the more quantitative aspects of this project.

Guillaume St-Onge facilitated select physical, geochemical, and magnetic measurements through the use of his laboratory equipment, and coordinated the CT-scanning of u-channels. He also provided the physical grain size data in Chapter 2.

TABLE OF CONTENTS

Page

1. INTRODUCTION 1

1.1 THESIS MOTIVATIONS AND APPROACH 1

1.2 BACKGROUND 2

1.2.1 The Earth's Magnetic Field 2

1.2.2 Paleomagnetism 3

1.2.3 Environmental Magnetism 5

1.3 REFERENCES 6

2. A 37,000-YEAR ENVIRONMENTAL MAGNETIC RECORD OF AEOLIAN DUST DEPOSITION FROM BURIAL LAKE, ARCTIC ALASKA 8

2.1 ABSTRACT 9

2.2 INTRODUCTION 10

2.3 REGIONAL SETTINGS 11

2.4 METHODS 12

2.4.1 Field Methods 12

2.4.2 Physical and Geochemical Analyses 13

2.4.3 Rock Magnetic Measurements 13

2.4.4 A10/C10 Composite Depth Scale 16

2.5 AGE-MODEL 16

2.6 RESULTS 17

2.6.1 Sedimentology and Lithostratigraphy 17

2.6.2 IRM Acquisition/Decomposition Results 21

2.7 DISCUSSION 23

2.7.1 Lithologic Interpretation 23

2.7.2 Local and Far-field Sources of Dust, Timing of Deposition, and Potential Forcing Mechanisms 26

2.8 CONCLUSIONS 35

2.9 REFERENCES 36

TABLE OF CONTENTS (Continued)

Page

3. A 37,000-YEAR RECORD OF PALEOMAGNETIC SECULAR VARIATION FROM BURIAL LAKE, ARCTIC ALASKA 56
3.1 ABSTRACT 57
3.2 INTRODUCTION 58
3.3 REGIONAL SETTING 59
3.4 METHODS 60
3.4.1 Field Methods 60
3.4.2 Magnetic Methods 61
3.4.3 Physical Analysis 63
3.4.4 A10/C10 Composite Depth Scale 63
3.5 AGE-MODEL 64
3.6 RESULTS 65
3.6.1 Lithostratigraphy 65
3.6.2 Natural Remanent Magnetization 68
3.6.3 Paleomagnetic Directional Results 68
3.6.4 Normalized Remanence / Relative Paleointensity 70
3.7 DISCUSSION 73
3.7.1 Holocene Paleomagnetic Secular Variation in the Alaskan Arctic 73
3.7.2 Paleomagnetic Secular Variation from the Greater High-latitude Pacific over the last 40 ka 75
3.7.3 Holocene-Pleistocene Geomagnetic Disparities 77
3.8 CONCLUSIONS 79
3.9 REFERENCES 80
4. GENERAL CONCLUSIONS AND FUTURE DIRECTIONS 104
4.1 THESIS SUMMARY 104
4.2 ENVIRONMENTAL MAGNETIC CONCLUSIONS AND FUTURE DIRECTIONS 104
4.3 PALEOMAGNETIC CONCLUSIONS AND FUTURE DIRECTIONS 107
4.4 REFERENCES 109
BIBLIOGRAPHY 112

TABLE OF CONTENTS (Continued)

Page

APPENDIX 125

Appendix A – A10/C10 stratigraphic comparison and composite depth scale construction diagram 126

LIST OF FIGURES

Figure Page

Figure 2.1 Site location map 44

Figure 2.2 AMS radiocarbon results based on terrestrial macrofossils identified in deep basin cores A10 and C10, which were stratigraphically correlated to produce a composite depth scale (see Appendix A) 45

Figure 2.3 Down-core physical, geochemical, and magnetic properties versus depth 46

Figure 2.4 Hysteresis results 47

Figure 2.5 Representative normalized IRM acquisition curves from Subunit 1 (H: 474 cm, 26.965 ka), Subunit 2 (E: 190 cm, 13.526 ka), and Subunit 3 (A: 40 cm, 2.331 ka) 48

Figure 2.6 Left column: IRM decomposition results based on smoothed data from Figure 2.5 49

Figure 2.7 R^2 correlation of smoothed input data to the sum of one, two, three, and four components for samples H, E, and A, representing Subunits 1, 2, and 3, respectively 50

Figure 2.8 Down-core physical, geochemical, and magnetic properties versus age ..51

Figure 2.9 Comparison of Burial Lake S-Ratios with proxy data for regional paleoclimate, glacial history of the Brooks Range, and relative sea level shown on a calibrated age scale 52

LIST OF FIGURES (Continued)

Figure Page

Figure 2.10 Paleo-shoreline map of Beringia showing sea level rise and inundation of Beringian continental shelves from the LGM sea level low-stand (~21 ka) to present 53

Figure 3.1 Site location map 88

Figure 3.2 AMS radiocarbon results based on terrestrial macrofossils identified in deep basin cores A10 and C10, which were stratigraphically correlated to produce a composite depth scale (see Appendix A) 89

Figure 3.3 Down-core physical and magnetic results subdivided into lithologic subunits according to Dorfman et al., (*in prep*) 90

Figure 3.4 Representative normalized IRM acquisition curves from Subunit 1 (H: 474 cm, 26.965 ka), Subunit 2 (E: 190 cm, 13.526 ka), and Subunit 3 (A: 40 cm, 2.331 ka 91

Figure 3.5 Left column: IRM decomposition results based on smoothed data from Figure 3.4.....92

Figure 3.6 Hysteresis results 93

LIST OF FIGURES (Continued)

Figure Page

Figure 3.7 A) Down-core paleomagnetic results versus depth: (From left to right) Natural remanent magnetization (NRM) with AF demagnetization steps ranging from 10-80 mT (plotted on a log scale), NRM_{30mT}/NRM_{0mT} demagnetization ratios, maximum angular deviation (MAD) values, component Inclinations with the geocentric axial dipole (GAD) prediction for site latitude (dashed red line), and component Declinations rotated to a mean 0° 94

Figure 3.8 Normalized remanence results and corresponding R-values for NRM/ARM (A) and NRM/IRM (B) versus depth, based on the slope method calculations for the "consecutive-range" (solid orange lines) and "optimized" (dashed blue lines) approaches (see text for details) 96

Figure 3.9 Full-vector regional comparison of Holocene PSV records the Alaskan Arctic placed on their own chronologies 98

Figure 3.10 Full-vector regional comparison of Holocene PSV records North America placed on their own chronologies 100

Figure 3.11 Regional comparison of directional PSV records the Alaskan Arctic and broader high-latitude Pacific placed on their own chronologies for the period 40 ka to present 101

Figure 4.1 Particle size-specific hysteresis results for representative samples in Subunit 3 (A: 40 cm, 2.331 ka), Subunit 2 (E: 190 cm, 13.526 ka), and Subunit 1 (H: 474 cm, 26.965 ka), corresponding to the Holocene, deglacial transition, and glacial period, respectively 111

LIST OF TABLES

Table | Page

Table 2.1 AMS radiocarbon results based on terrestrial macrofossils identified in deep basin cores A10 and C10, which were stratigraphically correlated to produce the composite depth scale 54

Table 2.2 Summary of IRM decomposition results for samples A-I assuming a two component model 55

Table 3.1 AMS ^{14}C results based on terrestrial macrofossils identified in deep basin cores A10 and C10, which were stratigraphically correlated using physical, geochemical, and magnetics data to produce a common depth scale (see Appendix A) 102

Table 3.2 Root mean square (RMS) results for various inclination anomaly records presented in this study 103

A 37,000-year record of Paleomagnetic and Environmental Magnetic Variability from Burial Lake, Arctic Alaska

Chapter 1

Introduction

1.1 Thesis Motivations and Approach

This thesis comprises an attempt to understand the last ~37,000 years of paleo-environmental and paleomagnetic variability as recorded in sediments from Burial Lake, Arctic Alaska. The Arctic provides a unique vantage point for studying these topics, as it is particularly sensitive to changes in both the geomagnetic field (Cox, 1970) and climate-related processes (Bradley, 1999). Despite increased focus in both these realms in recent decades, the Arctic still remains a remote and relatively understudied region of the world.

The magnetic properties of Burial Lake sediments provide a rather unique perspective on the drastic changes that have occurred in the region over the last millennia, and compliment more traditionally investigated physical and geochemical properties that are often studied in order to decipher sedimentary records. Over the last 37,000 years, glaciers and ice-sheets have come and gone, sea level has fallen and now continues to rise, and landscapes once devoid of vegetation, now show signs of life. Wind, rivers, ocean currents, and ice continue to move vast quantities of sediment through the air and over the surface of the Earth from source to sink. Each particle carries with it a "life history" – a geological narrative of its trials and tribulations experienced along the way, and a distinctive geologic signature of its place of origin. Eventually these particles come to rest, either in the bottom of lakes, the depths of the ocean, or in drifts upon the landscape. It is here that the geologic narrative is preserved, layer-by-layer, as sediments accumulate over time. Through all of this, the molten outer core of the Earth continues to roil and churn, casting invisible lines of magnetic flux towards the surface of the Earth and far out into space. The sediments, of course, do not escape the influence of this dancing magnetic web, and are often aligned by its magnetic

power and locked in place by the burden of overlying sediments, thus capturing the past motions of the core as snapshot moments in time.

In Chapter 1, we provide a brief background on the Earth's magnetic field, as well as a short introduction into the topics of Paleomagnetism and Environmental Magnetism – two branches of science that allow us to interpret the Burial Lake sedimentary record, and extract valuable information regarding the region's geomagnetic and climatic evolution. In Chapter 2, we provide a detailed physical, geochemical, and environmental magnetic investigation of the Burial Lake sedimentary record, commenting specifically on the paleo-environmental developments that have occurred over the last major glacial-interglacial cycle, while addressing how these changes have impacted sediment sourcing to the basin, with specific reference to aeolian (wind-blown) material. In Chapter 3, we address the paleomagnetic record from Burial Lake, which provides insights into the past directional orientations of the magnetic field, as well as past changes in geomagnetic intensity, both of which are preserved in a region with few existing data of comparable quality and temporal extent. We discuss the fidelity of the Burial Lake paleomagnetic record in terms of the lake's variable lithology, and comment on the spatial and temporal evolution of the field as it relates to deep Earth processes. In Chapter 4, we summarize our conclusions and provide a discussion of some of the ongoing and future work that will help to further constrain our observations at Burial Lake as well as provide a catalyst for future scientific research in the Arctic.

1.2 Background

1.2.1 The Earth's Magnetic Field

The Earth's magnetic field is generated by a self-sustaining dynamo effect caused by convective motions of the liquid iron-nickel alloy in the outer core, nearly 3,000 km below the Earth's crust (Merrill et al., 1998). It can be measured as a vector sum, described by directional components, Inclination (I) and Declination (D), as well as total field Intensity (F). The structure of the geomagnetic field is often described as a dipole centered on the Earth's axis of rotation (Merrill et al., 1998), much like a bar magnet in the center of the Earth. This geocentric axial dipole (GAD) approximation does appear to hold true if averaged over tens of thousands of years (Merrill et al., 1998; Tauxe et al.,

2010), and therefore is often used for reconstructing the motions of tectonic plates, which drift across the asthenosphere at speeds slow enough to average out short-term fluctuations in the magnetic field.

On shorter time scales however, the Earth's magnetic field exhibits a more complex morphology. Instrumental and historical observations show that the axis of the best-fitting dipole is offset from the axis of rotation, and the north magnetic pole is currently moving at a rate of ~50 km/year (Olsen and Mandea, 2007). Along with a growing area of reversed magnetic flux at the core-mantle boundary (CMB), below the South Atlantic, and the present dipole intensity decay rate of 5% per century, these observations have led some researchers to speculate that we are currently headed towards a polarity reversal or excursion (Hulot et al., 2002; Opdyke and Mejia, 2004). These sub-reversal scale changes, collectively termed paleomagnetic secular variation (PSV), occur on timescales ranging from seconds to millions of years, and have important implications for topics ranging from cosmogenic nuclide production (St-Onge et al., 2003; Snowball and Muscheler, 2007), to the convective behavior of the outer core (Bloxham and Gubbins, 1985), magnetostratigraphy (Lisé-Pronovost et al., 2009), and even to the navigation and lifecycles of living species (Lohmann et al., 2012).

1.2.2 Paleomagnetism

Instrumental and historical observations of PSV are limited to the past ~400 years (Chulliat et al., 2010; Jackson et al., 2000), and therefore, the only means of reconstructing earlier geomagnetic field variability is through studying the orientation of magnetic minerals preserved in geologic archives. The study of the ancient geomagnetic field preserved in geologic materials is known as Paleomagnetism. Lake and marine sediments are among the few such archives with the unique capability to provide continuous, high-resolution records of PSV that can be well dated, and with recent technological advances, such as the cryogenic superconducting u-channel rock magnetometer, we can accurately assess the paleomagnetic record preserved in even weakly magnetic sediments through rapid, inexpensive, and non-destructive means (Stoner and St-Onge, 2007).

The paleomagnetic signal in these environments is recorded as a depositional or post-depositional remanent magnetization (DRM or pDRM; Irving and Major, 1964). As magnetic grains fall through the water column and come to rest upon the sediment-water interface, they align with the ambient magnetic field. After a short time, they become "locked in" as they are buried below the surface mixed layer (SML) where they are no longer affected by bioturbation, and dewatering and compaction limit mechanical reorientation, thus preserving the directional components of the magnetic vector. Unlike geologic materials such as lavas and baked archeological artifacts, which are able to record absolute variations in Earth's geomagnetic field intensity through an empirically-derived thermo-remnant magnetization (TRM) acquisition process (Thellier and Thellier, 1959), unconsolidated sediments are only able to record relative changes in intensity down-core. This is because the magnetic acquisition process of sediments is both sensitive to changes in geomagnetic intensity, as well as lithologic variations associated with changes in the environment of deposition over time. Therefore, normalized remanence methods (Tauxe, 1993; Valet, 2003; Xuan and Channel, 2009) must be used to account for this lithologic variation and obtain a record of relative paleointensity (RPI).

Variable lithology can greatly influence a paleomagnetic record. Not all grains respond equally to an imposed magnetic field, and not all are capable of retaining a memory of the field at the time of deposition for extended periods of geologic time. The stability of a paleomagnetic recorder is a function of its mineralogy, concentration within the sediment, and domain state (typically referred to as magnetic grain size). As the study of paleomagnetism has developed, various criteria have been established for records thought to provide reliable directional and RPI results (King et al., 1983; Thompson, 1984; Opdyke and Channell, 1996; Tauxe, 1993; Stoner and St- Onge, 2007). Magnetite (an iron-oxide) in the pseudo single-domain (PSD) grain size range is typically viewed as the most reliable paleomagnetic recorder, and homogeneous sedimentary records containing high concentrations of magnetite typically produce the most dependable records of PSV (Stoner and St-Onge, 2007).

This lithologic information is commonly gained through the use of laboratory-applied magnetizations and rock magnetic measurements, the most common of which are anhysteretic remanent magnetization (ARM), and isothermal remanent magnetization

(IRM). Alone, or normalized by another magnetic parameter, the magnetic response to the induced magnetizations is again, a function of the concentration, mineralogy, and grain size, and can therefore be used to characterize the magnetic mineral assemblage serving as the paleomagnetic recorder, and the integrity of the paleomagnetic record over time (Stoner and St-Onge, 2007).

1.2.3 Environmental Magnetism

In any given depositional system (terrestrial or marine), the concentration, mineralogy, and grain size of magnetic materials are modulated by the environment of deposition over time, such that that many of these same measurements can provide a means of understanding environmental conditions that prevailed in the past (Evans and Heller, 2003). As all materials exhibit some form of magnetic behavior (even the air we breathe), and iron is one of the most abundant minerals in the Earth's crust (Evans and Heller, 2003), magnetic minerals, which are often present in minute proportions, can be readily detected, and act as passive environmental tracers, or proxy parameters, informing the geologic pathways of bulk sediments as they form *in situ*, or are transported across the Earth's surface and deposited in natural archives (Evans and Heller, 2003). The study of Environmental Magnetism therefore seeks to elucidate changes in lithology in terms of their climatic or environmental forcing mechanisms that cause changes in provenance, transport/depositional pathways, and/or physical/chemical alteration (Evans and Heller, 2003).

Often times, when the conditions are favorable, sediments can provide both a quality paleomagnetic record, as well as a stimulating record of environmental magnetic variability. It is in these special cases that these two seemingly unrelated branches of science become merged, and the theories and practices of each go hand in hand to recount a more complete story of Earth's dynamic past. The sedimentary record preserved in Burial Lake is one such example, and in the following chapters we hope to demonstrate the scientific gains that have resulted from this important research.

1.3 References

Bloxham, J., Gubbins, D., 1985. The secular variation of Earth's magnetic field. Nature 317, 777–781.

Bradley, R.S., 1999. Paleoclimatology: reconstructing climates of the Quaternary. Academic Press.

Chulliat, A., Thébault, E., Hulot, G., 2010. Core field acceleration pulse as a common cause of the 2003 and 2007 geomagnetic jerks. Geophys. Res. Lett. 37, L07301.

Cox, A., 1970. Latitude dependence of the angular dispersion of the geomagnetic field. Geophysical Journal of the Royal Astronomical Society 20, 253–269.

Evans, M.M.E., Heller, F.A., 2003. Environmental magnetism:, International geophysics series. Academic Press, Incorporated.

Hulot, G., Eymin, C., Langlais, B., Mandea, M., Olsen, N., 2002. Small-scale structure of the geodynamo inferred from Oersted and Magsat satellite data. Nature 416, 620–623.

Irving, E., Major, A., 1964. Post-Depositional Detrital Remanent Magnetization in a Synthetic Sediment. Sedimentology 3, 135–143.

Jackson, A., Jonkers, A.R.T., Walker, M.R., 2000. Four centuries of geomagnetic secular variation from historical records. Philosophical Transactions of the Royal Society of London. Series A: Mathematical, Physical and Engineering Sciences 358, 957–990.

King, J.W., Banerjee, S.K., Marvin, J., 1983. A new rock□magnetic approach to selecting sediments for geomagnetic paleointensity studies: Application to paleointensity for the last 4000 years. Journal of Geophysical Research: Solid Earth (1978–2012) 88, 5911–5921.

Lisé-Pronovost, A., St-Onge, G., Brachfeld, S., Barletta, F., Darby, D., 2009. Paleomagnetic constraints on the Holocene stratigraphy of the Arctic Alaskan margin. Global and Planetary Change 68, 85–99.

Lohmann, K.J., Putman, N.F., Lohmann, C.M., 2012. The magnetic map of hatchling loggerhead sea turtles. Current Opinion in Neurobiology 22, 336–342.

Merrill, R.T., McElhinny, M.W., McFadden, P.L., 1998. The magnetic field of the earth: paleomagnetism, the core, and the deep mantle. Academic Press.

Olsen, N., Mandea, M., 2007. Will the magnetic North Pole move to Siberia? Eos Trans. AGU 88, 293–293.

Opdyke, M.D., Channell, J.E., 1996. Magnetic stratigraphy. Academic Press.

Opdyke, N.D., Mejia, V., 2004. Earth's magnetic field. Geophysical Monograph Series 145, 315–320.

Snowball, I., Muscheler, R., 2007. Palaeomagnetic intensity data: an Achilles heel of solar activity reconstructions. The Holocene 17, 851–859.

St-Onge, G., Stoner, J.S., Hillaire-Marcel, C., 2003. Holocene paleomagnetic records from the St. Lawrence Estuary, eastern Canada: centennial- to millennial-scale geomagnetic modulation of cosmogenic isotopes. Earth and Planetary Science Letters 209, 113–130.

Stoner, J.S., St-Onge, G., 2007. Chapter Three Magnetic Stratigraphy in Paleoceanography: Reversals, Excursions, Paleointensity, and Secular Variation. Developments in Marine Geology 1, 99–138.

Tauxe, L., 1993. Sedimentary records of relative paleointensity of the geomagnetic field: theory and practice. Reviews of geophysics 31, 319–354.

Tauxe, L., Butler, R.F., Van der Voo, R., Banerjee, S.K., 2010. Essentials of paleomagnetism. University of California Press.

Thellier, E., Thellier, O., 1959. Sur l'intensité du champ magnétique terrestre dans le passé historique et géologique. [s.n.], Lille.

Thompson, R. 1984: A global review of paleomagnetic results from wet lake sediments. Pg. 145-164 in Haworth, E. Y. & Lund, J. W. G. (eds.): Lake Sediments and Environmental History. University of Minnesota Press, Minneapolis.

Valet, J., 2003. Time variations in geomagnetic intensity. Reviews of Geophysics 41.

Xuan, C., Channell, J.E.T., 2009. UPmag: MATLAB software for viewing and processing u channel or other pass-through paleomagnetic data. Geochem. Geophys. Geosyst. 10, Q10Y07.

Chapter 2

A 37,000-year Environmental Magnetic Record of Aeolian Dust Deposition from Burial Lake, Arctic Alaska

J.M. Dorfman[1]*, J.S. Stoner[1], M.S. Finkenbinder[2], M.B. Abbott[2], C. Xuan[1], G. St-Onge[3]

[1] Oregon State University, College of Earth, Ocean, and Atmospheric Sciences (CEOAS), Corvallis, Oregon, USA

[2] University of Pittsburgh, Department of Geology and Planetary Science, Pittsburgh, Pennsylvania, USA

[3] *Institut des Sciences de la Mer de Rimouski* (ISMER), Rimouski, Quebec, Canada

* Corresponding author e-mail: jdorfman@coas.oregonstate.edu

In preparation for submission to:

Quaternary Science Reviews

2.1 Abstract

Burial Lake sediments from the Noatak Basin in the northwest Brooks Range of Arctic Alaska (68.43°N, 159.17°W, 21.5 m water depth) provide an independently dated record, constraining regional environmental variability and insights into the region's climatic evolution over the last ~37,000 years. U-channel samples were studied through progressive alternating field (AF) demagnetization, with additional data provided by computed tomography (CT) derived density, hysteresis, isothermal remanent magnetization (IRM) acquisition, organic carbon content, biogenic silica, physical grain size on discrete samples, and point source magnetic susceptibility and X-ray fluorescence (XRF) on split cores faces. Environmental magnetic variability is complementary to, and enhances other datasets, allowing us to identify three distinct lithologic subunits associated with the last glacial period, the deglacial transition, and the Holocene. The radiocarbon-based chronology (11 accelerator mass spectroscopy; AMS ^{14}C dates, extending back ~37,000 Cal. yr. B.P) confirms that the timing of lithologic changes is consistent with global climate variations. Rock magnetic variability suggests changes in sediment provenance associated with the transition from glacial to interglacial conditions, interpreted to result from a variable flux of aeolian derived sediment. Aeolian material can be magnetically distinguished from locally derived, high-coercivity detrital sediments using diagnostic magnetic parameters. Using internal proxy data from Burial Lake in conjunction with regional paleoclimate data, published glacial chronologies for the Brooks Range, and a relative sea level reconstruction, we provide a discussion of possible local, widespread, and far-field sources of dust, and the time-dependency of potential forcing mechanisms governing its production, availability, transport, and deposition. Results indicate an overall reduction in dust input from the glacial period to the Holocene that is largely attributed to increases in terrestrial and aquatic productivity, warming, and moisture availability, which limited widespread landscape deflation and production of dust. In addition, subaerial continental shelves may have provided significant far-field sources of dust to interior Alaska during the glacial period, that were shut off by sea level inundation following the Last Glacial Maximum (LGM), further contributing to diminishing dust emissions. Lastly, while alpine glacial activity in the Brooks Range may provide local revenue of dust, activation of those deposits and timing of deposition

in Burial Lake often appears to be more directly linked with general aridity, lack of vegetative cover, and increased windiness, rather than glacial advances or retreats.

2.2 Introduction

Aeolian dust has long been used as a proxy indicator for past continental climates and atmospheric transport processes (Rea, 1994). Much focus has been given to late-Quaternary glacial-interglacial variations in "dustiness," with increased glacial dust flux attributed to colder temperatures, increased wind intensities, source aridity, limited vegetative cover, supply of glacier derived silt, and broad exposure of continental shelves from lowered sea level (Muhs et al., 2003a). Besides acting as a passive environmental tracer, aerosolic dust can also directly impact climate through radiative forcing (Tegen et al, 1996; Kohfeld and Harrison, 2001), or by fertilizing the world's oceans, thereby promoting phytoplankton blooms, which regulate atmospheric carbon dioxide (Hutchins and Brunland, 1998). At present however, both the sources of dust and the particular forcing mechanisms responsible for its production, availability, transport, and deposition are poorly understood, thus limiting our ability to accurately resolve records of dust flux in any particular region, or usefully incorporate that information in general circulation models (GCMs).

In Alaska, the majority of dust-related paleoclimate data are derived from thick terrestrial loess deposits that accumulate along major river valleys and blanket large areas of the landscape (Péwé, 1955). Determining the sources and depositional history of the Alaskan loess in relation to the timing of external environmental forcing mechanisms has been hindered by the often discontinuous and difficult to date nature of the deposits, as well as chemical diagenetic processes that can alter the physical and chemical properties of these sediments (e.g., Liu et al., 1999).

As an alternative, lakes provide a highly controlled, low energy depositional setting, capable of producing paleoclimate archives that are free from many of the physical and chemical processes that plague terrestrial loess deposits. While loess deposits are entirely composed of the material of interest, and therefore contain significant sedimentological noise, lake sediments contain merely an admixture of dust,

thus amplifying paleo-environmental signals against background sedimentation, and can be more easily dated to constrain the timing of specific events.

Here, we present a continuous ~37,000-year record of paleo-environmental change inferred from physical, geochemical, and environmental magnetic analyses of sediment cores from Burial Lake, Arctic Alaska, with a well-constrained radiocarbon chronology determined from accelerator mass spectrometry (AMS). Diagnostic magnetic parameters allow the magnetic distinction between locally weathered hematite-rich bedrock and the strongly ferrimagnetic (magnetite-rich) aeolian dust, as inferred from previous magnetic studies on Alaskan loess (Begét, 1990; 2001; Begét et al., 1990; Vlag et al., 1999; Liu et al., 1999; Lagroix and Banerjee, 2002; Muhs et al., 2003a; Muhs and Budhan, 2006; Evans et al., 2011). We perform this study within a simple depositional basin that appears sensitive to aeolian dust flux, while remaining isolated from local surficial processes, and relatively unscathed by glacial-interglacial processes, providing the oldest continuous lacustrine record from eastern Beringia.

2.3 Regional Setting

Burial Lake (68.43°N, 159.17°W) lies at 460 m above sea level in the Northwest Brooks Range, Alaska (Fig. 2.1). It is a small (~0.8 km^2) roughly circular lake, with a maximum depth of 21.5 m. Perched above the surrounding tundra on a slight topographic high, the catchment is limited in size, defined by steep-sided embankments (3-5 m high) that extend along most of the lake's perimeter. The lake has no direct inflow and contains a small outlet stream on the southwest shoreline. Burial Lake is oligotrophic and a hydrologically open system, and it is well mixed, with no evidence for thermal or chemical stratification (Abbott et al., 2010). Based on its isolated geographic setting and lack of fluvial input, we presume that sedimentation is influenced by aeolian deposition, with additional inputs derived from seasonal runoff and biogenic accrual.

Flanked by the DeLong Mountains to the north, and the Baird Mountains to the south, Burial Lake lies within the northwestern limit of the Noatak Basin, a broad lowland depression with a maximum width of 80 km. The Noatak River, which originates 110 km upstream on the granitic slopes of 2,523 m Mount Igikpak (the highest peak in Gates of the Arctic National Park & Preserve), cuts a central course through the

basin before eventually spilling into the Chukchi Sea at Kotzebue Sound. The Anisak and Aniuk Rivers descend southward from the DeLong Mountains, traversing the Basin along with the Cutler River system, which flows northward from the Baird Mountains (Hamilton, 2001).

The Noatak Basin has an arctic climate, with long cold winters and short cool summers. Mean July air temperature is ~11°C, and mean February temperature is estimated at -25°C (Elias et al., 1999). The basin floor is underlain by permafrost, which is generally continuous and extends beneath surrounding uplands (Ferrians, 1965). Vegetation is low-arctic tundra, dominated by sedges, *Salix*, shrub-*Betula*, and *Alnus*, with sparse stands of *Populus balsamifera* found in river valleys and along creek beds (Abbott et al., 2010). Tree-line for the nearest *Picea* (Spruce) forest lies ~100 km to the west, and also encroaches on the basin from the south (Abbott et al., 2010), but no evidence has been found thus far to suggest its presence within the basin during Holocene time (Hamilton, 2001).

During the mid and late Pleistocene, mountain glaciers repeatedly dammed the Noatak River forming a series of large proglacial lakes with surface areas as large as 4,400 km^2 (Hamilton, 2001) - collectively known as *Glacial Lake Noatak* (Hamilton and Van Etten, 1984). Glacial Lake Noatak appears not to have inundated Burial Lake since the Itkillik I (early Wisconsonian) glacial advance (Hamilton, 2010), and the lake remained ice-free during the Last Glacial Maximum (LGM: 26.5 – 19 ka; Clark et al., 2009), lying just beyond the reach of mountain glaciers and Northern Hemisphere ice-sheet extent (Hamilton, 2001).

2.4 Methods

2.4.1 Field Methods

During the summer of 2010, three sediment cores ranging from 4.15 - 6.51 m in length were collected; two from the deep central basin (A10 and C10: 21.5 m water depth) and one nearer to the margin (D10: 8.5 m water depth) using a 2" diameter square-rod Livingstone coring system designed to take 1 m successive drives. A larger, 2 5/8" polycarbonate barrel was used to capture the undisturbed sediment-water interface at each location. Overlapping sections assured complete recovery in the upper part of each

record, but in order to achieve deeper core penetration, holes were cased with PVC pipe, restricting the ability to overlap drives in the lower portions of the records.

2.4.2 Physical and Geochemical Analyses

Whole cores were split, described, and subsampled using ridged plastic u-channels (2x2 cm cross-sectional area) at the University of Pittsburgh. Organic content and wet/dry bulk density were computed from standard loss on ignition (LOI) analysis, weight percent biogenic silica (BSi) was determined, and X-ray fluorescence (XRF) measurements provided major and minor elemental abundances (the above data provided by Finkenbinder et al., *in prep*, with methods therein). At the *Institute des Sciences de la Mer de Rimouski* (ISMER), in Quebec, u-channels were photographed using a high-resolution digital camera mounted on a GEOTEK™ Multi Sensor Core Logger (MSCL). Scanning electron microscope (SEM) images were acquired in discrete intervals to visualize grain-specific traits and characterize the relative abundance of diatoms. Bulk physical grain size (including both lithogenic and biogenic fractions) was measured at 10 cm increments using a Beckman-Coulter™ LS 13320 laser diffraction analyzer. Grain size distribution and statistical parameters were calculated using the Gradistat software (Blott and Pye, 2001). Computed Tomography (CT) scans on the u-channels were obtained at the *Institute national de la recherché scientifique, Centre Eau Terre Environement* (INRS-ETE) in Quebec City, in order to visualize sedimentary structures, assess possible core deformation, and aid stratigraphic matching efforts. The CT numbers were extracted using a MATLAB™ code developed by Jaques Labrie, at ISMER, primarily reflecting changes in bulk density (St-Onge et al., 2007).

2.4.3 Rock Magnetic Measurements

Point source low-field magnetic susceptibility (k_{LF}) was measured on split cores at the University of Pittsburgh, at a 2 mm resolution using a Bartington™ MS2 meter and MS2E1 sensor, mounted to a TAMISCAN-TS1 automatic stage conveyor. Rock magnetic properties were studied through progressive Alternating Field (AF) demagnetization of u-channel samples measured at 1 cm intervals using a 2G Enterprises™ model 755-1.65UC cryogenic superconducting u-channel rock

magnetometer and pulse magnetizer module (for Isothermal Remanent Magnetization; IRM), at the Oregon State University *Paleo- and Environmental Magnetism Laboratory*. U-channel results were assessed using UPmag software (Xuan and Channell, 2009).

After natural remanent magnetization (NRM) measurements (the paleomagnetic results of this study will be presented elsewhere), anhysteretic remanent magnetization (ARM) was induced at a peak AF of 100 mT with a 0.05 mT direct current (DC) biasing field and measured before and after AF demagnetization up to a peak AF of 100 mT at 5 or 10 mT spacing. An initial IRM was imparted with a DC field of 0.3 T and measured after demagnetization at the same steps as the ARM. A second IRM imparted with a DC field of 1.0 T and considered to represent a saturation isothermal remanent magnetization (SIRM) was also measured after demagnetization at the same steps as the ARM. The response to these laboratory-applied magnetizations is not only a function of the concentration of ferrimagnetic material within the sample, but also of the sample's mineralogy and domain state (typically referred to as *magnetic grain size*) – all properties that are modulated by the environment of deposition. Akin to trace element analysis, environmental magnetism is the analytical determination of a minute population of minerals contained within the bulk sample, that inform the geologic pathways of the bulk sediments through time. Alone, or normalized by another magnetic parameter, the different magnetizations are used to assess lithologic variations down-core as they relate to changing environmental conditions and sediment input to the basin over time (Dekkers, 1996).

Demagnetization ratios (e.g., $ARM_{30\ mT}/ARM_{0\ mT}$, or $SIRM_{30\ mT}/SIRM_{0\ mT}$) provide information on the coercivity of the sample and are analogous to the medium destructive field (MDF) commonly used to characterize NRM (Stoner and St-Onge, 2007), which is a reflection of magnetic grain size and/or mineralogy. Higher values indicate higher coercivity, or finer grainsize if the sample is of uniform ferrimagnetic mineralogy (Stoner and St-Onge, 2007). $ARM_{0\ mT}/SIRM_{0\ mT}$ is widely employed as a magnetic grain size indicator for magnetite, with finer grain sizes yielding larger values (Evans and Heller, 2003). The parameter derived by normalizing the IRM at 0.3 T by the SIRM at 1.0 T, sometimes referred to as a pseudo S-Ratio (St-Onge et al., 2003) is analogous to the S-ratio of Stober and Thompson (1979), and can be used to estimate the proportion of high

vs. low-coercivity magnetic mineralogies (e.g., the proportion of magnetite to hematite). Values closer to 1 denote an exclusively low-coercivity ferrimagnetic mineral assemblage, such as magnetite, while lower values signify the presence of higher-coercivity components, such as hematite (Thompson and Oldfield, 1986; King and Channel, 1991; Stoner and St-Onge, 2007). The "hard" IRM (HIRM) is a measure of the concentration of high-coercivity material (e.g., hematite), and are here defined as a version optimized for u-channel measurements (Stoner and St-Onge, 2007); HIRM = 0.5*(SIRM-IRM).

Hysteresis experiments on subsampled bulk material were carried out at ISMER on a Princeton Measurements Corporation™ MicroMag model 2900 alternating gradient force magnetometer (AGM), to assess both mineralogy and magnetic grain size. Hysteresis loops were corrected for paramagnetic/diamagnetic contributions, and the following values were derived: the coercivity of magnetic minerals (Hc), the coercivity of remnance (Hcr), the saturation magnetization (Ms), and the saturation remnance (Mrs).

IRM acquisition experiments were performed on select bulk samples using a Princeton Measurements Corporation™ MicroMag model 3900 vibrating sample magnetometer (VSM) at Western Washington University. Data were smoothed using a MATLAB™ loess filter, and IRM decomposition was performed using IRMUNMIX V2.2 (Heslop et al., 2002). This software package automates the fitting of IRM acquisition curves through the use of an expectation-maximization algorithm to decompose curves into their individual component contributions, thereby facilitating the distinction of magnetic mineral assemblages within the bulk sample.

Thermomagnetic analyses were attempted on four bulk samples to study the temperature dependence of k_{LF}, using an MS2WF Bartington™ instrument. Measurements were heated at 2°C steps from room temperature (24°C) up to 700°C, and subsequently cooled to room temperature. Unfortunately, given the weak k_{LF} of Burial Lake sediments and the sample size limitations of the instrument, results proved unreliable, and data are not presented.

2.4.4 A10/C10 Composite Depth Scale

Down-core measurements and detailed core descriptions were used to characterize lithologic subunits and transitions, and stratigraphically correlate deep basin cores, A10 and C10, placing them on a common depth scale. Correlation between deep basin cores and the margin core (D10), however, proved more difficult due to an absence of material in D10 suitable for radiocarbon dating, and a likely depositional hiatus, observed in D10, and previously observed at a similar shallow margin location in the lake (Abbott et al., 2010).

To construct the A10/C10 composite depth scale, A10 was initially selected as a baseline, based on its slightly longer length, abundant radiocarbon dates, minor core deformation, and more extensive proxy datasets. Minor internal adjustments were first made to field measurements of A10 drive-depth to align features between overlapping drives. C10 drives were then individually "hung" on the revised A10 depth scale to stratigraphically align comparable features between cores. Considering the close proximity of coring sites, no stretching or squeezing of C10 drives was required to achieve a satisfactory match (see Appendix A).

Based on this correlation, it is possible to splice together portions of each core to construct a composite record. However, given the quality, continuity, and extent of the A10 dataset, (and in many intervals, lack of comparable C10 data) we currently find this method impractical. From here forward, we focus on results from the 6.51 m A10 core. The A10/C10 composite depth scale (referred to throughout as "depth") is utilized solely for the production of the age-depth model, in which radiocarbon-dated samples were derived from both A10 and C10 cores (see the following).

2.5 Age-Model

AMS radiocarbon measurements were performed on 13 terrestrial macrofossil samples from cores A10 and C10 at the *Keck-Carbon Cycle AMS Facility* at the University of California, Irvine. Results are shown in Table 2.1 and Figure 2.2. Size-dependent sample preparation backgrounds were subtracted based on measurements of ^{14}C-free wood. All results have been corrected for isotopic fractionation according to the conventions of Stuiver and Polach (1977), with $\delta^{13}C$ values measured on prepared

graphite. Radiocarbon ages were calibrated using Calb 6.0 (Stuiver et al., 2005), and the IntCal09 calibration curve (Reimer et al. 2009), assuming a ΔR of 0. Calibrated ages are reported at their 2σ confidence level.

Two out of the original 13 dates (UCIAMS #109363 and #89123; Table 2.1) were excluded prior to generating the age-depth model (Fig. 2.2). The first date at 359.5 cm appears anomalously young – possibly contaminated by modern carbon during the combustion and graphitization of this small (0.017 mgC) sample (Oswald et al. 2005), which approaches the threshold limit for AMS radiocarbon analysis. Inclusion of this date would also invoke a sudden and drastic increase in sedimentation rate (reaching 1.51 m/ka), which is unsupported by additional radiocarbon constraints or lithologic evidence, and is hard to imagine given the local geography. The second date at 598 cm displays a slight age-reversal with an adjacent date (#89124; Table 2.1), though overlapping error bars suggest both are statistically sound age-control points. We exclude date #89123 based on its slightly broader uncertainty and lower carbon yield.

CLAM software for "classical," non-Bayesian age-depth modeling (Blaauw, 2010) was used to produce the "best fit" linearly interpolated age used throughout this report (Fig. 2.2). To account for chronologic uncertainty, we apply a Monte Carlo-based approach that perturbs the interpolated age-depth model 10,000 times following a random draw from a normal distribution between the 2σ calibrated ^{14}C ages (Marcott et al., 2013). The uncertainty between the age control points (Fig. 2.2) is modeled as a random walk, after Huybers and Wunch (2004), with chronologic uncertainty assumed to be auto-correlated through time and modeled as a first order autoregressive (AR1) process.

2.6 Results

2.6.1 Sedimentology and Lithostratigraphy

The sediment record from Burial lake appears continuous over the last ~37,000 years, with sedimentation rates (Fig. 2.2) ranging between 8.8 and 29.4 cm/ka, averaging 20.3 cm/ka for the whole record. In its entirety, the record shows distinct lithologic changes down-core from a primarily biogenic, high organic carbon, low magnetic concentration and high magnetic coercivity at the top of the core, to a more lithogenic, lower organic, higher magnetic concentration and low-coercivity below. These changes

can be divided into three distinct lithologic subunits defined using down-core physical, geochemical, and magnetic properties (Fig. 2.3) that aid the paleo-environmental interpretation of the Burial Lake record.

Lithologic Subunit 1 (651 – 285 cm)

Subunit 1 corresponds to the glacial period (37.2 – 19.4 ka), and extends from the base of the core (651 cm) to 285 cm (Fig. 2.3). Sediments consist mainly of pale yellowish-brown (Munsell color: 10YR 6/2) to dark yellowish-brown (10YR 4/2) very fine to very coarse-grained silts, with a moderate percentage of clay (~10-26%; Fig. 2.3) and a small, but unknown fraction of granules that exceeded the 2 mm measurement limit of the laser diffraction analyzer, and was sieved and removed prior to textural analysis. Mean physical grain size (Fig. 2.3) for Subunit 1 ranges between 4 and 10 μm. Faint banding is observed in CT images from this interval, and throughout the Burial Lake record (Fig. 2.3). CT density (324.4 ± 62.9 HU) and k_{LF} (1.3 x 10^{-5} ± 0.3 x 10^{-5}) are relatively high and variable, while organic matter (8.1% ± 0.9%) and BSi (1.4% ± 0.4%) contents are relatively low (Fig. 2.3). These data are consistent with SEM images, which reveal sediment composed mainly of lithogenic detritus, and containing a near absence of diatoms. Though BSi in Subunit 2 (Fig. 2.3) shows no significant long-term trend, organic matter (Fig. 2.3) generally decreases towards the bottom of Subunit 2, while k_{LF} gradually increases. Other concentration-dependent magnetic parameters, ARM, IRM, and SIRM (Fig. 2.3) mimic k_{LF}, with relatively high and variable intensities, consistent with higher concentrations of ferrimagnetic material in this subunit. Ratios of $ARM_{30\ mT}/ARM_{0\ mT}$ and $SIRM_{30\ mT}/SIRM_{0\ mT}$ (Fig. 2.3; 0.49 ± 0.03, and 0.38 ± 0.04, respectively) suggest sediments in Subunit 1 are dominated by a low-coercivity mineral assemblage, with values typical of magnetite. S-Ratios (Fig. 2.3) are high (0.93 ± 0.02), increasing up core, to a maximum of ~0.96 near the top of Subunit 1. This is consistent with a high proportion of magnetite, with decreasing S-Ratios with depth (reaching ~0.86 at the base of the core) suggest an increasing proportion of high-coercivity minerals (hematite) in the bottom of record.

While uncorrected hysteresis loops (dashed lines, Fig. 2.4) show substantial high-field slopes diagnostic of significant paramagnetic contributions, slope-corrected loops

(solid lines, Fig. 2.4) are consistent with low-coercivity ferrimagnetic minerals, with Mrs/Ms values mostly ranging between 0.1 and 0.3, and saturation fields mostly below 0.2 T (Day et al., 1977; Tauxe, 1993). Ratios of Mrs/Ms and Hcr/Hc are plotted in Figure 2.4 according to Day et al., (1977). Samples from Subunit 1 fall within the pseudo single-domain (PSD) to multi-domain (MD) theoretical grain size boundaries for magnetite.

Discrete peaks in magnetic parameters punctuate the record at 582, 294, and 210 cm (33.1, 19.8, and 15.8 ka, respectively) (Fig. 2.3). These are perhaps related to cryptotephra deposits, though despite concerted effort, none of this highly magnetic material could be isolated and identified as such, and their source remains unknown.

Sedimentation rates (Fig. 2.2) in Burial Lake are elevated (25.0 – 29.4 cm/ka) throughout most of the glacial period, with the exception of the interval between 30.2 and 35.6 ka, where they appear to drop to 9.6 cm/ka. Timing of sedimentation rate changes and the magnitude of uncertainty are at least partially a function of the radiocarbon date locations, and without a better-constrained chronology through the glacial interval, it is difficult to address sedimentation rate in context with environmental change.

Lithologic Subunit 2 (285 – 140 cm)

Subunit 2, corresponding to the deglacial transition (19.4 – 9.8 ka), is characterized by a transitional lithology extending from 285 and 140 cm (Fig. 2.3). Lower sediments are dark yellowish-brown (10YR 4/2) in color, changing to a dusky-brown (5YR 2/2) at ~225 cm, and eventually grading to greyish-brown (5YR 3/2) in the upper part of the transition. Marked declines in CT density, k_{LF}, ARM, IRM, and SIRM (Fig. 2.3) are accompanied by significant increases in organic content and BSi (Fig. 2.3). Sediments are still dominated by fine to very coarse-grained silts, but mean physical grain size increases substantially (peaking at 26 μm) with the appearance of a moderate amount (8-19%) of fine to very fine sand introduced around 130 cm (Fig. 2.3). Clay content remains below 13% (Fig. 2.3). As physical grain size samples were not pre-treated to remove biogenic components, the increase in grain size during this time interval may be partially attributed to the increased abundance of diatoms, which are often larger than lithic grains. Ratios of $ARM_{30\ mT}/ARM_{0\ mT}$ and $SIRM_{30\ mT}/SIRM_{0\ mT}$ (Fig.

2.3) increase through the transition, and since coercivity variations within these parameters are mainly limited to what can be achieved by AF demagnetization at low fields, the increase in coercivity is consistent with a fining of magnetic grain size, rather than a change in mineralogy. This is supported by increasing values of $ARM_{0\ mT}/SIRM_{0\ mT}$ (Fig. 2.3), as ARM is sensitive to fine-grained magnetite (Evans and Heller, 2003), but is contrary to mean physical grain size (Fig. 2.3) and unsupported by hysteresis results (Fig. 2.4), which show no significant difference in magnetic grainsize. However, the influence of magnetic mineralogical changes on these ratios must also be considered, as well as the biogenic contributions to bulk physical grain size measurements.

A distinct change in S-Ratios is observed to occur around 212 cm, (16 ka; Fig. 2.3). This is interpreted to result from a change in magnetic mineralogy (Thompson and Oldfield, 1986; King and Channel, 1991; Stoner and St. Onge, 2007). HIRMs (Fig. 2.3) decrease through this interval in accordance with k_{LF}, ARM, IRM, and SIRM, demonstrating the overall decrease in concentration of both the high and low coercivity magnetic components. Because the decrease in concentration of both low and high coercivity minerals is associated with increases in productivity indicators (Fig. 2.3) it results at least partially from organic/biogenic dilution of the detrital components. S-Ratios, on the other hand, are insensitive to organic/biogenic dilution, and sharply decline to ~0.83 (Fig. 2.3), reflecting an increase in the proportion of high coercivity minerals (hematite) relative to low coercivity minerals (magnetite) through this transitional sub-unit. S-Ratios slightly increase for the remainder of Subunit 2, but remain below 0.86. Sedimentation rates (Fig. 2.2) appear to decrease through the deglacial transition, averaging 18.3 cm/ka, and reaching their lowest overall values between 16.8 and 11.7 ka.

Lithologic Subunit 3 (140 – 0 cm)

Subunit 3, dating to the Holocene (9.8 ka - present), extends from 140 cm to the top of the core (0 cm; Fig. 2.3). Sediments consist mainly of fine to very coarse silt with small amounts (<7%) of very fine sand and clay (Fig. 2.3) - dusky-brown (5YR 2/2) at the base and grading to greyish-brown (5YR 3/2). Uppermost sediments are dark-yellowish brown (10YR 4/2). Mean physical grain size (Fig. 2.3) ranges between 13 and 18 μm. A finer grained ferrimagnetic assemblage is suggested by higher values of ARM_0

$_{mT}$/SIRM$_{0\ mT}$, as well as ARM$_{30\ mT}$/ARM$_{0\ mT}$ and SIRM$_{30\ mT}$/SIRM$_{0\ mT}$ ratios, 0.55 ± 0.02 and 0.62 ± 0.03, respectively (Fig. 2.3). CT density is low and less variable (-47.1 ± 62.8 HU), along with k_{LF} (0.26 x 10^{-5} ± 0.07 x 10^{-5}) and other concentration dependent magnetic parameters (Fig. 2.3). Organic content peaks near the boundary of Subunits 2 and 3 at 19.3% (Fig. 2.3), then slightly decreases until ~129 cm, but remains elevated (13.2% ± 1.1%) comparative to previous subunits. BSi is also elevated (11.4% ± 2.4%), increasing steadily from the base of Subunit 3 before leveling off in the upper ~100 cm (Fig. 2.3). These data are consistent with SEM images, which reveal an increased abundance of diatoms and organic detritus, relative to clastic mineral matter. Noisy hysteresis loops (Fig. 2.4) reflect the low ferrimagnetic concentrations in Subunit 3, which approach instrumentation limitations and result in somewhat scattered hysteresis results with respect to domain-state boundaries (Fig. 2.4).

S-Ratios (0.81 ± 0.02) decline rapidly again between 140 and 103 cm, reaching values as low as ~0.78 (Fig. 2.3). Values increase again in the upper ~35 cm, but do not exceed 0.85. Smaller values of XRF Fe/k_{LF} in Subunit 1 (Fig. 2.3) suggest the iron content of these sediments is more or less fully accounted for by k_{LF}. Conversely, the higher ratios observed during Subunits 2 and 3 reflect sediments that are high in iron, yet display weak values of k_{LF}. This "unaccounted" for iron must therefore be tied up in minerals like hematite, an iron oxide that is elevated in iron, but possesses a weaker k_{LF} (Dunlop and Özdemir, 2001), consistent with the increased proportion of high-coercivity minerals. Sedimentation rates are also comparatively low (11.6 – 16.7 cm/ka) during the Holocene (Fig. 2.2), displaying a slight increasing trend from the early Holocene to present.

2.6.2 IRM Acquisition/Decomposition Results

To further quantify the magnetic mineralogical changes, IRM acquisition curves were generated from subsampled material at nine down-core locations (Fig. 2.3). Representative normalized curves from each lithologic subunit are shown in Figure 2.5. Results indicate similar coercivity distinctions as observed in the S-Ratios (Fig. 2.3), with samples from Subunit 1 acquiring magnetization more quickly than samples from Subunits 2 and 3, and displaying low-coercivity behavior characteristic of magnetite. All

samples reach magnetic saturation within a narrow range of field intensities (1200-1400 mT), with samples from Subunits 2 and 3 saturating towards the high end of this range. While hematite usually continues to acquire magnetization beyond 1400 mT (Lowery, 1990), the high-coercivity minerals present in Subunits 2 and 3 may be hematite of a complex or impure variety. Regardless of the exact mineralogy, S-Ratios and IRM acquisition results show it to be fundamentally distinct from the magnetite-rich sediments in Subunit 1.

IRM decomposition enables the separation of remanence-bearing sediments into their individual component contributions, allowing us to estimate the number of endmembers needed to explain the bulk magnetic properties of the sediments, and track relative changes in endmember contribution over time (depth). IRM decomposition results are based on smoothed input curves as shown in Figure 2.6, with results for all samples provided in Table 2.2. Smoothing was required because of the extremely weak magnetization of these samples resulted in measurement noise. Regardless, the consistency of results supports the interpretations. Burial Lake sediments are best described by a two-component model, with both low-coercivity (component 1) and high-coercivity (component 2) sources present throughout the record. The R^2 correlation of smoothed input data to the sum of one, two, three, and four components, are provided in Figure 2.7, supporting our use of a two-component model. Following on the principle of parsimony (Imbrie, 1963), which was specifically envisioned for the case of un-mixing models, this provides the best-fitting, simplest, and most geologically meaningful solution.

Excluding two samples, which contained either excessive measurement noise (sample B), or a third low-coercivity component (sample G), mean coercivities for component 1 (Table 2.2) are extremely consistent (44.0 ± 2.7 mT), suggestive of a common low-coercivity mineralogy, and consistent with a fine-grained magnetite source. Mean coercivities for component 2 (Table 2.2; 270.2 ± 56.8 mT) are much higher, with increased variability perhaps indicating variable high-coercivity sources, or an artifact induced by smoothing in the much noisier high-coercivity range (Fig. 2.6).

Relative percent contributions depicted in Figure 2.6 and Table 2.2 illuminate coercivity trends observed in S-Ratios (Fig. 2.3). Though high-coercivity minerals are

present throughout the record, their influence on S-Ratios is at times overshadowed by increased abundance of the low-coercivity mineralogy (e.g., magnetite), an observation consistent with previous studies on S-Ratio sensitivity (e.g., Frank and Nowaczyk, 2008) that conclude an overwhelming percentage of hematite is needed to cause any major decrease in S-Ratios. Sample H (474 cm) from Subunit 1 provides an instructive example, containing an overwhelming 93.0% component 1 (compared with 7.0% component 2), corresponding to a high S-Ratio of 0.94. Only when component 1 contributions are reduced throughout Subunits 2 (e.g., sample E, 190 cm: 87.8%) and 3 (e.g., sample A, 40 cm: 68.2%), can component 2 drive S-Ratios towards lower values (0.85 and 0.78, respectively). The overall ~25% reduction in component 1 that occurs between samples H at 474 cm and sample A at 40 cm is consistent with general decline in S-Ratios that occurs throughout Subunits 2 and 3. A 12.4% increase in component 1 is also observed to occur between sample I (574 cm) and sample H (474 cm), in keeping with increasing S-Ratios from the base of the core. Though components 1 and 2 refer specifically to IRM acquisition/decomposition results from a few discrete measurements, they are representative of the low and high-coercivity mineralogies present in variable proportion throughout the Burial Lake record, identified through the number of different rock-magnetic observations pertaining to coercivity/mineralogy that are measured more continuously throughout each subunit (Fig. 2.3).

2.7 Discussion

2.7.1 Lithologic Interpretation

Down-core physical, geochemical, and magnetic parameters are shown versus age in Figure 2.8, allowing us to place our paleo-environmental results in the context of time. The pattern of variability observed in the Burial Lake record, with low ferrimagnetic concentration and an increased proportion of high-coercivity components at the top of the record, transitioning to higher magnetic concentrations with a low-coercivity component mineralogy in the lower part of the record, could be explained either in terms of diagenetic alteration (e.g., post-depositional magnetite dissolution), or through a change in sediment source brought to the basin. We find that a diagenetic model to explain the rock magnetic variability is unlikely, as; **1)** There is no physical evidence for significant

diagenesis at any point in the record (e.g., laminations, gas production, elemental deposits) and the lake appears well oxygenated with no stratification. **2)** There is no evidence for a core-top diagenetic transition, commonly observed and associated with reducing environments where magnetic dissolution occurs (Karlin and Levi, 1983; Anderson and Rippey, 1988). **3)** The magnetic properties of Subunit 1 are consistent with a fine-grained ferrimagnetic component, whereas magnetic dissolution commonly results in coarse grain ferrimagnetic residual (Karlin and Levi, 1983, Anderson and Rippey, 1988), which is not what we observe. Therefore, the rock magnetic variability observed is more likely derived from variations in sediment sources, which we suspect reflect local versus far-field (aeolian) sources.

We interpret the low-coercivity ferrimagnetic (e.g., magnetite) component to reflect the input of aeolian dust based on the following cumulative reasoning:

1. A low-coercivity magnetic mineralogy dominates glacial period sedimentation in Burial Lake, (i.e., Subunit 1; Fig. 2.8), and enhanced glacial-age loess production is well supported, with ubiquitous deposits found throughout Alaska (Péwé, 1955; Muhs et al., 2003a; 2003b).
2. Glacial-age sediments from Burial Lake have comparable magnetic characteristics to Alaskan loess (Fig. 2.4-2.6, 2.8; Table 2.2), which contains significant quantities of magnetite, contributing to high values of k_{LF}, and coercivity similar to that of component 1 (Begét, 1990; 2001; Begét et al., 1990; Vlag et al., 1999; Liu et al., 1999; Lagroix and Banerjee, 2002; Muhs et al., 2003a; Muhs and Budhan, 2006; Evans et al., 2011).
3. Sedimentation in Burial Lake during the glacial period is characterized by extensive fine-grained deposition of silts and clays with a mean physical grain size of 4 – 10 μm (Fig. 8). This is within the lower grain size range of the Alaskan loess (Muhs and Buhdan, 2006), and consistent with aeolian deposition.
4. Detrital flux ($F_{detrial}$ = SR*[BD*(100% - %OM - %BSi)]), calculated by removing weight percent organic matter (OM) and biogenic silica (BSi) contributions from total dry bulk density (BD), and factoring in sedimentation rate (SR), shows that mineralogenic input was approximately four and half times greater during the glacial

period than in the Holocene, consistent with the gradual diminished relative contribution of low-coercivity ferrimagnetic components and the decrease in S-Ratios through the deglacial transition (Fig. 2.6, 2.8).

5. Based on its regional geographic setting, Burial Lake appears sensitive to aeolian deposition. Due to the lack of other inputs, the only means to achieve increased detrital flux during the glacial period (other than increasing dust flux) would be to increase precipitation and spring runoff. This conflicts with widespread evidence for prevailing xeric conditions over the glacial-age landscape of interior Alaska (Hopkins, 1982).
6. Sedimentation rates are comparatively low during the Holocene (Fig. 2.2), and the concentration of the low-coercivity magnetic component is significantly diminished (Fig. 2.8). Yet, it still accounts for the bulk of Holocene sedimentation. Again, based on regional geography, Burial Lake likely still remains sensitive to aeolian deposition. While less extensive and episodic in nature, Alaskan loess deposition continued even after the LGM, with deposits as recent as ~3 ^{14}C ka found at Delta Junction, south of Fairbanks (Muhs et al., 2003a). Modern dust storms are common in Alaska during the snow-free months of spring, summer, and early fall (Begét, 2001). In some areas, river bars exposed to wind in winter can cause dust to accumulate in winter snowpack before melting out in the spring (Péwé, 1955).

For the following cumulative reasoning, high-coercivity material is interpreted as a locally-derived source, weathered from surrounding uplands and transported to Burial Lake during seasonal runoff events:

1. Though variable, high-coercivity material is present throughout all parts of the Burial Lake record (Fig. 2.6, Table 2.2), and remains an active sediment source irrespective of the drastic environmental changes associated with the glacial-interglacial transition, and therefore, must be immediately available from the local catchment.
2. The Brooks Range, while geologically diverse, has been shown to contain significant high-coercivity mineral concentrations within the Paleozoic and Mesozoic sedimentary and metasedimentary strata that comprise regional bedrock topography

(Slack et al., 2004; Mayfield et al., 1984; Ellersieck et al., 1984). Among such deposits, are large outcroppings of the Kayak shale (early Mississippian), the same friable and highly oxidized (i.e., hematite bearing) material responsible for the reddish hue in sediments from Blue Lake (Bird et al., 2009) in the central Brooks Range near Atigun Pass.

Given these deductions, we suggest that S-Ratios, though only a measure of relative proportion, are a sensitive indicator for dust input to Burial Lake, with higher values indicating periods of increased accumulation, and lower values indicating periods of diminished flux, while IRM acquisition/decomposition allows for background levels of high-coercivity material to be discerned through out the record.

2.7.2 Local and Far-field Sources of Dust, Timing of Deposition, and Potential Forcing Mechanisms

Generally speaking, there are three conceivable ways in which aeolian dust could be made available for transport to Burial Lake: **1)** Sea level lowering could expose large portions of the continental shelves, providing a potential far-field source of dust to Burial Lake; **2)** Expansion of alpine glaciers in the Brooks Range could also generate potential local revenue of dust (though it would need to be weathered from localized low-coercivity bedrock to fit our description of component 1); and **3**) A dry and windy environment with little vegetative cover could expose the landscape to deflation, generating a widespread source of dust without the need to invoke sea level *or* glacial activity. In the remainder of this report, we provide a paleo-environmental interpretation of the Burial Lake record, devoting particular attention to the timing and extent of dust deposition as depicted from the S-Ratio proxy. We compare these changes to other internal proxy data from Burial Lake, and place them in context with regional paleoclimate data, the glacial chronology of the Brooks Range, and relative sea level (Fig. 2.9). In doing so, we are able to at times distinguish the mechanism(s) responsible for increased or decreased dust input to Burial Lake, and therefore identify or exclude potential source(s).

The Last Glacial Period (Subunit 1) 37.2 – 19.4 ka

S-Ratios are highest and magnetic concentrations are greatest during the last glacial period (Fig. 2.8), and reflect a general increasing trend in dust accumulation from moderate levels in the earliest portion of the record during Marine Isotope Stage 3 (MIS-3; i.e., prior to ~30 ka), reaching a maximum at the height of the global LGM (19 – 20 ka). Fine-grained sediments with high CT density and increasing values of k_{LF} (Fig. 2.8) are consistent with increasing accumulation of aeolian dust. Low organic matter (Fig. 2.8) and the general absence of terrestrial macrofossils for AMS radiocarbon analysis between ~30 and ~17 ka (Fig. 2.2), suggest the surrounding landscape was largely devoid of substantial vegetation, indicating a windswept tundra environment that was colder and drier than present. Low BSi (Fig. 2.8) suggests diminished lake productivity due to cold conditions with a short, ice-free summer season, along with potentially turbid and/or nutrient depleted waters. Abbott et al. (2010) determined that the depositional hiatus in the shallower portions of Burial Lake occurred between 34.8 and 23.2 ka, corresponding to a significant drop in lake level from decreased moisture availability.

Proxy data from Burial Lake are consistent with evidence elsewhere in the region depicting extremely cold, arid, and windy conditions leading up to the LGM (Hopkins, 1982), highlighting the potential for significant landscape deflation and production of dust. The ubiquity of loess deposits placed stratigraphically above palaeosols dating from ~45 to ~33 ka at Halfway House, Gold Hills, Birch Hills, and Chena Hot Springs Road, near Fairbanks (Muhs et al., 2003a) provides evidence of xeric and windy conditions. Furthermore, Birch Lake (Abbott et al., 2000), in the Tanana valley, southeast of Fairbanks, was dry prior to 15 ka (Fig. 2.9), along with many other small lakes in the unglaciated interior of Alaska (e.g., Ager, 1982; Bigelow, 1997; 2001; Carlson and Finney, 2004; Wooler et al., 2012), demonstrating a substantial moisture deficit during the glacial period. Though loess production and windiness appear to increase, Muhs et al., (2003a) note surprisingly little accumulation of loess during the LGM, which they attribute to sparse vegetation and limited ground surface roughness. Though these attributes may inhibit terrestrial loess accretion, they would not necessarily prohibit deposition in lakes. Burial Lake S-Ratios may therefore offer a more accurate

portrayal of dust production during the LGM, further demonstrating the advantages lacustrine records hold over traditional terrestrial loess deposits.

Fossil chironomid-inferred temperatures from Burial Lake and Zagoskin Lake (western Alaska; Kurek et al., 2009) are consistent with a pollen-based study for eastern Beringia (Viau et al., 2008), reflecting summer temperatures during the last glacial period that were 3.5 – 4°C colder than present, allowing for the expansion of alpine glaciers in the Brooks Range, despite the considerably arid conditions. Non-finite radiocarbon ages on glacial deposits in the central Brooks Range indicate that Itkillik I (early Wisconsonian) glaciation occurred largely before 53 ^{14}C ka (Hamilton, 1994). In the Noatak Basin, Itkillik I advances are younger than the Old Crow tephra (140 ka) and older than 36 – 34 ka. (Hamilton, 2001). Bracketing radiocarbon ages of 30 and 13 ka in the central (Hamilton, 1982) and western (Hamilton 2001) Brooks Range, constrain the timing of the subsequent Itkillik II (late Wisconsonian) glaciation, which reached its maximum extent between 27 and 25 ka (Fig. 2.9; Briner and Kaufman, 2008). Though extensive in the eastern and central parts of the Brooks Range, growth of alpine glaciers (and the potential for dust generation) became progressively more restricted towards the west, primarily due to the lower-lying topography of mountain valleys (Hamilton and Labay, 2011). Therefore, some mountain valleys in the western Brooks Range did not support glaciers of Itkillik II age (Hamilton and Labay, 2011). This, combined with the fact that S-Ratios do not diminish in response to waning Brooks Range glaciers from their maximum Itkillik II extents (they in fact continue to increase; Fig. 2.9), suggests that local glaciers likely did not contribute substantially to the supply of dust deposited in Burial Lake during the glacial period, or at least cannot be held accountable for the increasing trend in in S-Ratios leading up to the LGM (Fig. 2.9).

Increased exposure of Beringian continental shelves from rapidly declining sea level may help to explain the increase in dust input over the glacial period, particularly considering that newly exposed coastline would likely have lacked substantial vegetative cover and been subjected to the same arid and windy conditions that persisted in the continental interior. A marine source has been inferred for glacial-age loess found in coastal locations along the Seward Peninsula, in USGS marine cores from Norton Sound, and in Zagoskin Lake on St. Michael's Island (Muhs et al., 2003b). While these sites are

limited to the western coast of Alaska, it is not unreasonable to think that winds could transport such material further inland. If continental shelves are viable sources of far-field dust, the surface area over which dust could be generated is massive in comparison to the relatively small footprint of mountain glaciers.

In comparing Burial Lake S-Ratios to relative sea level (Fig. 2.9; Clark et al., 2009) we observe only a moderate amount of dust accumulation occurring in the earliest part of the record, during MIS-3, in keeping with somewhat elevated sea level (roughly 70 m below present). As sea level declined, subaerial extent of continental shelves increased until sea level reached its lowest position (-123 m) at approximately 21 ka (maximum low-stand shelf exposure is depicted in Fig. 2.10). S-Ratios respond accordingly, reflecting an increase in dust input to Burial Lake. Clark et al. (2009) note that the initial phase of sea level regression towards the LGM is coincident with the earliest global ice-sheet last glacial maxima (33-29 ka), likely forced by a combination of high northern latitude insolation, tropical Pacific sea surface temperatures (SSTs), and atmospheric CO_2. Consistent with these observations, summer insolation (Fig. 2.9; Berger and Loutre, 1991) declines in similar fashion to sea level, and also accompanies increasing S-Ratios. Solar insolation is therefore shown to play a dominant role in Northern Hemisphere climate during the last glacial period, and through regulating global ice volume (and in turn, sea level), appears to have an indirect control on the availability of far-field dust sources on exposed shelves, and the ensuing record of dust input to Burial Lake.

The Deglacial Transition (Subunit 2) 19.4 – 9.8 ka

The lithologic transition, here characterized by decreasing magnetic concentration and CT density, accompanied by rising organic content and BSi (Fig. 2.8), is commonly observed in sediment records that span the glacial/interglacial transition. The beginning of the transition (19.4 ka) is coincident with the onset of Northern Hemisphere deglaciation (Clark et al., 2009; 2012). Termination of the LGM is led by increased northern high latitude insolation (Fig. 2.9), which Clark et al. (2009) suggest is the primary mechanism for triggering widespread ice-margin retreat and rapid mass-loss on mountain glaciers through increased summer ablation. The Noatak Basin likely

experienced warming and increases in effective moisture, leading to the observed rise in terrestrial and aquatic productivity (as evidenced by organic content and BSi; Fig. 2.8). Concentration dependent magnetic parameters decrease (Fig. 2.8), partially in response to organic/biogenic dilution of lithogenic sediments. However, dwindling sedimentation rates (Fig. 2.2) imply a decline in detrital flux as well, which S-Ratios (Fig. 2.8) suggest is in large part due to a reduction in low coercivity aeolian dust contribution. As many of the harsh conditions, once favorable to landscape deflation and production of dust during the glacial period, were ameliorated following the LGM, dust sources were effectively shut off from Burial Lake, permitting Holocene sedimentation to be dominated by local high-coercivity input.

Though Burial Lake begins to respond to global climate changes at ~19.4 ka, the major decrease in S-Ratios between 16 and 12.6 ka, is broadly synchronous with the onset of the Bølling interstadial at 14.7 ka (Rasmussen et al., 2006), identified in $\delta^{18}O$ temperature proxy records from Greenland NGRIP ice cores (Fig. 2.9; NGRIP project members, 2004), and in tune with rising summer insolation (Fig. 2.9; Berger and Loutre, 1991). This is consistent with regional proxy data that reflect a local expression of Bølling warming and a rapid climatic teleconnection between the North Atlantic and North Pacific sectors (Broeker, 1994; Mikolajwicz et al., 1997; Hostetler et al., 1999; Davies et al., 2011). Marine records of $\delta^{18}O$ from the Gulf of Alaska (Davies et al., 2011) show warming and/or freshening of surface waters at 14.7 ka. The pollen-based study for eastern Beringia (Viau et al., 2008) shows rising mean annual temperatures beginning at 16 ka, and reaching a maximum around 12 ka. A rapid ~18 m rise in water levels at Birch Lake at ~15 ka (Fig. 2.9; Abbott et al., 2000) indicates warmer temperatures and increased moisture availability, as does evidence from other small lakes in Alaska, which began accumulating sediment between 15 and 13 ka (e.g., Ager, 1982; Bigelow, 1997; 2001; Carlson and Finney, 2004; Wooler et al., 2012). In summary, available evidence suggests that the landscape response to a more amiable climate may explain the reduction in dust input to Burial Lake during the deglacial transition. S-Ratios make a brief return to higher values between 12.6 and 9.8 ka, broadly coinciding with a period of fluctuating water levels in Birch Lake (Fig. 2.9; Abbott et al., 2000), and indicating a return to slightly drier conditions and increasing dustiness during the later

stages of the transition. Bigelow et al. (1990) identified an increase in wind intensity between 13 and 12.6 ka from grain size variations in loess sequences along the Nenana River, which is in general agreement with this period of renewed dust deposition at Burial Lake.

Unlike for the glacial period, the glacial chronology of the Brooks Range during the transition is at times in phase with S-Ratios, and therefore we are unable to rule out alpine glaciers as potential mediators of dustiness in the Noatak Basin. The time-distance diagram for glaciers in the Brooks Range (Fig. 2.9; Briner and Kaufman, 2008) demonstrates that Itkillik II advances had largely withdrawn by the time of the first S-Ratios drop at 16 ka. Accordingly, Hamilton (1982) observed that alluviation of outwash streams in the Koyakuk River area on the south side of the range had ceased by 15 ka. Cosmogenic ^{10}Be exposure dating within the Kurupa and Antigun River valleys in the north-central Brooks Range shows evidence for ice retreat from the northern range prior to 15.9 ka, with glaciers disappearing entirely, or retreating into individual cirques by 13.8 ka (Fig. 2.9; Badding et al., 2012). Diminished glacial silt production from local glaciers could therefore elucidate the major coercivity change that we observe in Burial Lake at around the same time. Still, this would imply that dust from nearby glaciers is magnetically distinct from terrestrial runoff derived from the same general area (i.e., low-coercivity vs. high-coercivity), a perplexity that leads us to favor a more widespread or far-field diminishing source of dust. Late Itkillik II readvances took place in the north-central Brooks Range between 15.1 and 13.3 ka (Fig. 2.9; Hamilton 2003). Briner and Kaufman (2008) show this readvance to be minor in comparison to previous advances during the glacial period (Fig. 2.9). End moraines were deposited at about this time in the Delong Mountains, but no evidence has been found to suggest a readvance in the upper Noatak River valley (Hamilton, 2010). The readvance appears to have contributed little to S-Ratios, instead corresponding to elevated water levels at Birch Lake (Fig. 2.9; Abbott et al., 2000), implying that increased moisture may have nourished readvancement in areas that remained cold enough to support glaciers or received ample winter snowfall to withstand summer ablation. A lack of evidence for ice advance between 12.6 and 9.8 ka, suggests that general aridity and an increase in wind intensity are more likely responsible for dust emissions during this time.

Rising sea level and the rapid inundation of continental shelves may be largely responsible for a reduction in far-field derived dust input to Burial Lake, and also may explain the delayed response of S-Ratios from the start of the deglacial Transition and the initial rise in summer insolation (Fig. 2.9). Although sea level began to rise ~21 ka (Fig. 2.9; Clark et al., 2009), S-Ratios do not appear to respond until 16 ka. The corresponding ~18 m rise in sea level, however, translates to a rather small surface area reduction of the continental shelf, thus subtracting little from their total potential generation of dust (see Figure 2.10 for paleo shorelines contoured according to the timing of major changes in S-Ratios). The ~45 m of rise between 16 and 12 ka (Fig. 2.9), however, inundated a significant portion of Beringia (Fig. 2.10), and likely had a greater impact on dust availability and the magnetic proportions in Burial Lake. While sea level appears to maintain a higher order control on dust availability, it does not fully describe S-Ratios over the entirety of the transition. For example, the return to slightly drier and dustier conditions at Burial Lake between 12.6 and 9.8 ka occurs despite a ~22 m rise in sea level (Fig. 2.9), and a significant loss in land area (Fig. 2.10). Regional glacial isostatic adjustment (GIA) may have had significant effects on paleo-topography during the deglacial transition (Glenn Milne, personal communication, June 21, 2013), and will need to be ultimately considered in any quantitative evaluations of the timing and area extent of potential dust sources on continental shelves with respect to sea level rise.

The Holocene (Subunit 3) 9.8 ka – present

S-Ratios decrease again between 9.8 and 6.7 ka, attaining their lowest values in the mid-Holocene and implying a continued diminishing input of dust (Fig. 2.8). Values remain low and stable throughout the mid-Holocene, but increase again between ~2 ka and the present, suggesting a slight recent intensification of dustiness in the late Holocene (Fig. 2.8). Low CT density and low magnetic concentration observed throughout the Holocene interval (Fig. 2.8) is interpreted largely as a function of dilution from high organic matter and rising BSi (Fig. 2.8). Along with the general abundance of terrestrial macrofossils for AMS radiocarbon analysis (Fig. 2.2), these data are characteristic of a warmer, more quiescent Holocene environment, with increased terrestrial and aquatic productivity, and enhanced precipitation.

Proxy data from Burial Lake support existing evidence for continued climatic amelioration during the Holocene. The peak in organic content at ~10.5 ka (just before the Holocene interval; Fig. 2.8) roughly coincides with peak summer insolation at (Fig. 2.9; Berger and Loutre, 1991) and with the reopening of the Bering Strait around 11 ka (Elias et al., 1997), which likely facilitated the transport of maritime air masses into interior Alaska. Birch Lake displays evidence for rising lake levels, approaching overflow conditions between 10 and 9 ka (Fig. 2.9), indicating an increase in effective moisture (Abbott et al., 2000). These conditions are again likely to have prevented landscape deflation, further reducing dust emissions, and contributing to the early to mid-Holocene decline in S-Ratios.

Following the readvance of glaciers between 15.1 and 13.3 ka (Fig. 2.9; Hamilton, 2003), no further Itkillik II glacial activity is reported for the Brooks Range (Fig. 2.9). The decline in S-Ratios between 9.8 and 6.7 ka (Fig. 2.9), therefore cannot represent the immediate cessation of dust production from glacial abrasion. The continued alluviation of material from glacial catchments following retreat could contribute a local source of dust to Burial Lake, which would decline over time as source material dwindled. However, Hamilton (1986; 2009) observed that post-Itkillik basin-filling had commenced by about 12.5 ka in some valleys of the central Brooks Range - too early to fully explain the decline in S-Ratios that extends well into the mid-Holocene.

Given the rather gentle sloping topography of the remaining portions of the Beringian Steppe, sea level rise, on the order of 37 m between 9.8 and 6.7 ka (Fig. 2.9; Clark et al., 2009), corresponded to a massive reduction in land area (Fig. 2.10), and could very well explain the early to mid-Holocene decline in dust input at Burial Lake. Though paleo-shorelines are binned from 10 ka to present in Figure 2.10, nearly all of the remaining area was inundated before ~7 ka, when sea level stabilized and Alaskan shorelines approached their present-day configurations. Intriguingly, S-Ratios stabilize around the same time (Fig. 2.9), hinting at a possible causal relationship. Sea level rise, however, is likely not the sole cause of dust emissions in the Holocene, given that the late Holocene increase in S-Ratios ~2 ka, occurs after sea level had already stabilized (Fig. 2.9).

This recent intensification of dustiness implied by increasing S-Ratios from ~2 ka is also difficult to rationalize given the available proxy evidence that indicates wet, warm, and stable climatic conditions for central Alaska in the last few millennia. Other than S-Ratios, down-core physical, geochemical, and magnetic parameters do not appear to show any substantial deviation that would indicate a sudden trend towards a more arid environment (Fig. 2.8). Sedimentation rates do increase towards the late Holocene (Fig. 2.2), but this does not appear to be linked to an increase in calculated detrital flux. Water levels at Birch lake appear stable, at near-overflow level (Fig. 2.9), with sedimentary evidence suggesting a late Holocene moist phase persisting throughout the last ~5.5 ka (Abbott et al., 2000). Summer insolation and NGRIP $\delta^{18}O$ do exhibit declining trends which are in phase with S-Ratios (Fig. 2.9), but as the only supporting evidence for deteriorating climatic conditions in the recent past, we do not suspect they contributed much towards the suddenly dustier conditions.

Cosmogenic ^{10}Be exposure dates provided by Badding et al. (2012) demonstrate that late Holocene (Neoglacial) advances took place in the Kurupa and Antigun River valleys, which formed pre-LIA (Little Ice Age) moraine crests between 4.6 and 2.7 ka (Fig. 2.9). This is in agreement with previously published lichen-inferred ages (Ellis and Calkin, 1984), which confirm that glaciers in the Brooks Range experienced multiple similar Neoglacial advances (Fig. 2.9). It is conceivable then, that these Neoglacial advances supplied Burial Lake with local aeolian material, triggering the late Holocene increase in S-Ratios. Barclay et al. (2009) report Neoglacial advances for glaciers in southeast Alaska occurring as as early as 4.5-4.0 ka, with major advances underway by 3.0 ka. They also describe the subsequent LIA advance as the largest Holocene expansion in southern Alaska, with ice-volumes sufficiently large enough to cause major glacio-isostatic depression and rebound (Larsen et al., 2005). Since the largest glaciers and ice fields of Alaska are confined to southern mountain ranges (and glaciers are more limited in the Brooks Range), we must consider them a potential far-field, glaciogenic source of dust to Burial Lake. Though we are currently unable to magnetically type such a source, it may better conform to our description of a low-coercivity mineralogy, than does known high-coercivity material from the Brooks Range. Though Barclay et al. (2009) also describe advances for tidewater glaciers along the coastal rim of the Gulf of

Alaska that occur throughout the Holocene, the majority of eroded material from these systems would intuitively be lost to the marine environment, and be unavailable for aeolian transport. Therefore, we conclude that if a far-field source of dust from southern Alaska exists, it would need to be generated mainly from valley or cirque glaciers with land-based termini.

2.8 Conclusions

We extend our understanding of paleo-environmental variability across the Alaskan Arctic through a detailed study of Burial Lake sediments. This ~37,000-yr record can be subdivided into three lithologic subunits based on observed physical, geochemical, and rock magnetic changes. The marked decrease in magnetic concentration observed through the deglacial transition, is partly attributed to biogenic/organic dilution as cold, windy, and dry glacial period conditions gave way to a warmer, more productive Holocene climate with increased moisture availability. The two main detrital constituents of Burial Lake sediments are mineralogically distinct and can be classified according to their rock magnetic characteristics. The low-coercivity magnetic component is interpreted as magnetite-rich sediment that arrives via aeolian deposition of dust. The high-coercivity component is interpreted as a local influx of detrital minerals, weathered from surrounding bedrock, and arriving via terrestrial seasonal runoff. Down-core rock magnetic variability indicates significant provenance changes, which we suspect are mainly driven by variable inputs of aeolian dust. The diminished relative contribution of the low-coercivity ferrimagnetic component from the glacial period to the Holocene, along with a 4.5-fold reduction in detrital flux, suggests the decrease in magnetic concentration is also largely attributed to a decrease in clastic aeolian flux.

Taking advantage of a well-constrained chronology and a simple depositional environment, we compare the timing and extent of aeolian deposition in Burial Lake with regional proxy data to constrain regional and far-field sources of dust and identify the possible forcing mechanisms that control its production, availability, transport, and deposition. The climatic amelioration associated with the deglacial transition appears to have limited landscape deflation that likely supplied Burial Lake with a widespread

source of dust during the glacial period. The similarity of S-Ratios to regional lake level reconstructions suggests that dust input is regulated to a large degree by general aridity. If this is the case, then perhaps S-Ratios can be used elsewhere in Alaska to estimate dust flux and general aridity at a much higher resolution. Regardless, environmental magnetic techniques add a needed dimension to ongoing paleoclimate research in Alaska.

Although the Alaskan loess is typically assumed to be glaciogenic in origin, we at times observe little correlation between dust input in Burial Lake and regional glacial activity. This suggests that regional glaciers in the Brooks Range may not be the sole contributors of dust to Burial Lake, or that its availability for transport and its timing of deposition is more broadly dependent on regional climate.

Lastly, the similarity of S-Ratios to relative sea level demonstrates the significance of newly exposed continental shelves as a potential far-field source of dust to interior Alaska. Future studies of terrestrial loess deposits should therefore consider continental shelves as a viable source of dust, which may communicate valuable long-range paleo-environmental signals.

2.9 References

Abbott, M.B., Edwards, M.E., Finney, B.P., 2010. A 40,000-yr record of environmental change from Burial Lake in Northwest Alaska. Quaternary Research 74, 156–165.

Abbott, M.B., Finney, B.P., Edwards, M.E., Kelts, K.R., 2000. Lake-Level Reconstruction and Paleohydrology of Birch Lake, Central Alaska, Based on Seismic Reflection Profiles and Core Transects. Quaternary Research 53, 154–166.

Ager, T.A., 1975. Late quaternary environmental history of the Tanana Valley, Alaska. Research Foundation and the Institute of Polar Studies, The Ohio State University, Columbus, Ohio.

Anderson, N., Rippey, B., 1988. Diagenesis of magnetic minerals in the recent sediments of a eutrophic lake. Limnology and Oceanography 1476–1492.

Badding, M.E., Briner, J.P., Kaufman, D.S., 2013. 10Be ages of late Pleistocene deglaciation and Neoglaciation in the north-central Brooks Range, Arctic Alaska. J. Quaternary Sci. 28, 95–102.

Barclay, D.J., Wiles, G.C., Calkin, P.E., 2009. Holocene glacier fluctuations in Alaska. Quaternary Science Reviews 28, 2034–2048.

Begét, J.E., 1990. Middle Wisconsinan Climate Fluctuations Recorded in Central Alaskan Loess. Géographie physique et Quaternaire 44, 3–13.

Begét, J.E., 2001. Continuous Late Quaternary proxy climate records from loess in Beringia. Quaternary Science Reviews 20, 499–507.

Begét, J.E., Stone, D.B., Hawkins, D.B., 1990. Paleoclimatic forcing of magnetic susceptibility variations in Alaskan loess during the late Quaternary. Geology 18, 40–43.

Berger, A., Loutre, M.F., 1991. Insolation values for the climate of the last 10 million years. Quaternary Science Reviews 10, 297–317.

Bigelow, N., Begét, J., Powers, R., 1990. Latest Pleistocene increase in wind intensity recorded in eolian sediments from central Alaska. Quaternary Research 34, 160–168.

Bigelow, N.H., 1997. Late-Quaternary climate and vegetation in interior Alaska. University of Alaska, Fairbanks, Fairbanks, AK.

Bigelow, N.H., Edwards, M.E., 2001. A 14,000 yr paleoenvironmental record from Windmill Lake, Central Alaska: Lateglacial and Holocene vegetation in the Alaska range. Quaternary Science Reviews 20, 203–215.

Bird, B., Abbott, M., Finney, B., Kutchko, B., 2009. A 2000 year varve-based climate record from the central Brooks Range, Alaska. J Paleolimnol 41, 25–41.

Blaauw, M., 2010. Methods and code for "classical" age-modelling of radiocarbon sequences. Quaternary Geochronology 5, 512–518.

Blott, S.J., Pye, K., 2001. GRADISTAT: a grain size distribution and statistics package for the analysis of unconsolidated sediments. Earth Surf. Process. Landforms 26, 1237–1248.

Briner, J.P., Kaufman, D.S., 2008. Late Pleistocene mountain glaciation in Alaska: key chronologies. J. Quaternary Sci. 23, 659–670.

Broecker, W.S., 1994. Massive iceberg discharges as triggers for global climate change. Nature 372, 421–424.

Carlson, L.J., Finney, B.P., 2004. A 13 000-year history of vegetation and environmental change at Jan Lake, east-central Alaska. Holocene 14, 818–827.

Clark, P.U., Dyke, A.S., Shakun, J.D., Carlson, A.E., Clark, J., Wohlfarth, B., Mitrovica, J.X., Hostetler, S.W., McCabe, A.M., 2009. The Last Glacial Maximum. Science 325, 710–714.

Clark, P.U., Shakun, J.D., Baker, P.A., Bartlein, P.J., Brewer, S., Brook, E., Carlson, A.E., Cheng, H., Kaufman, D.S., Liu, Z., Marchitto, T.M., Mix, A.C., Morrill, C., Otto-Bliesner, B.L., Pahnke, K., Russell, J.M., Whitlock, C., Adkins, J.F., Blois, J.L., Clark, J., Colman, S.M., Curry, W.B., Flower, B.P., He, F., Johnson, T.C., Lynch-Stieglitz, J., Markgraf, V., McManus, J., Mitrovica, J.X., Moreno, P.I., Williams, J.W., 2012. Global climate evolution during the last deglaciation. Proceedings of the National Academy of Sciences.

Davies, M.H., Mix, A.C., Stoner, J.S., Addison, J.A., Jaeger, J., Finney, B., Wiest, J., 2011. The deglacial transition on the southeastern Alaska Margin: Meltwater input, sea level rise, marine productivity, and sedimentary anoxia. Paleoceanography 26, PA2223.

Day, R., Fuller, M., Schmidt, V., 1977. Hysteresis properties of titanomagnetites: grain-size and compositional dependence. Physics of the Earth and Planetary Interiors 13, 260–267.

Dekkers, M.J., 1997. Environmental magnetism: an introduction. Geologie en Mijnbouw 76, 163–182.

Dunlop, D.J., Özdemir, Ö., 2001. Rock magnetism: fundamentals and frontiers. Cambridge University Press.

Elias, S.A., Hamilton, T.D., Edwards, M.E., Begét, J.E., Krumhardt, A.P., Lavoie, C., 1999. Late Pleistocene environments of the western Noatak basin, northwestern Alaska. Bull Geol Soc Am 111, 769–789.

Elias, S.A., Short, S.K., Birks, H.H., 1997. Late Wisconsin environments of the Bering Land Bridge. Palaeogeography, Palaeoclimatology, Palaeoecology 136, 293–308.

Ellersieck, I., Curtis, S.M., Mayfield, C.F., and Tailleur, I.L., 1984, Reconnaissance geologic map of south-central Misheguk Mountain Quadrangle, Alaska: U.S. Geological Survey Miscellaneous Investigations Series Map 1504, 2 sheets, scale 1:63,360.

Ellis, J.M., Calkin, P.E., 1984. Chronology of Holocene glaciation, central Brooks Range, Alaska. Geological Society of America Bulletin 95, 897–912.

Evans, M.E., Jensen, B.J.L., Kravchinsky, V.A., Froese, D.G., 2011. The Kamikatsura event in the Gold Hill loess, Alaska. Geophys. Res. Lett. 38, L13302.

Evans, M.M.E., Heller, F.A., 2003. Environmental magnetism:, International geophysics series. Academic Press, Incorporated.

Farrians, O., J., 1965. Permafrost map of Alaska: U.S. Geological Survey Miscellaneous Geologic Investigations Map I-445.

Finkenbinder, M.S., Abbott, M.B., Stoner, J.S., Dorfman, J.M., (*in prep*), A multi-proxy geochemical investigation of late-Quaternary paleoenvironmental change from Burial Lake, Noatak National Preserve, Alaska.

Frank, U., Nowaczyk, N.R., 2008. Mineral magnetic properties of artificial samples systematically mixed from haematite and magnetite. Geophysical Journal International 175, 449–461.

Hamilton, T.D., 1982. A late Pleistocene glacial chronology for the southern Brooks Range: Stratigraphic record and regional significance. Geological Society of America Bulletin 93, 700–716.

Hamilton, T.D., 1994, Late Cenozoic glaciation of Alaska, in Plafker, George, and Berg, H.C., The Geology of Alaska: Geological Society of America, p. 813-844.

Hamilton, T.D., 2001. Quaternary glacial, lacustrine, and fluvial interactions in the western Noatak basin, Northwest Alaska. Quaternary Science Reviews 20, 371–391.

Hamilton, T.D., 2003. Surficial geology of the Dalton Highway (Itkillik-Sagavanirktok Rivers) area, southern Arctic foothills, Alaska. Alaska Dept. of Natural Resources, Division of Geological and Geophysical Surveys, [Fairbanks, Alaska].

Hamilton, T.D., 2009, Guide to surficial geology and river-bluff exposures, Noatak National Preserve, northwestern Alaska: U.S. Geological Survey Scientific Investigations Report 2008-5125, 116 p. [http://pubs.usgs.gov/sir/2008/5125/].

Hamilton, T.D., 2010, Surficial geologic map of the Noatak National Preserve, Alaska: U.S. Geological Survey Scientific Investigations Map 3036, 1 sheet, scale 1:250,000, 1 pamphlet, 21 p.

Hamilton, T.D., and Labay, K.A., 2011, Surficial geologic map of the Gates of the Arctic National Park and Preserve, Alaska: U.S. Geological Survey Scientific Investigations Map 3125, pamphlet 19 p., scale 1:300,000, available at http://pubs.usgs.gov/sim/3125/.

Hamilton, T.D., Van Etten, D.P., 1984. Late Pleistocene glacial dams in the Noatak valley. In: Coonrad, W.L., Elliott, R.L. (Eds.), The United States Geological Survey in Alaska: Accomplishments During 1981. U.S. Geol. Survey Circular 868, pp. 21-23.

Heslop, D., Dekkers, M.J., Kruiver, P.P., Van Oorschot, I.H.M., 2002. Analysis of isothermal remanent magnetization acquisition curves using the expectation–maximization algorithm. Geophysical Journal International 148, 58–64.

Hopkins, D.M., 1982. Aspects of the paleogeography of Beringia during the late Pleistocene. Paleoecology of Beringia. Academic Press, New York 3–28.

Hostetler, S.W., Clark, P.U., Bartlein, P.J., Mix, A.C., Pisias, N.J., 1999. Atmospheric transmission of North Atlantic Heinrich events. J. Geophys. Res. 104, 3947–3952.

Hutchins, D.A., Bruland, K.W., 1998. Iron-limited diatom growth and Si:N uptake ratios in a coastal upwelling regime. Nature 393, 561–564.

Huybers, P., Wunsch, C., 2004. A depth-derived Pleistocene age model: Uncertainty estimates, sedimentation variability, and nonlinear climate change. Paleoceanography 19, PA1028.

Imbrie, J., Northwestern University (Evanston, I.), Research, U.S.O. of N., 1963. Factor and Vector Analysis Programs for Analyzing Geologic Data. Northwestern University.

Karlin, R., and Levi, S., 1983. Diagenesis of magnetic minerals in recent hemipelagic sediments. Nature 303: 327-330.

King, J.W., and Channel, J.E.T., 1991, Sedimentary magnetism, environmental magnetism, and magnetostratigraphy: Reviews of Geophysics, Supplement, p. 358-370.

Kohfeld, K.E., Harrison, S.P., 2001. DIRTMAP: the geological record of dust. Earth-Science Reviews 54, 81–114.

Kurek, J., Cwynar, L.C., Ager, T.A., Abbott, M.B., Edwards, M.E., 2009. Late Quaternary paleoclimate of western Alaska inferred from fossil chironomids and its relation to vegetation histories. Quaternary Science Reviews 28, 799–811.

Lagroix, F., Banerjee, S.K., 2002. Paleowind directions from the magnetic fabric of loess profiles in central Alaska. Earth and Planetary Science Letters 195, 99–112.

Larsen, C.F., Motyka, R.J., Freymueller, J.T., Echelmeyer, K.A., Ivins, E.R., 2005. Rapid viscoelastic uplift in southeast Alaska caused by post-Little Ice Age glacial retreat. Earth and Planetary Science Letters 237, 548–560.

Liu, X.M., Hesse, P., Rolph, T., Begét, J.E., 1999. Properties of magnetic mineralogy of Alaskan loess: evidence for pedogenesis. Quaternary International 62, 93–102.

Lowrie, W., 1990. Identification of ferromagnetic minerals in a rock by coercivity and unblocking temperature properties. Geophys. Res. Lett. 17, 159–162.

Marcott, S.A., Shakun, J.D., Clark, P.U., Mix, A.C., 2013. A Reconstruction of Regional and Global Temperature for the Past 11,300 Years. Science 339, 1198–1201.

Mayfield, C.F., Curtis, S.M., Ellersieck, I., and Tailleur, I.L., 1984, Reconnaissance geologic map of southeastern Misheguk Mountain Quadrangle, Alaska: U.S.

Geological Survey Miscellaneous Investigations Series Map 1503, 2 sheets, scale 1:63,360.

Mikolajewicz, U., Crowley, T.J., Schiller, A., Voss, R., 1997. Modelling teleconnections between the North Atlantic and North Pacific during the Younger Dryas. Nature 387, 384–387.

Muhs, D.R., Ager, T.A., Arthur Bettis III, E., McGeehin, J., Been, J.M., Begét, J.E., Pavich, M.J., Stafford Jr., T.W., Stevens, D.A.S.P., 2003a. Stratigraphy and palaeoclimatic significance of Late Quaternary loess–palaeosol sequences of the Last Interglacial–Glacial cycle in central Alaska. Quaternary Science Reviews 22, 1947–1986.

Muhs, D.R., Ager, T.A., Been, J., Bradbury, J.P., Dean, W.E., July 2003b. A late quaternary record of eolian silt deposition in a maar lake, St. Michael Island, western Alaska. Quaternary Research 60, 110–122.

Muhs, D.R., Budahn, J.R., 2006. Geochemical evidence for the origin of late Quaternary loess in central Alaska. Can. J. Earth Sci. 43, 323–337.

North Greenland Ice Core Project members, 2004. High-resolution record of Northern Hemisphere climate extending into the last interglacial period. Nature 431, 147–151.

Oswald, W.W., Anderson, P.M., Brown, T.A., Brubaker, L.B., Feng Sheng Hu, Lozhkin, A.V., Tinner, W., Kaltenrieder, P., 2005. Effects of sample mass and macrofossil type on radiocarbon dating of arctic and boreal lake sediments. Holocene 15, 758–767.

Péwé, T.L., 1955. Origins of the upland silt near Fairbanks, Alaska. Geological Society of America Bulletin 66, 699–724.

Rasmussen, S.O., Andersen, K.K., Svensson, A.M., Steffensen, J.P., Vinther, B.M., Clausen, H.B., Siggaard-Andersen, M.-L., Johnsen, S.J., Larsen, L.B., Dahl-Jensen, D., Bigler, M., Röthlisberger, R., Fischer, H., Goto-Azuma, K., Hansson, M.E., Ruth, U., 2006. A new Greenland ice core chronology for the last glacial termination. J. Geophys. Res. 111, D06102.

Rea, D.K., 1994. The paleoclimatic record provided by eolian deposition in the deep sea: The geologic history of wind. Rev. Geophys. 32, 159–195.

Reimer, P.J., Baillie, M.G.L., Bard, E., Bayliss, A., Beck, J.W., Blackwell, P.G., Ramsey, C.B., Buck, C.E., Burr, G.S., Edwards, R.L., Friedrich, M., Grootes, P.M., Guilderson, T.P., Hajdas, I., Heaton, T.J., Hogg, A.G., Hughen, K.A., Kaiser, K.F., Kromer, B., McCormac, F.G., Manning, S.W., Reimer, R.W., Richards, D.A., Southon, J.R., Talamo, S., Turney, C.S.M., Plicht, J. van der, Weyhenmeyer, C.E., 2011. IntCal09 and Marine09 Radiocarbon Age Calibration Curves, 0-50,000 Years cal BP. Radiocarbon 51, 1111–1150.

Slack, J.F., Dumoulin, J.A., Schmidt, J.M., Young, L.E., Rombach, C.S., 2004. Paleozoic Sedimentary Rocks in the Red Dog Zn-Pb-Ag District and Vicinity, Western Brooks Range, Alaska: Provenance, Deposition, and Metallogenic Significance. Economic Geology 99, 1385–1414.

St-Onge, G., Mulder, T., Francus, P., Long, B., 2007. Chapter Two Continuous Physical Properties of Cored Marine Sediments. Developments in Marine Geology 1, 63–98.

St-Onge, G., Stoner, J.S., Hillaire-Marcel, C., 2003. Holocene paleomagnetic records from the St. Lawrence Estuary, eastern Canada: centennial- to millennial-scale geomagnetic modulation of cosmogenic isotopes. Earth and Planetary Science Letters 209, 113–130.

Stober, J.C., Thompson, R., 1979. An investigation into the source of magnetic minerals in some Finnish lake sediments. Earth and Planetary Science Letters 45, 464–474.

Stoner, J.S., St-Onge, G., 2007. Chapter Three Magnetic Stratigraphy in Paleoceanography: Reversals, Excursions, Paleointensity, and Secular Variation. Developments in Marine Geology 1, 99–138.

Stuiver, M. and Polach, H.A., 1977. Discussion: Reporting of 14C data. Radiocarbon, 19:355-363.

Stuiver, M., Reimer, P. J., and Reimer, R. W. 2005. CALIB 5.0. [program and documentation]. http://calib.qub.ac.uk/calib/

Tauxe, L., 1993. Sedimentary records of relative paleointensity of the geomagnetic field: theory and practice. Reviews of geophysics 31, 319–354.

Tegen, I., Lacis, A.A., Fung, I., 1996. The influence on climate forcing of mineral aerosols from disturbed soils. Nature 380, 419–422.

Thompson, R., Oldfield, F., 1986. Environmental Magnetism. Allen & Unwin.

Viau, A.E., Gajewski, K., Sawada, M.C., Bunbury, J., 2008. Low- and high-frequency climate variability in eastern Beringia during the past 25 000 years. Canadian Journal of Earth Sciences 45, 1435–1453.

Vlag, P.A., Oches, E.A., Banerjee, S.K., Solheid, P.A., 1999. The paleoenvironmental-magnetic record of the Gold Hill Steps loess section in central Alaska. Physics and Chemistry of the Earth, Part A: Solid Earth and Geodesy 24, 779–783.

Wooller, M., Kurek, J., Gaglioti, B., Cwynar, L., Bigelow, N., Reuther, J., Gelvin-Reymiller, C., Smol, J., 2012. An ~11,200 year paleolimnological perspective for emerging archaeological findings at Quartz Lake, Alaska. J Paleolimnol 48, 83–99.

Xuan, C., Channell, J.E.T., 2009. UPmag: MATLAB software for viewing and processing u channel or other pass-through paleomagnetic data. Geochem. Geophys. Geosyst. 10, Q10Y07.

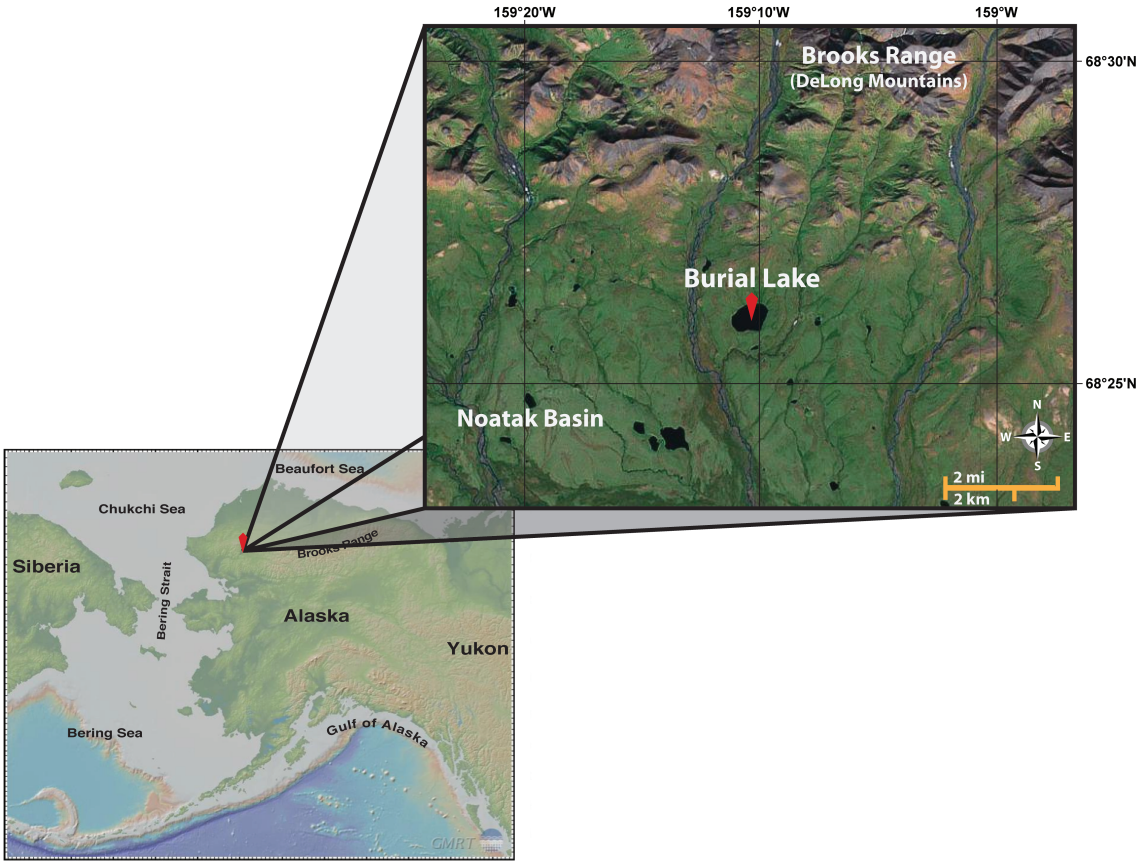

Figure 2.1 – Site location map. Burial Lake (68.43°N, 159.17°W) is located in Noatak Basin in the northwest Brooks Range, Arctic Alaska, at the foot of the DeLong Mountains.

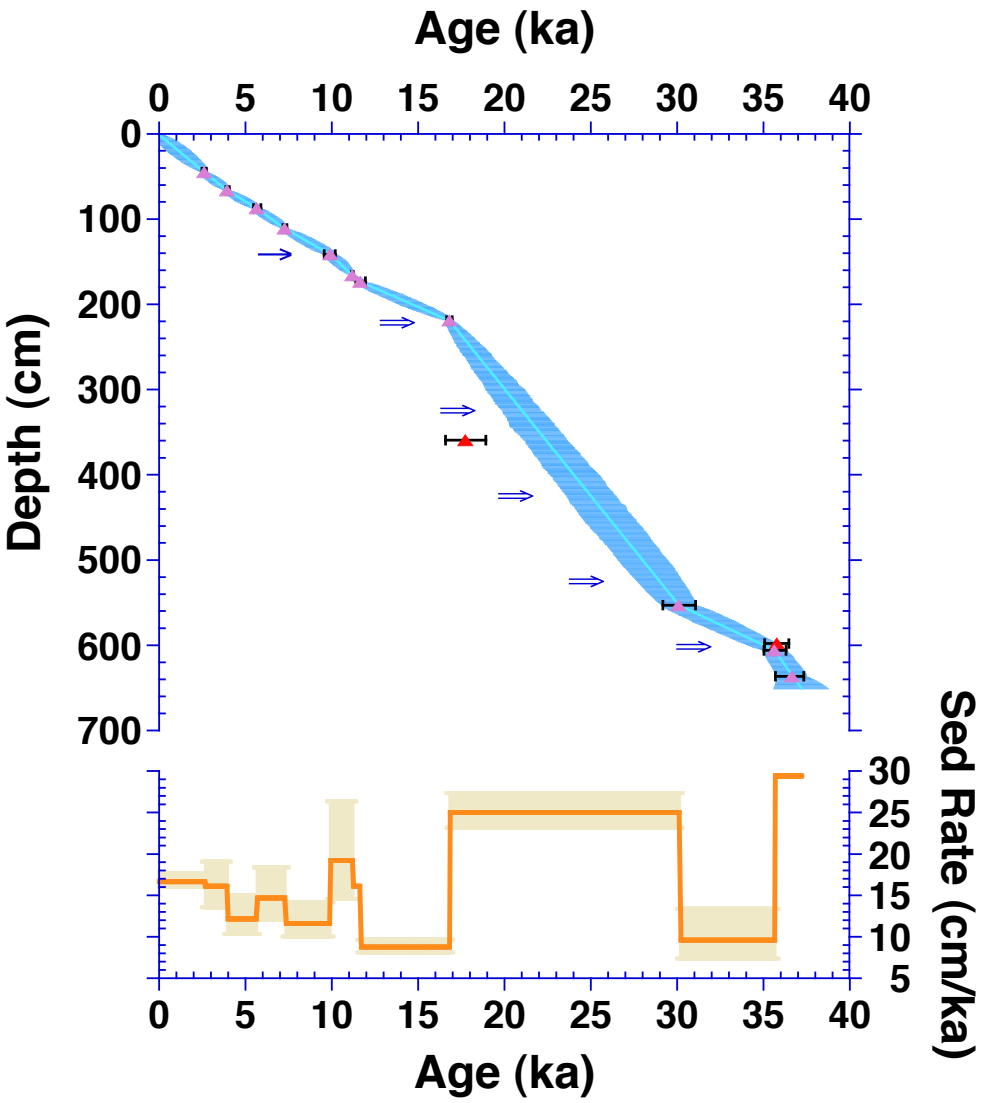

Figure 2.2 – AMS radiocarbon results based on terrestrial macrofossils identified in deep basin cores A10 and C10, which were stratigraphically correlated to produce a composite depth scale (see Appendix A). Radiocarbon ages were calibrated using Calib 6.0 (Stuiver et al., 2005) and the IntCal09 calibration curve (Reimer et al., 2009). Eleven calibrated median radiocarbon ages (pink triangles) are shown with associated 2σ error bars, as well as two dates, which were excluded from the age model (red triangles – see text for explanation). *CLAM* software for "classical" non-Bayesian age-depth modeling (Blaauw, 2010) was used to produce the "best fit" linearly interpolated age (cyan line) for the 6.51 m A10 core. Locations of A10 section breaks are shown for overlapping (→) and abutted (⇒) sections. The blue shaded envelope represents the maximum age variance computed between age control points based on the 2σ calibrated ^{14}C ages. It is the maximum AR1 normalized 1σ standard deviation computed from 10,000 Monte Carlo simulations following a random draw from a normal distribution (Marcott et al., 2013) with uncertainty between age control points based on a random walk model after Huybers and Wunsch, (2004), using a "jitter factor" of 200. The orange line represents sedimentation rate over the ~37,000-year time interval with uncertainty generated using the 2σ calibrated age range of each age control point where feasible.

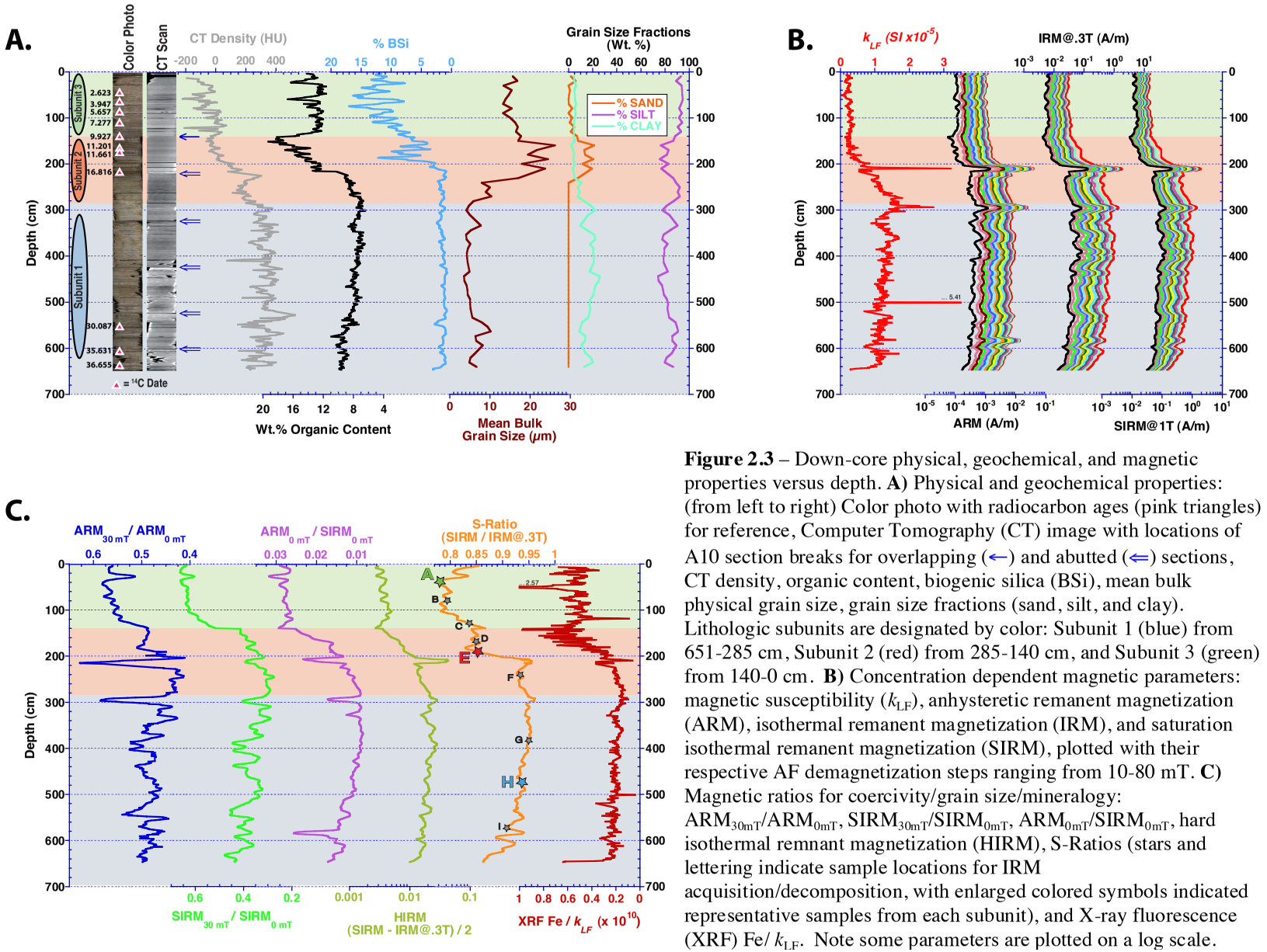

Figure 2.3 – Down-core physical, geochemical, and magnetic properties versus depth. **A)** Physical and geochemical properties: (from left to right) Color photo with radiocarbon ages (pink triangles) for reference, Computer Tomography (CT) image with locations of A10 section breaks for overlapping (←) and abutted (⇐) sections, CT density, organic content, biogenic silica (BSi), mean bulk physical grain size, grain size fractions (sand, silt, and clay). Lithologic subunits are designated by color: Subunit 1 (blue) from 651-285 cm, Subunit 2 (red) from 285-140 cm, and Subunit 3 (green) from 140-0 cm. **B)** Concentration dependent magnetic parameters: magnetic susceptibility (k_{LF}), anhysteretic remanent magnetization (ARM), isothermal remanent magnetization (IRM), and saturation isothermal remanent magnetization (SIRM), plotted with their respective AF demagnetization steps ranging from 10-80 mT. **C)** Magnetic ratios for coercivity/grain size/mineralogy: ARM_{30mT}/ARM_{0mT}, $SIRM_{30mT}/SIRM_{0mT}$, $ARM_{0mT}/SIRM_{0mT}$, hard isothermal remnant magnetization (HIRM), S-Ratios (stars and lettering indicate sample locations for IRM acquisition/decomposition, with enlarged colored symbols indicated representative samples from each subunit), and X-ray fluorescence (XRF) Fe/ k_{LF}. Note some parameters are plotted on a log scale.

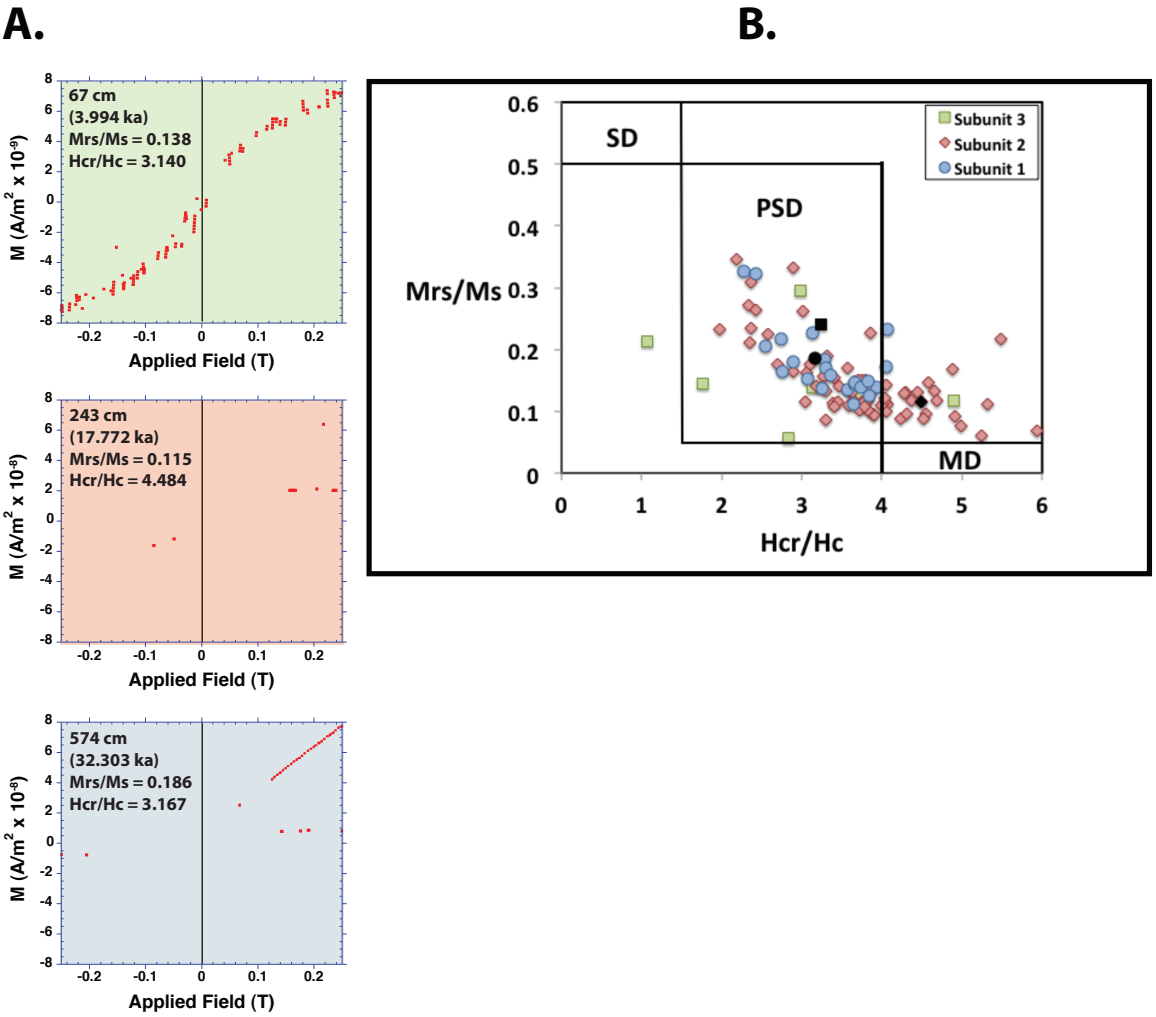

Figure 2.4 – Hysteresis results. **A)** Hysteresis loops generated from alternating gradient magnetometer (AGM) measurements on representative samples from each lithologic subunit. Uncorrected loops are shown (dashed lines) as well as those corrected for high-field paramagnetic/diamagnetic contributions. Shapes of loops demonstrate the presence of low-coercivity ferrimagnetic minerals such as magnetite, and also exhibit significant paramagnetic contributions. Noisy loops in Subunit 3 are indicative of low ferrimagnetic magnetic concentration. **B)** Hysteresis ratios of Hcr/Hc and Mrs/Ms plotted according to Day et al. (1977) for a number of samples within each subunit, and with theoretical domain state (magnetic grain size) boundaries drawn according to the behavior of pure magnetite (Day et al., 1977). Most samples fall within the PSD-MD magnetic grain size rage including values derived from the hysteresis loops depicted here (black symbols), though scatter does occur - likely due to low ferrimagnetic concentration and/or high-coercivity components.

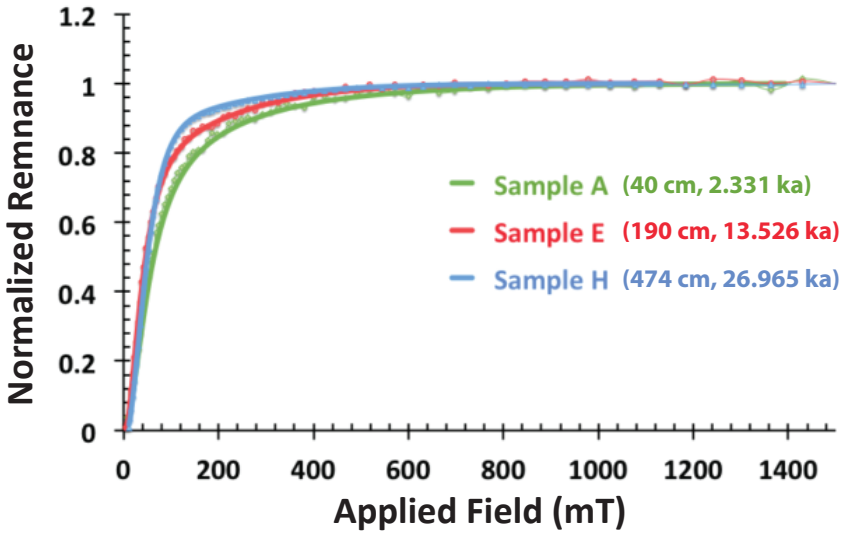

Figure 2.5 – Representative normalized IRM acquisition curves from Subunit 1 (H: 474 cm, 26.965 ka), Subunit 2 (E: 190 cm, 13.526 ka), and Subunit 3 (A: 40 cm, 2.331 ka). Sample A displays higher coercivity behavior than samples E and H, consistent with a distinctive change in mineralogy. Raw data points were smoothed using a MATLAB™ loess filter prior to IRM decomposition as is indicated by the thick solid lines.

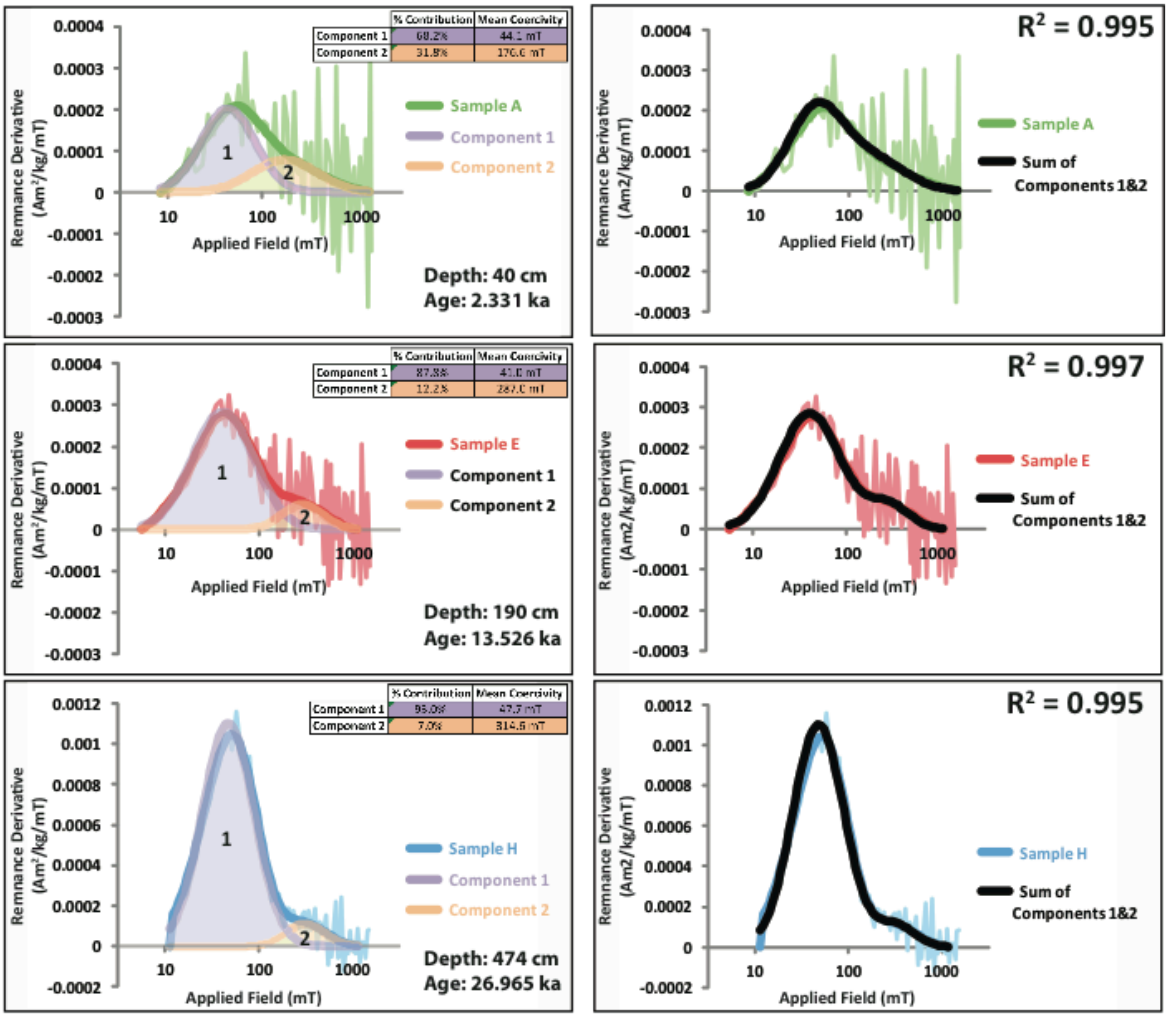

Figure 2.6 – **Left column:** IRM decomposition results based on smoothed data from Figure 2.5. Non-normalized input data for representative samples from Subunit 1 (H), Subunit 2 (E), and Subunit 3 (A) were analyzed using IRMUNMIX V2.2 (Heslop et al., 2002) to decompose curves into their individual component contributions. Raw data is shown behind the smoothed curve for each sample. Note, applied field is plotted on a log scale. Burial Lake sediments are best described by a two-component model, with both low-coercivity and high-coercivity sources present throughout the record. Component 1 (shaded purple) is characteristic of low-coercivity minerals (magnetite), and its relative abundance decreases by ~25% between Subunit 1 and Subunit 3. Component 2 (shaded orange) is characteristic of high-coercivity minerals (hematite) and is ever-present throughout the record, but can easily be masked when component 1 is in high abundance (e.g., sample H in Subunit 1). Relative percent contribution and mean coercivity for each component is tabulated for each sample. Depths and ages for each sample are provided. **Right column:** The sum of components 1 and 2 compared against the smoothed input data, with R^2 values given for each sample, demonstrating an excellent correlation. Raw data is again shown for reference behind the smoothed curves.

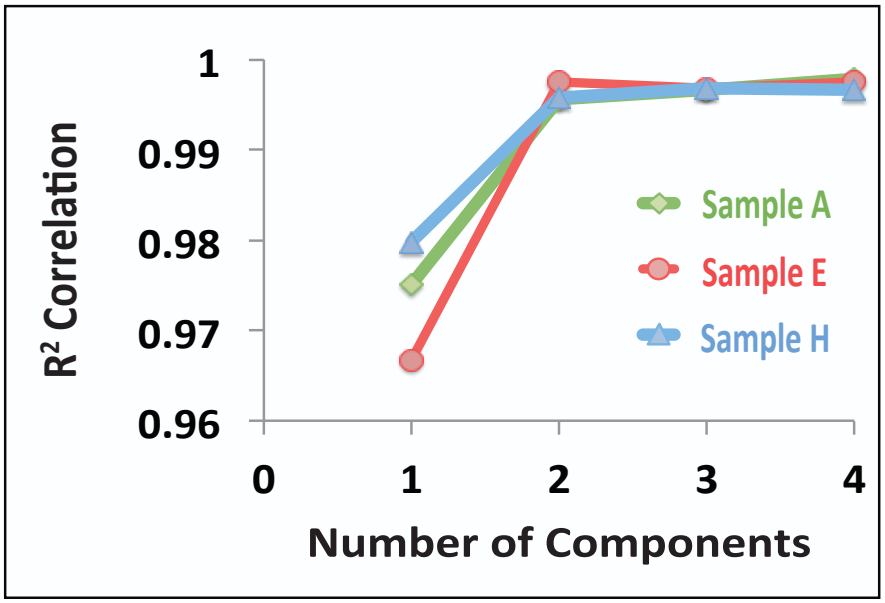

Figure 2.7 – R^2 correlation of smoothed input data to the sum of one, two, three, and four components for samples H, E, and A, representing Subunits 1, 2, and 3, respectively. This supports our use of a two-component model, as R^2 values do not significantly increase for models using more than two components.

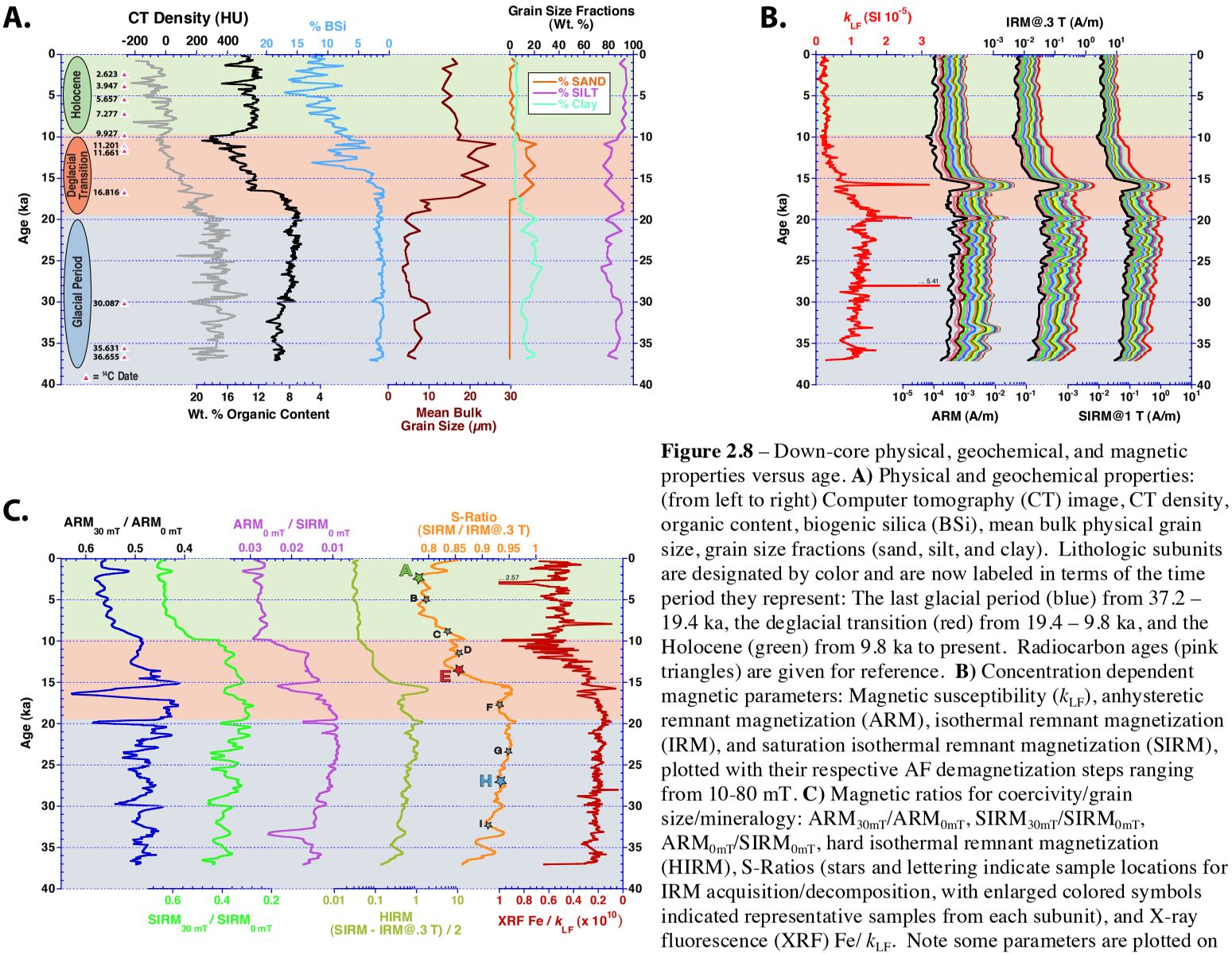

Figure 2.8 – Down-core physical, geochemical, and magnetic properties versus age. **A)** Physical and geochemical properties: (from left to right) Computer tomography (CT) image, CT density, organic content, biogenic silica (BSi), mean bulk physical grain size, grain size fractions (sand, silt, and clay). Lithologic subunits are designated by color and are now labeled in terms of the time period they represent: The last glacial period (blue) from 37.2 – 19.4 ka, the deglacial transition (red) from 19.4 – 9.8 ka, and the Holocene (green) from 9.8 ka to present. Radiocarbon ages (pink triangles) are given for reference. **B)** Concentration dependent magnetic parameters: Magnetic susceptibility (k_{LF}), anhysteretic remnant magnetization (ARM), isothermal remnant magnetization (IRM), and saturation isothermal remnant magnetization (SIRM), plotted with their respective AF demagnetization steps ranging from 10-80 mT. **C)** Magnetic ratios for coercivity/grain size/mineralogy: ARM_{30mT}/ARM_{0mT}, $SIRM_{30mT}/SIRM_{0mT}$, $ARM_{0mT}/SIRM_{0mT}$, hard isothermal remnant magnetization (HIRM), S-Ratios (stars and lettering indicate sample locations for IRM acquisition/decomposition, with enlarged colored symbols indicated representative samples from each subunit), and X-ray fluorescence (XRF) Fe/ k_{LF}. Note some parameters are plotted on a log scale.

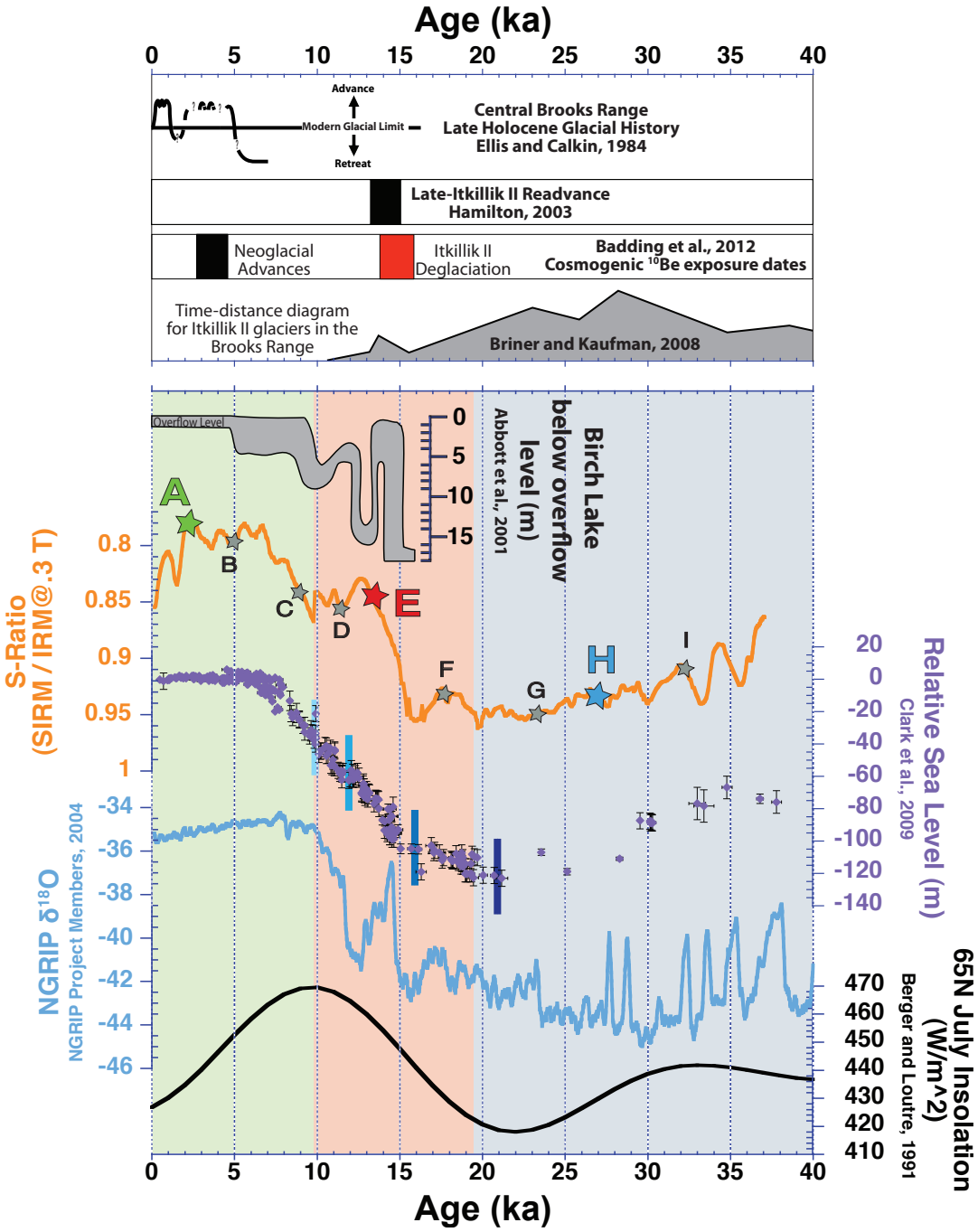

Figure 2.9 – Comparison of Burial Lake S-Ratios with proxy data for regional paleoclimate, glacial history of the Brooks Range, and relative sea level shown on a calibrated age scale. **Upper panel:** (from top to bottom) Lichen-inferred late Holocene glacial history of the central Brooks Range (Ellis and Calkin, 1984), Timing of the late-Itkillik II readvance (Hamilton, 2003), Timing of ice-retreat (red bar) and Neoglacial advances (black bar) in the north-central Brooks range as delimited by cosmogenic ^{10}Be exposure dating (Badding et al., 2012), Time-distance diagram for Itkillik II glaciers in the Brooks range (Briner and Kaufman, 2008). **Lower panel:** (From top to bottom) Lake-level reconstruction for Birch Lake (Abbott et al., 2001), Burial Lake S-Ratios (stars and lettering indicate sample locations for IRM acquisition/decomposition, with enlarged colored symbols indicated representative samples from each subunit), Relative sea level (Clark et al., 2009), NGRIP δ^{18}O (NGRIP project members, 2004), Mid-month July solar insolation reconstructed for 65°N (Berger and Loutre, 1991). Colored vertical bars on the sea level curve correspond to the paleo-shoreline bins shown in Figure 2.10.

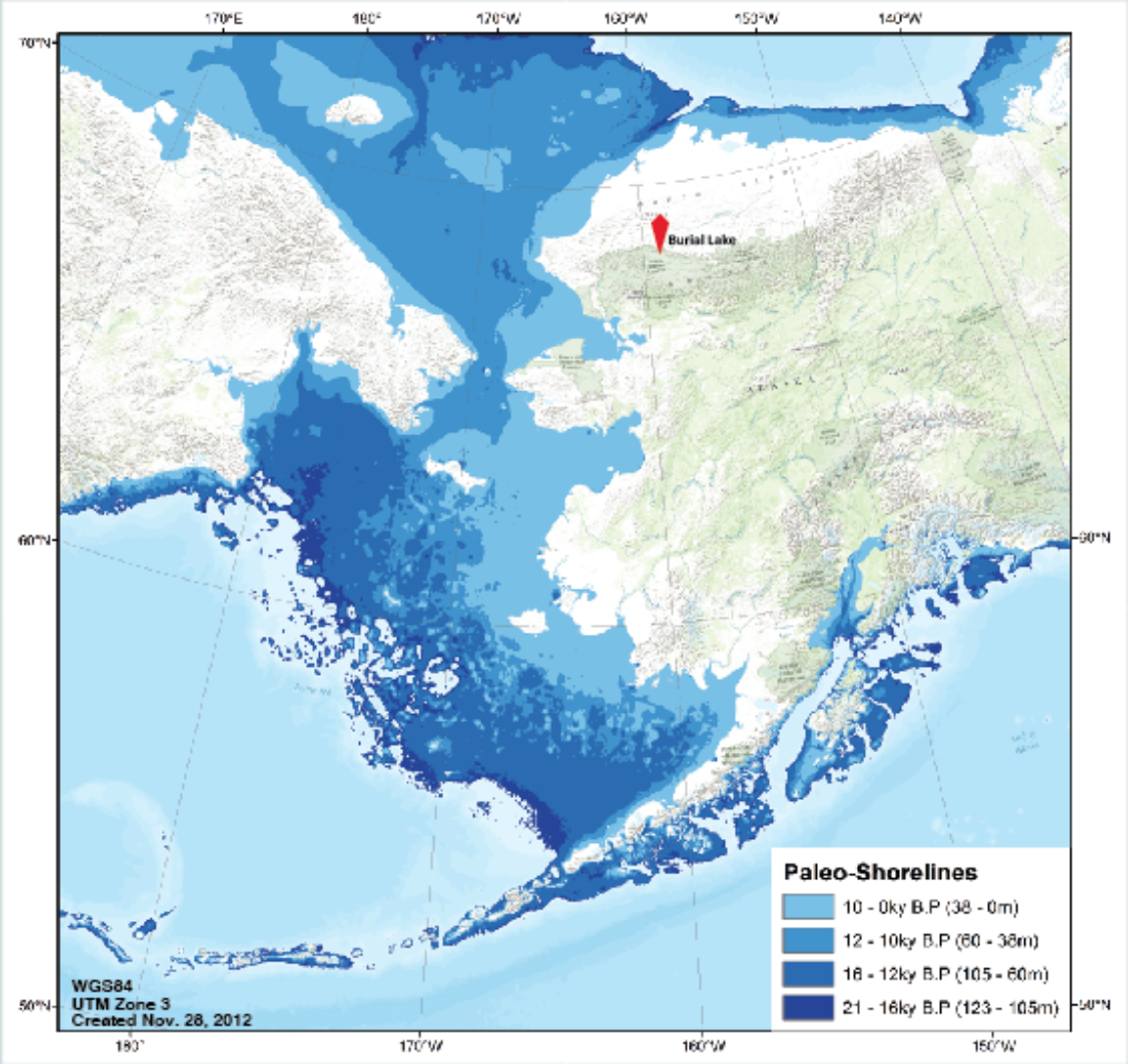

Figure 2.10 – Paleo-shoreline map of Beringia showing sea level rise and inundation of Beringian continental shelves from the LGM sea level low-stand (~21 ka) to present. Contours correspond to timing of major changes in S-Ratios at ~16, ~12, and ~10 ka (see Fig. 2.9).

Table 2.1 – AMS radiocarbon results based on terrestrial macrofossils identified in deep basin cores A10 and C10, which were stratigraphically correlated to produce the composite depth scale (see Appendix A). Radiocarbon ages were calibrated using Calib 6.0 (Stuiver et al., 2005) and the IntCal09 calibration curve (Reimer et al., 2009), and are reported at their 2σ confidence levels.

Sample ID (UCIAMS #)	Core-Drive	Drive Depth (cm)	Composite Depth (cm)	Material	Raw Age (^{14}C yr BP)	Error (yr)	Calib Age (yr BP)
89197	A10-D1	45.0	45.0	plant material	2,535	30	2,493 - 2,745
109361	A10-D1	66.5	66.5	wood	3,635	25	3,872 - 4,074
116878	A10-D1	87.5	87.5	plant material	4,910	90	5,470 - 5,896
89198	A10-D1	111.0	111.0	plant material	6,345	25	7,174 - 7,410
109362	A10-D1	141.5	141.5	wood	8,850	110	9,564 - 10,205
89199	A10-D2	84.0	166.0	plant material	9,760	40	11,134 - 11,244
89200	A10-D3	54.0	173.5	seed	10,085	45	11,398 - 11,959
89122	C10-D3	45.0	219.0	wood	13,670	30	16,657 - 16,978
* 109363	A10-D5	35.5	359.5	plant material	14,590	550	16,570 - 18,903
89201	A10-D7	29.0	553.0	seed	25,300	510	29,173 - 31,074
** 89123	C10-D7	64.0	598.0	plant material	31,290	300	35,085 - 36,475
89124	C10-D7	72.0	606.0	wood	31,090	210	35,036 - 36,313
89121	A10-D8	35.5	636.5	wood	32,150	240	35,699 - 37,342

* Sample excluded from age model due to very low carbon yield and presumed modern carbon contamination.

** Sample excluded from age model due to slight age reversal with sample #89124, containing slightly higher carbon yield.

Table 2.2 – Summary of IRM decomposition results for samples A-I assuming a two-component model. Relative percent contribution for components 1 and 2 are given for each sample along with their mean coercivities. R^2 values are also given for the sum of components 1 and 2 compared against smoothed input data. Graphical results for samples H, E, and A are shown in Figure 2.6, representing Subunits 1, 2, and 3, respectively. Note samples B and G appear anomalous, which can be attributed to measurement noise and/or better representation using a three-component model (see text for further explanation).

Sample (Depth)	% Component 1	% Component 2	Mean Coercivity Component 1 (mT)	Mean coercivity Component 2 (mT)	Sum of Components 1&2 R2 correlation to smoothed input data	
A (40 cm)	68.2	31.8	44.1	176.6	0.995	* Displayed above
B (80 cm)	43.4	56.6	38.0	105.6	0.972	* Noisy data
C (130 cm)	74.7	25.3	42.1	239.1	0.994	
D (170 cm)	89.3	10.7	43.5	303.7	0.998	
E (190 cm)	87.8	12.2	41.0	287.0	0.997	* Displayed above
F (241 cm)	94.1	5.9	42.0	339.2	0.996	
G (384 cm)	56.1	43.9	44.2	60.2	0.992	* Best fit by 3 comps.
H (474 cm)	93.0	7.0	47.7	314.6	0.995	* Displayed above
I (574 cm)	80.6	19.4	47.7	231.5	0.987	

Chapter 3

A 37,000-year Record of Paleomagnetic Secular Variation from Burial Lake, Arctic Alaska

J.M. Dorfman[1]*, J.S. Stoner[1], M.S. Finkenbinder[2], M.B Abbott[2], C. Xuan[1], G. St-Onge[3]

[1] Oregon State University, College of Earth, Ocean, and Atmospheric Sciences (CEOAS), Corvallis, Oregon, USA

[2] University of Pittsburgh, Department of Geology and Planetary Science, Pittsburgh, Pennsylvania, USA

[3] *Institut des Sciences de la Mer de Rimouski* (ISMER), Rimouski, Quebec, Canada

* Corresponding author e-mail: jdorfman@coas.oregonstate.edu

In preparation for submission to:

Geochemistry, Geophysics, Geosystems (G-Cubed)

3.1 Abstract

Burial Lake sediments from the Noatak Basin in the northwest Brooks Range of Arctic Alaska (68.43°N, 159.17°W, 21.5 m water depth) allow us to reconstruct millennial-scale variations in full-vector geomagnetic field behavior (directions and paleointensity). A radiocarbon-constrained chronology (11 AMS ^{14}C dates, extending back ~37,000 Cal. yr B.P) establishes the Burial Lake record as the longest continuous records paleomagnetic secular variation (PSV) from Arctic Alaska. This fills a significant data gap in the growing Holocene paleomagnetic database, while allowing us to extend our understanding of PSV beyond the Holocene and into the Pleistocene, and continue the development of regional stratigraphic dating curves. Progressive alternating field (AF) demagnetization of u-channel samples and additionally acquired physical and rock-magnetic datasets reveal three distinct lithologic sub-units associated with the last glacial period, the deglacial transition, and the Holocene. Despite this lithologic variability, we isolate a stable single-component characteristic remanent magnetization, carried predominately by low-coercivity (titano)magnetite in the pseudo single-domain (PSD) to multi-domain (MD) grain size range. Paleomagnetic data are consistent with other available regional PSV records and continuous spherical harmonic model outputs, with only small deviations from Geocentric Axial Dipole (GAD) predictions during the Holocene. Larger amplitude directional features are prevalent before 10 ka, and inclinations lay significantly shallower than GAD. While this may be related to lithology and the sediment magnetic acquisition process, comparisons with regional records (including data from lava flows) indicate similar Holocene-Pleistocene discrepancies. Following on the "eccentric dipole" hypothesis, subdued secular variation and GAD-like behavior in the Pacific (i.e., the "Pacific dipole window") appears confined to the Holocene high-intensity state, showing greater variability as Pleistocene field strength diminishes, and/or the dipole axis is shifted away from the Pacific hemisphere. Long period trends in PSV from the Alaskan Arctic are also similar in character to far-field sites (e.g., Hawaii and Siberia), suggesting large-scale coherent core-fluid flow regimes, expressed over surface geographical extents >5,000 km, and spanning Holocene-Pleistocene time intervals.

3.2 Introduction

The Earth's magnetic field, which is generated by fluid convection in the liquid outer core, can be measured as a vector sum, described by directional components, Inclination (I) and Declination (D), as well as total field Intensity (F). Past changes in the geomagnetic field vector, known as Paleomagnetic Secular Variation (PSV), occur on time-scales ranging from seconds to millions of years. Instrumental and historical observations of PSV are limited to the past ~400 years (Chulliat et al., 2010; Jackson et al., 2000), with geologic archives providing the only means of reconstructing earlier geomagnetic field variability. Lake and marine sediments are among the few such archives with the unique capability to provide continuous, high-resolution PSV records that can be well dated. A number of high-quality records have been published in the last few decades (e.g., Turner and Thompson, 1981; Snowball and Sandgren, 2002; Snowball et al., 2007; Lund and Banerjee, 1985; Verosub et al., 1986; Lund, 1996; Creer and Tucholka, 1982; Gogorza et al., 2000) and incorporated into continuous spherical harmonic models (CSHM; Korte and Constable, 2003; 2005; 2011; Korte et al., 2005; 2009; 2011), extending historical type assessments of the space/time structure of the geomagnetic field. At present, however, the spatial and temporal resolution of these models is limited by the present distribution and quality of PSV data, including independent chronological constraints (Stoner et al., 2013). Few records extend beyond the Holocene – lacustrine records in particular, as most lake basins postdate the last glacial period (Hayashida et al., 2007), and the Alaskan Arctic (and greater high-latitude Pacific) remains a significant data gap.

Due to their proximity to the North Magnetic Pole, high latitude sites have the potential to record higher amplitude directional changes (Cox, 1970), but unfortunately, the few studies that have been published from the region (Andrews and Jennings, 1990; Frank et al., 2002; Snowball and Sandgren, 2002; Geiss and Banerjee, 2003; Nowacyzk et al., 2001; Snowball and Sandgren, 2004; Snowball et al., 2007; Stoner et al., 2007; Barletta et al., 2008; 2010; Lisé-Pronovost et al., 2009) are again, confined to the Holocene time interval, with only a subset of these capturing the full paleomagnetic vector. Recognizing that synchronous changes in the geomagnetic field at a given site can provide regional chronostratigraphic horizons, recent studies have successfully used

the paleomagnetic vector as a regional stratigraphic dating tool (e.g., Lisé-Pronovost et al., 2009). Given the increased focus on Arctic paleo-environments, and upcoming Arctic expeditions with particular interest in glacial-interglacial time-scales (e.g., IODP Expedition 341), it is important that we extend our understanding of Arctic geomagnetic field behavior beyond the Holocene and continue the development of regional stratigraphic dating curves.

In this study, we present a continuous 37,000-year record of directional PSV, derived from sediment cores from Burial Lake, Arctic Alaska (Fig. 3.1), with relative paleointensity (RPI) constrained for the last ~14,700 years. Unlike many paleomagnetic and paleoclimate reconstructions in Arctic environments, which suffer from a lack of robust chronologies (e.g., Lisé-Pronovost et al., 2009; Hillaire-Marcel, 2008), sediment cores from Burial Lake can be well dated, and contain a precise radiocarbon chronology (Fig. 3.2) determined through accelerator mass spectrometry (AMS). This study fills an important spatial and temporal gap in the growing paleomagnetic database, allowing us to further reconstruct boreal field morphology and place detailed constraints on long-term (pre- and post-Holocene) geodynamo behavior. Lastly, the independently dated Burial Lake PSV record has the ability to serve as a baseline regional stratigraphic dating curve, applicable beyond the Holocene and through the last deglacial episode.

3.3 Regional Setting

Burial Lake (68.43°N, 159.17°W) lies at 460 m above sea level in the Northwest Brooks Range, Alaska (Fig. 3.1). It is a small (~0.8 km^2) roughly circular lake, with a maximum depth of 21.5 m. Perched above the surrounding tundra on a slight topographic high, the catchment is limited in size, defined by steep-sided embankments (3-5 m high) that extend along most of the lake's perimeter. The lake has no direct inflow and contains a small outlet stream on the southwest shoreline. Burial Lake is oligotrophic and a hydrologically open system. It is well mixed, with no evidence for thermal or chemical stratification (Abbott et al., 2010). Sedimentation is characterized by variable aeolian deposition, with additional inputs derived from seasonal runoff and biogenic accrual (Dorfman et al., *in prep*).

Flanked by the DeLong Mountains to the north, and the Baird Mountains to the south, Burial Lake lies within the northwestern limit of the Noatak Basin, a broad lowland depression with a maximum width of 80 km. During the mid and late Pleistocene, mountain glaciers repeatedly dammed the Noatak River, (which traverses the Basin to the south of Burial Lake) forming a series of large proglacial lakes with surface areas as large as 4400 km^2 (Hamilton, 2001) - collectively known as *Glacial Lake* Noatak (Hamilton and Van Etten, 1984). Glacial Lake Noatak appears not to have inundated Burial Lake since the Itkillik I (early Wisconsonian) glacial advance (Hamilton, 2010), and the lake remained ice-free during the Last Glacial Maximum (LGM: 26.5 – 19 ka; Clark et al., 2009), lying just beyond the reach of mountain glaciers and Northern Hemisphere ice-sheet extent (Hamilton, 2001).

In a geomagnetic context, Burial Lake is located just outside the surface expression of the "tangent cylinder," the area described by a latitudinal circle at ~ 69.5° North and South, and defined as the region of the outer core (where Earth's magnetic field is generated) that is created if the solid inner core is transcribed within a theoretical cylinder parallel to the axis of rotation. Convective flow patters within the tangent cylinder are thought to be distinct from those outside the region, and therefore could generate a distinctive geomagnetic field from that at mid-latitudes (Aurnou et al., 2003). Burial Lake is also situated between the historically-persistent North American and Siberian "flux lobes", areas of concentrated geomagnetic flux that appear to be important drivers of PSV at mid latitudes (Bloxham and Gubbins, 1985).

3.4 Methods

3.4.1 Field Methods

During the summer of 2010, three complete sediment cores ranging from 4.15 - 6.51 m in length were collected; two from the central deep basin (A10 and C10: 21.5 m water depth) and one nearer to the margin (D10: 8.5 m water depth) using a 2" diameter square-rod Livingstone coring system designed to take 1 m successive drives. A larger, 2 5/8" polycarbonate barrel was used to capture the undisturbed sediment-water interface at each location. Overlapping sections assured complete recovery in the upper part of each

record, but in order to achieve deeper core penetration, holes were cased with PVC pipe, which restricted the ability to overlap drives in the lower portions of the records.

3.4.2 Magnetic Methods

Whole cores were split, described, and subsampled using rigid plastic u-channels (2x2 cm cross sectional area) at the University of Pittsburgh. Half cores were measured for point source low-field magnetic susceptibility (k_{LF}) at 2 mm resolution using a Bartington™ MS2 meter and MS2E1 sensor, mounted to a TAMISCAN-TS1 automatic stage conveyor. Paleomagnetic and rock magnetic properties were studied through progressive Alternating Field (AF) demagnetization of u-channel samples measured at 1 cm intervals using a 2G Enterprises™ model 755-1.65UC cryogenic superconducting u-channel rock magnetometer and pulse magnetizer module (for isothermal remanent magnetization, IRM) at the Oregon State University *Paleo- and Environmental Magnetism Laboratory*. UPmag software (Xuan and Channell, 2009) provided an elegant suite of data processing, optimization, and visualization capabilities, allowing us to more-robustly assess our u-channel results.

The natural remanent magnetization (NRM) was studied using a 16 to 24-step AF demagnetization routine with 2.5, 5, or 10 mT spacing between steps. Anhysteretic remanent magnetization (ARM) was induced at a peak AF of 100 mT with a 0.05 mT direct current (DC) biasing field. An initial IRM was imparted with a DC field of 0.3 T, and a second IRM (corresponding to a Saturation Isothermal Remanent Magnetization, SIRM) was imparted with a higher DC field of 1.0 T. These laboratory-applied magnetizations were subsequently measured and demagnetized using an AF routine comparable to that of the NRM. The pick-up coils of the magnetometer integrate measurements over a half-peak width of ~7 cm. To eliminate edge effects associated with this response function, we mask the first and last few centimeters of data from each u-channel segment.

Demagnetization ratios of $NRM_{30\ mT}/NRM_{0\ mT}$, $ARM_{30\ mT}/ARM_{0\ mT}$, and $IRM_{30\ mT}/IRM_{0\ mT}$ provide information on the mean coercivity state of the sample, which is a reflection of magnetic grain size and mineralogy (Stoner and St. Onge, 2007). Higher values indicate higher coercivity, interpreted as finer grain size if the sample is of

uniform ferrimagnetic magnetic mineralogy (Stoner and St. Onge, 2007). $ARM_{0\ mT}/SIRM_{0\ mT}$ is widely employed as a magnetic grain size indicator for magnetite, with finer grain sizes yielding larger values (Evans and Heller, 2003). The parameter derived by normalizing the IRM at 0.3 T by the SIRM at 1.0 T, sometimes referred to as a pseudo S-Ratio (St-Onge et al., 2003) is analogous to the S-ratio of Stober and Thompson (1979), and can be used to estimate the proportion of high vs. low-coercivity magnetic mineralogies (e.g., the proportion of magnetite to hematite). Values closer to 1 denote low-coercivity ferrimagnetic minerals, such as magnetite, while lower values signify the presence of higher-coercivity components, such as hematite (Thompson and Oldfield, 1986; King and Channel, 1991; Stoner and St. Onge, 2007).

IRM acquisition experiments were performed on subsampled bulk sediments from nine down-core locations (Fig. 3.3) using a Princeton Measurements Corporation™ MicroMag model 3900 vibrating sample magnetometer (VSM) at Western Washington University. Data were smoothed using a MATLAB™ loess filter, and IRM decomposition was performed using IRMUNMIX V2.2 (Heslop et al., 2002). This software package automates the fitting of IRM acquisition curves through the use of an expectation maximization algorithm to decompose curves into their individual component contributions, thereby facilitating the distinction of magnetic mineral assemblages within the bulk sample. Results for all nine samples are given in Dorfman et al. (*in prep*), but here we provide only representative results.

Hysteresis experiments on subsampled bulk material were carried out at the *Institute des Sciences de la Mer de Rimouski* (ISMER), in Quebec, Canada, on a Princeton Measurements Corporation™ MicroMag model 2900 alternating gradient force magnetometer (AGM), to assess both mineralogy and magnetic grain size. Hysteresis loops were corrected for paramagnetic/diamagnetic contributions, and the following values were derived: the coercivity of magnetic minerals (Hc), the coercivity of remanence (Hcr), the saturation magnetization (Ms), and the saturation remanence (Mrs).

Thermomagnetic analyses were attempted on four bulk samples to study the temperature dependence of k_{LF}, using an MS2WF Bartington™ instrument. Measurements were heated at 2°C steps from room temperature (24°C) up to 700°C, and subsequently cooled to room temperature. Unfortunately, given the low k_{LF} of Burial

Lake sediments and the sample size limitations of the instrument, results proved unreliable, and data are not presented.

3.4.3 Physical Analysis

At ISMER, u-channels were photographed using a high-resolution digital camera mounted on a GEOTEK™ Multi Sensor Core Logger. Computerized Tomography (CT) scans were performed at the *Institute national de la recherché scientifique, Centre Eau Terre Environement* (INRS-ETE) in Quebec City, Canada, in order to visualize sedimentary structures, assess possible core deformation, and aid stratigraphic matching efforts. The CT numbers were extracted using a MATLAB™ code developed by Jacques Labrie, at ISMER, and primarily reflect changes in bulk density (St. Onge et al., 2007).

3.4.4 A10/C10 Composite Depth Scale

Detailed core descriptions and down-core physical, geochemical, and magnetic measurements were utilized to stratigraphically correlate deep basin cores, A10 and C10 (which were taken only meters apart), and place them on a common depth scale (see Appendix A). Stratigraphic correlation between deep basin cores and the margin core (D10) proved difficult due to an absence of material in D10 suitable for radiocarbon dating, and a likely depositional hiatus, observed in D10 and previously observed at a similar shallow margin location in the lake (Abbott et al., 2010). Our current inability to provide a robust absolute or tuned chronology for D10 has led us to omit D10 paleomagnetic results. Given the quality, continuity, and extent of the A10 dataset (and in many intervals, lack of comparable C10 data), paleomagnetic results in this study are derived exclusively from the 6.51 m-long A10 core. The A10/C10 composite depth (referred to throughout as "depth") is utilized solely for the production of the age-depth model (Fig. 3.2), in which radiocarbon-dated samples were derived from both A10 and C10 cores (Table 3.1). Though data are not provided, paleomagnetic results from the C10 core are in overall agreement with the A10 record, and are used here, in some instances, to validate PSV features observed in A10. We are currently in the process of constructing an A10/C10 composite record of Burial Lake PSV that will be incorporated in the final journal publication of this manuscript.

3.5 Age-Model

AMS radiocarbon measurements were performed on 13 terrestrial macrofossil samples from cores A10 and C10 at the *Keck-Carbon Cycle AMS Facility* at the University of California, Irvine (Table 3.1). Size-dependent sample preparation backgrounds were subtracted based on measurements of ^{14}C-free wood. All results have been corrected for isotopic fractionation according to the conventions of Stuiver and Polach (1977), with $\delta^{13}C$ values measured on prepared graphite. Radiocarbon ages were calibrated using Calib 6.0 (Stuiver et al., 2005), and the IntCal09 calibration curve (Reimer et al., 2009), assuming a ΔR of 0. Calibrated ages are reported at their 2σ confidence level.

Two out of the original 13 dates (UCIAMS #109363 and #89123; Table 3.1) were excluded prior to generating the age-depth model (red triangles in Fig. 3.2). The first appears anomalously young – likely contaminated by modern carbon during the combustion and graphitization of this small (0.017 mgC) sample (Oswald et al., 2005), which approaches the threshold limit for AMS radiocarbon analysis. Inclusion of this date would also invoke a sudden and drastic increase in sedimentation rates (reaching 1.51 m/ka), which is unsupported by additional radiocarbon constraints or lithologic evidence, and would be hard to explain given the local geography. Therefore, at present, we are uncomfortable with assigning such weight to a single questionable measurement. The second displays a slight age-reversal with an adjacent date (#89124; Table 3.1), though overlapping error bars suggest both are statistically sound age-control points. We exclude date #89123 based on its slightly broader uncertainty and lower carbon yield.

CLAM software for "classical," non-Bayesian age-depth modeling (Blaauw, 2010) was used to produce the "best fit" linearly interpolated depth to radiocarbon age model (Fig. 3.2) used throughout this report. To account for chronologic uncertainty, we apply a Monte Carlo-based approach that perturbs the interpolated age-depth model 10,000 times following a random draw from a normal distribution between the 2σ calibrated ^{14}C ages (Marcott et al., 2013). The uncertainty between the age control points (Fig. 3.2) is modeled as a random walk, after Huybers and Wunch (2004), with chronologic uncertainty assumed to be auto-correlated through time and modeled as a first order autoregressive (AR1) process.

3.6 Results

3.6.1 Lithostratigraphy

Radiocarbon results support stratigraphic evidence for a continuous sedimentary record spanning the last ~37,000 years. An extensive physical, geochemical, and environmental magnetic investigation of Burial Lake sedimentology is provided by Dorfman et al. (*in prep*), in which the Burial Lake record is subdivided into three distinct lithologic subunits, with the timing of lithologic transitions consistent with Northern Hemisphere deglacial climate change (Clark et al., 2009; 2012). In the following section we summarize these results, focusing on the lithologic variations that are necessary for interpreting the paleomagnetic record. Down-core physical and magnetic results are provided in Figure 3.3, partitioned according to the previously defined subunit boundaries:

Lithologic Subunit 1 (651 – 285 cm)

Subunit 1 extends from the base of the core (651 cm) to 285 cm (Fig. 3.3), and corresponds to the last glacial period (37.2 – 19.4 ka). Sediments are composed mainly of fine-grained lithogenic detritus with high CT density (Fig. 3.3; 324 ± 62.9 HU). Faint banding is observed in CT images (Fig. 3.3) throughout the record suggesting minimal bioturbation. k_{LF} (Fig. 3.3) is relatively high and variable ($1.3 \times 10^{-5} \pm 0.3 \times 10^{-5}$) along with other concentration dependent magnetic parameters, ARM ($7.4 \times 10^{-3} \pm 2.9 \times 10^{-3}$ A/m), IRM (0.62 ± 0.25 A/m), and SIRM (0.66 ± 0.26 A/m), indicating relatively high concentrations of ferrimagnetic material (Fig. 3.3). Several discrete k_{LF} peaks are observed at 582, 294, and 210 cm (Fig. 3.3). These are reflected in other magnetic parameters, and are perhaps related to crypto-tephra deposits. Ratios of $ARM_{30\ mT}/ARM_{0\ mT}$ and $IRM_{30\ mT}/IRM_{0\ mT}$ (Fig. 3.3; 0.49 ± 0.03 and 0.34 ± 0.04, respectively) suggest that low-coercivity magnetic minerals carry much of the magnetization, which is also reflected by high S-Ratios (Fig. 3.3; 0.93 ± 0.02) and steep IRM acquisition of representative Sample H in Figure 3.4. S-Ratios slightly decrease below 550 cm (reaching ~0.86 at the base of the core), suggesting an increased proportion of high-coercivity minerals. IRM decomposition results (Fig. 3.5) model Burial Lake sediments as as a competing sum of both low-coercivity and high-coercivity components, thought to

reflect local versus far-field sources. While Sample H does show a small (7%) contribution from high-coercivity minerals (Fig. 3.5), the sample is composed overwhelmingly (93%) of low-coercivity material, with a mean coercivity (47.7 mT), similar to that of (titano)magnetite. While uncorrected hysteresis loops (dashed lines, Fig. 3.6) show substantial high-field slopes diagnostic of significant paramagnetic contributions, shapes of corrected loops (solid lines, Fig. 3.6) confirm the presence of ferrimagnetic minerals, with Mrs/Ms values mostly ranging between 0.1 and 0.3, and saturation fields mostly below 0.2 T (Day et al., 1977; Tauxe, 1993). Ratios of Mrs/Ms and Hcr/Hc are plotted in Figure 3.6 according to Day et al. (1977). Samples from Subunit 1 fall within the pseudo single-domain (PSD) to multi-domain (MD) theoretical grain size boundaries, and are therefore suitable for paleomagnetic studies (Stoner and St. Onge 2007).

Lithologic Subunit 2 (285 – 140 cm)

Subunit 2 corresponds to the deglacial transition (19.4 – 9.8 ka), and is characterized by a broad lithologic transition extending between 285 and 140 cm (Fig. 3.3). A marked decline in CT density is observed along with decreasing values of k_{LF} ($0.83 \times 10^{-5} \pm 0.52 \times 10^{-5}$), ARM ($5.5 \times 10^{-3} \pm 7.3 \times 10^{-3}$ A/m), IRM (0.37 ± 0.37 A/m), and SIRM (0.40 ± 0.39 A/m). Dorfman et al. (*in prep*) demonstrate that the lowered density and significant decline in ferrimagnetic concentration (Fig. 3.3) are partly attributed to organic/biogenic dilution of ferrimagnetic input as well as a significant reduction in clastic aeolian flux. S-Ratios (Fig. 3.3), which vary irrespective of organic/biogenic dilution, sharply decline to ~0.83 between 212 and 182 cm, demonstrating an apparent increase in the proportion of high-coercivity minerals. IRM acquisition curves generated from sample E (Fig. 3.4) and subsequent decomposition (Fig. 3.5) demonstrate that the decline in S-Ratios is driven by a reduction in the low-coercivity component relative to a background influx of high-coercivity material. Despite this reduction, sample E is still dominated (87.8%) by the low-coercivity component, suggesting the potential to record stable remanence. $ARM_{30\ mT}/ARM_{0\ mT}$ and $IRM_{30\ mT}/IRM_{0\ mT}$ (0.47 ± 0.04 and 0.30 ± 0.05, respectively; Fig. 3.3) increase through Subunit 2, indicating a fining in magnetic grain size, which is upheld by increasing values

of $ARM_{0\ mT}/SIRM_{0\ mT}$ (0.015 ± 0.005 compared with 0.012 ± .0032 in Subunit 1; Fig. 3.3). Hysteresis results (Fig. 3.6) do not show much discernable difference in magnetic grainsize, but still plot within PSD-MD grain size boundaries. Given the changes in magnetic mineralogy through this interval, we use caution when interpreting magnetic grain size proxies, originally defined based on the magnetic response of pure magnetite.

Lithologic Subunit 3 (140 – 0 cm)

Subunit 3 extends from 140 cm to the top of the core at 0 cm (Fig. 3.3) and represents the time period, 9.8 ka to present. Sediments are composed mainly of fine-grained organic silts (gyttja) with low CT density (-47.1 ± 62.8 HU) and low k_{LF} (0.26 x 10^{-5} ± 0.07 x 10^{-5}; Fig. 3.3), typical of Holocene sediments from northern Alaska (e.g., Eisner and Colinvaux, 1992). Sediments in Subunit 3 appear more homogeneous, with k_{LF}, ARM (1.1 x 10^{-3} ± 0.1 x 10^{-3} A/m), IRM (0.03 ± 0.004 A/m), and SIRM (0.04 ± 0.004 A/m) displaying much more subdued variability compared with the larger amplitude intensity variations below (Fig. 3.3). S-Ratios (Fig. 3.3) continue to decline, reaching values as low as ~0.78. IRM acquisition of sample A (Fig. 3.4) demonstrates the higher coercivity behavior of Subunit 3 sediments, and decomposition results (Fig. 3.5) reveal the overall diminished relative contribution of the low-coercivity component by ~25% from Subunit 1. Although sediments in Subunit 3 clearly reveal a high-coercivity magnetization, sample A still remains dominated (68.2%) by low-coercivity minerals with a mean coercivity of (44.1 mT), suggesting the magnetization is carried predominantly by low-coercivity titano(magnetite). Ratios of $ARM_{30\ mT}/ARM_{0\ mT}$ and $IRM_{30\ mT}/IRM_{0\ mT}$ (Fig. 3.3) continue to increase (0.55 ± 0.02 and 0.53 ± 0.04, respectively), along with $ARM_{0\ mT}/SIRM_{0\ mT}$ (Fig. 3.3; 0.28 ± 0.001), consistent with fining magnetic grain sizes. Hysteresis loops (Fig. 3.6) are still characteristic of ferrimagnetic minerals, displaying reduced paramagnetic contributions comparative to samples in Subunit 1. Noisy loops reflect low ferrimagnetic concentrations in Subunit 3, which approach instrumentation limitations and result in somewhat scattered hysteresis results (Fig. 3.6).

3.6.2 Natural Remanent Magnetization

Before directional data can be used for paleomagnetic studies, we must first demonstrate that they accurately represent variations in Earth's magnetic field. Rock magnetic results have thus far demonstrated that despite suboptimal high-coercivity magnetization in Subunit 3, sediments are dominated by a low-coercivity mineral assemblage consistent with PSD-MD (titano)magnetite. In the following sections we continue to address the reliability criteria of Thompson, (1984), Opdyke and Channell, (1996), Stoner and St. Onge, (2007) to test the integrity of Burial Lake sediments as accurate recorders of the geomagnetic field.

Burial Lake sediments carry a weak, but well-defined and relatively stable NRM, shown in Figure 3.7, alongside peak AF demagnetization steps between 10 and 80 mT. Stepwise demagnetization results and vector endpoint diagrams (Zijderveld plots) for representative samples in each lithologic subunit are also provided in Figure 3.7, depicting the demagnetization behavior of the NRM. $NRM_{0\ mT}$ intensities mimic magnetic susceptibility trends, remaining high and variable ($2.4 \times 10^{-3} \pm 1.8 \times 10^{-3}$ A/m) throughout Subunit 1, and decreasing to around $2.2 \times 10^{-4} \pm 0.4 \times 10^{-4}$ A/m in Subunit 3 as the concentration of ferrimagnetic input dwindles. Zijderveld plots show that in most cases, a weak viscous component is removed by the 10 mT demagnetization step. Ratios of $NRM_{30\ mT}/NRM_{0\ mT}$ (Fig. 3.7) average 0.48 ± 0.07 in Subunit 1, demonstrating that nearly half of the NRM is acquired by minerals within the 0-30 mT coercivity range. This ratio increases to 0.56 ± 0.04 in Subunit 3, consistent with finer magnetic grain sizes and/or higher coercivities. Following the 80 mT demagnetization step, only 10.8% ± 3.2% of the $NRM_{0\ mT}$ remains for sediments in Subunit 1. Subunit 3 displays a much higher percentage of remaining remanence (25.9% ± 5.6%), further indicating the high-coercivity nature of these sediments.

3.6.3 Paleomagnetic Directional Results

As a first approach, component Inclination and Declination were calculated using standard Principal Component Analysis (PCA) to define a Characteristic Remanent Magnetization (ChRM) from consecutive peak AF demagnetization steps between 10 and 65 mT (12 or 18 steps total, depending on the u-channel). Resulting component

directions from this "consecutive-range" approach are plotted in Figure 3.7 (solid orange lines), along with their Maximum Angular Deviation (MAD) values. MAD values are a measure of the complexity of the ChRM, and are often used to assess the quality of a paleomagnetic record (Kirschvink, 1980). This calculation was repeated using a ChRM isolated between peak AF demagnetization steps of 10 and 50 mT (9 or 15 steps total), however this time, "optimized" PCA results (Fig. 3.7, dashed blue lines) were computed by selecting the best 7 out of 9, or 12 out of 15, demagnetization steps that provided the lowest MAD value. By confining the ChRM to between 10 and 50 mT, we restrict our analysis to the more reliable low-coercivity range, while avoiding possible contamination from high-coercivity components. Furthermore, the optimized approach allows us to disregard the occasional spurious demagnetization data that result from our weakly magnetic samples. Figure 3.7 demonstrates that the optimized approach significantly reduces MAD values, while having little effect on component directions. This speaks to the quality of Burial Lake directional data and validates the continued use of optimization methods.

Optimized MAD values (Fig. 3.7) average 2.5° ± 1.3° through Subunit 1 and increase to 5.6° ± 2.2° as the NRM intensity diminishes in Subunit 3. While sediments in Subunit 3 clearly do not display ideal demagnetization behavior, MAD values for the most part lie well below the proposed threshold of 15° sought for reliable paleomagnetic studies (Butler, 1992; Opdyke and Channell, 1996), though more recent reviews concerning Quaternary PSV and RPI studies call for MAD values ≤ 5° (Stoner and St. Onge, 2007). The high MAD values in this case may result from low ferrimagnetic concentration (i.e., low signal to noise), rather than complex magnetic acquisition with different components "locked-in" over a range of coercivities. This said, high MAD values and aberrant component directions between 25 and 0 cm (shaded grey in Fig. 3.7) could reflect soft sediment core-top deformation during the sampling process, and these data are disregarded. The interval between 194 and 170 cm also displays high MAD values that correspond to abrupt shallow inclination features and easterly declinations (also shaded grey in Fig. 3.7). Although we do not omit these results, we suggest they be treated with caution.

Component Inclinations vary around the GAD prediction for site latitude (78.8°;

Fig. 3.7) for the upper portion of the record, with a mean inclination of 77.2° for Subunit 3. Although somewhat counterintuitive, inclinations for Subunits 1 and 2 are on average, 7.4° shallower than GAD despite lower $NRM_{30\ mT}/NRM_{0\ mT}$ ratios, higher NRM intensities, lower MAD values, higher S-Ratios, and overall, seemingly higher quality paleomagnetic data (Fig 3.3 – 3.7).

Individual drives collected during the coring process lacked azimuthal orientation. Therefore, component declinations (Fig. 3.7) are relative, with each drive rotated to a mean of 0°. Declinations were aligned in overlapping drives where possible. Although not evident in the CT imagery (Fig. 3.3), one individual drive (A10-D6: 424-524 cm) appears to have twisted during the coring process, producing an easterly trend in declination for that section of the record, which spans an unreasonable 150° and is inconsistent with adjoining drives. This artifact was easily corrected by applying a linear regression to de-trend the data. The resulting declination (Fig. 3.7) matches up well with the adjoining drives, and is reproduced by the equivalent interval in the C10 core.

3.6.4 Normalized Remanence / Relative Paleointensity

The NRM acquired by sediments is both sensitive to changes in geomagnetic intensity, as well as lithologic variations associated with changes in the environment of deposition over time. In order to estimate relative changes in paleointensity (RPI) the NRM must be normalized by a magnetic parameter that fully accounts for this lithologic variation. Because we do not fully understand how sediments acquire a magnetization, and as a result, how past intensity is preserved (Roberts et al., 2013), strict criteria have been established for sediments likely to provide reliable RPI results (King et al., 1983; Tauxe, 1993; Stoner and St. Onge, 2007):

1. NRM demagnetization produces a strong, stable, and well-defined single component ChRM.
2. MAD values are generally ≤ 5° and ChRM inclinations vary around GAD.
3. Sediments must accurately record directional changes in geomagnetic field morphology.
4. The dominant remanence-bearing mineral is magnetite in the 1-15 μm PSD grain size range.
5. Changes in magnetic concentration do not vary by more than a factor of 10.

6. Normalized intensity records are not coherent with the bulk rock magnetic parameters, and therefore not controlled by lithologic variation.
7. Normalization of NRM intensities for magnetic concentration variations should be accomplished using several methods (i.e., different normalizers), all yielding similar results.

At first glance, Burial Lake sediments do not appear to completely satisfy all of these criteria. However, we have reason to believe that RPI can be accurately determined for the at least the top 200 cm of the record. Through a comparison with other regional paleomagnetic records from the Alaskan Arctic, North America, and the greater high-latitude Pacific, we will demonstrate that this interval accurately records geomagnetic directional PSV. This interval also possesses rather uniform magnetic concentration (Fig. 3.3) such that lithologic variability in the NRM can be accurately normalized by a suitable concentration dependent magnetic parameter.

Figure 3.8 shows normalized remanence results for the full length of the Burial Lake record, having used two different normalizing parameters (ARM and IRM). RPI was estimated using the slope method (Xuan and Channel, 2009), which uses the slope of the NRM versus its normalizer over a range of AF demagnetization steps. Similar to the directional PCA, this is achieved using a "consecutive-range" approach between consecutive peak AF demagnetization steps of 10 and 65 mT (solid orange lines), as well as an "optimized" approach confined to the 10-50 mT range (dashed blue lines). The optimized approach in this case seeks to maximize the correlation coefficient (R-value), which is calculated from the slope method and can be used to assess the quality of the RPI dataset (Fig 3.8). In most intervals, optimization increases the R-values while having little effect on RPI estimated from either normalizer (Fig. 3.8), and we again proceed with using optimized results. R-values in the top 200 cm are nearly identical (0.995 ± 0.004) for NRM/ARM and NRM/IRM suggesting a close resemblance of the optimized NRM, ARM, and IRM coercivity spectra. R-values in the lower portion of the record are slightly higher for NRM/ARM (0.998 ± 0.003), and roughly equivalent for NRM/IRM (0.995 ± 0.005). Similar to MAD values (Fig. 3.7), lower R-values in the top 200 cm, in this case, may result from low ferrimagnetic concentration.

Short-term (sub-meter) variability between NRM/ARM and NRM/IRM appears nearly identical (Fig. 3.8), the amplitude of features being the main discernable

difference. However, over the long term (i.e., the whole record), we observe that using ARM produces the lowest overall intensities in the upper 200 cm of the record, whereas using IRM produces the highest intensities (Fig. 3.8). In certain intervals, both normalized intensity records show clear resemblance to demagnetization steps from each of the normalizers ($ARM_{30\ mT}$ and $IRM_{30\ mT}$, Fig. 3.8), suggesting that lithologic variation has not been adequately removed from all parts of the record. Subunit 2 still resembles its characteristic large-scale change in magnetic concentration, as do many of the large amplitude normalized intensity features in Subunits 1 and 2. In contrast, the top 200 cm of the record does not.

Excluding intervals effected by core top disturbance or rapidly changing magnetic concentration (304-288 cm, 226-187 cm, and 25-0 cm; shaded pink in Fig. 3.8), we utilize bi-plots of $ARM_{30\ mT}$ vs. NRM/ARM and $IRM_{30\ mT}$ vs. NRM/IRM (Fig. 3.8) to identify those parts of the record that show strong correlation (and are therefore contaminated), and those that show little correlation (and may therefore still be reliable for RPI estimates). Using ARM as a normalizer, we observe only a very slight negative correlation ($R^2 = 0.14$) for the upper 200 cm, while the lower portion of the record demonstrates a relatively strong positive correlation ($R^2 = 0.42$). Using IRM as a normalizer produces a relatively strong (but negative) correlation in the upper 200 cm ($R^2 = 0.51$). Using IRM in the lower portion of the record produces two distinct populations of data with differing degrees of correlation. These two populations result from magnetic mineralogical differences emphasized by S-Ratios in Figure 3.3. Sediments dominated by low-coercivity magnetization (higher S-Ratios) form one population, having a strong positive correlation ($R^2 = 0.50$), while sediments below 550 cm (shaded green in Fig. 3.8), with a larger proportion of high coercivity minerals (lower S-ratios) form the second population, displaying a much lower, but still positive correlation ($R^2 = 0.18$). From these results we determine that only the more uniform upper 200 cm of the Burial Lake record may be suitable for continuous RPI reconstruction, and that ARM is the most appropriate normalizer. Although NRM/ARM and NRM/IRM display similar patterns of variability and R-values, choosing ARM allows us to further restrict the normalization to the more reliable low-coercivity range, while avoiding high-coercivity components that are likely to be acquired by the IRM. Large amplitude intensity variations within the

lower portion of the record hinder adequate normalization of rock magnetic variability. Though this interval likely contains short segments that meet the above stated criteria, we choose to focus on the continuous upper 200 cm for RPI from here forward.

3.7 Discussion

We have thus far demonstrated that Burial Lake sediments meet various internal paleomagnetic criteria, and should accurately record geomagnetic field variations. Mean sedimentation rates of ~20 cm/ky (Fig. 3.2) combined with the smoothing response of magnetometer should allow us to resolve geomagnetic features ~350 years or longer in duration. As a further test of the reliability of the Burial Lake PSV record, we now compare it with other PSV records from the region (Fig. 3.1). As Burial Lake provides the longest records of PSV to date in the Alaskan Arctic (as well as the Arctic and North America in general), few data exist for regional comparison beyond 10 ky B.P. We therefore split the directional record into two parts, first assessing the regional character of the field in the recent Holocene (0-10 ky), and later extending the comparison over the full length of the record using additionally available data. As continuously reliable RPI can only be obtained for the last ~14.7 ky in Burial Lake, the full extent of the record is included in the following discussion of Holocene PSV.

3.7.1 Holocene Paleomagnetic Secular Variation in the Alaskan Arctic

In Figure 3.9, we provide a full vector regional comparison, supported by Holocene PSV records from the Beaufort (core 803; Barletta et al., 2008) and Chukchi (cores 8 JPC and 6 JPC; Lisé-Pronovost et al., 2009) Seas on the Arctic Alaskan margin, as well as additional high latitude PSV records from the Gulf of Alaska (core 85 JC; Davies et al., *in prep*) and Grandfather Lake (GFL; Geiss and Banerjee, 2003) on the southwestern mainland. We also incorporate a well-known CHSM, *CALS10k.1b* (Korte et al., 2011), explicitly output for Burial Lake's location. This comparison is also supported by the more extensively studied Holocene records from North America (Fig. 3.10), which include lacustrine PSV records from Fish Lake, Oregon (Verosub et al., 1986), Lake Pepin (Brachfeld and Banerjee, 2000) and Lake St. Croix (Lund and Banerjee, 1985), Minnesota, the eastern Canadian stack compiled from marine cores in

the Laurentian Channel (Barletta et al., 2010), and the PSV record from ^{14}C-dated lava flows in western North America (PSVL; Hagstrum and Champion, 2002).

Comparisons between Burial Lake Holocene PSV and other records from the Alaskan Arctic (Fig 3.9) show regional consistencies in geomagnetic field variability at the millennial and even centennial timescales. Although amplitude of PSV in the Burial Lake record is comparatively subdued, we identify numerous correlative features in inclination (e.g., I-1 – I-8), declination (e.g., D-1 – D-8), and RPI (e.g., R-1 – R-3) (Fig. 3.9). Comparison with model results from CALS10k.1b (Fig. 3.9) also captures many of these millennial-scale directional and intensity variations, supporting their geomagnetic attribution.

To facilitate comparison, inclination anomalies are calculated by subtracting the GAD prediction for each site from the observed inclination value (Fig. 3.9). Features I-1, I-4, and I-6 mark abrupt steepening events that occur around 2.27, 4.85, and 7.75 ka, respectively in the Burial Lake record. Features I-2 and I-5 mark shallow inclination events, centered at 2.83 and 7.0 ka. Similar features are also observed in North American Holocene PSV records at around the same time (Fig. 3.10), extending the concept of Lund (1996) to suggest a spatially coherent geomagnetic field between the Alaskan Arctic and continental North America.

Declination records are less coherent between sites in the Alaskan Arctic (Fig. 3.9), and amplitude of features is more variable. Abrupt westward swings in declination, D3 and D6, occur around 3.55 and 7.28 ka, respectively in the Burial Lake record. Features D4 and D7 are examples of large eastwardly declination swings that occur around 4.85 and 8.07 ka. Unduly large amplitude declination features (on the order of hundreds of degrees) are observed in cores 8 JPC and 6 JPC (Lisé-Pronovost et al., 2009), and 803 (Barletta et al., 2008). These are not reflected in Burial Lake, 85 JC (Davies et al., *in prep*), nor any of the North American records (Fig. 3.10), and along with their seemingly anomalous eastward trends in declination between ~5.0 and ~2.0 ka, suggest potential coring-related artifacts.

Though paleointensity records for the Alaskan Arctic are in general agreement (Fig. 3.9), the Burial Lake record matches CALS10k.1b predictions (Fig. 3.9) and North American RPI records (Fig. 3.10) much more closely. The lowest intensities are

observed below the deglacial transition / Holocene boundary (i.e., the end of the Pleistocene epoch) between ~14.7 and ~12 ka for the Burial Lake record. Feature R-3 is part of a broad intensity high in the early Holocene centered between ~12.0 and ~8.5 ka. Intensity generally increases through the mid-Holocene from ~8.5 ka, with feature R-1 corresponding to a strong late Holocene peak in intensity at ~2.0 ka.

Discrepancies in the timing of individual PSV features are in large part due to the poorly constrained chronologies of many of the regional records (readily available radiocarbon chronologies are plotted for each record in Figures 3.9 and 3.10). With Burial Lake, however, we can take advantage of a well-constrained, precisely dated Holocene interval with seven radiocarbon dates spaced relatively evenly (mean age span of 1.67 ky between dates) between ~11.7 ka and the present (Fig. 3.9) to better estimate the timing of particular geomagnetic events. Certainly, small-scale geomagnetic differences occur between sites, and/or drift of particular features may result in a non-unique chronostratigraphic understanding of the broader region. Similarly, phase offsets as well as amplitude variability may result from post-depositional "lock-in" related processes, whereby sediments acquire their magnetization at depth, resulting in an age offset between the sediments and the magnetization, as well as potential signal smoothing (Strano et al., *in prep*). We therefore recognize that the age of the sediment as suggested by AMS radiocarbon results is not necessarily the age of the magnetization, and that lock-in likely generates features with older apparent ages. Comparison with the well-dated PSVL record from western North American (Fig. 3.10; Hagstrum and Champion, 2002), which is unaffected by lock-in, shows that Burial Lake features I-1, I-2, and D-2, are older by ~200 years, consistent with post-depositional lock-in (Verosub, 1977). Given the relatively low sedimentation rate environment (Fig. 3.2), we suggest that the Burial Lake record places, in effect, a "maximum age" estimate on geomagnetic features in the Alaskan Arctic.

3.7.2 Paleomagnetic Secular Variation from the Greater High-latitude Pacific over the last 40 ka

Having established the fidelity of Burial Lake sediments as accurate recorders of the geomagnetic field in the Holocene, we believe it likely that they maintain this ability

beyond 10 ka, where directional paleomagnetic data are much improved, containing higher ferrimagnetic concentrations, lower MAD values, higher S-Ratios, and lower ratios of $NRM_{30\ mT}/NRM_{0\ mT}$ (Fig. 3.3 – 3.7). In Figure 3.11, we extend our regional comparison to 40 ka, assessing the full extent of directional PSV over the greater high-latitude Pacific. This comparison is supported by the extended portions of 85 JC (Davies et al., *in prep*) and Grandfather Lake (GFL; Geiss and Banerjee, 2003), as well as data from the Oregon margin (core 17 PC; Xuan et al., *in prep*), Lake Baikal (Peck et al., 1996) in south central Siberia, Lake Waiau, (Peng and King, 1992) in Hawaii, and the Hawaiian lava record drilled from the Kilauea volcano (core SOH-4; Laj et al., 2002). These are among the few longer records of PSV in the vicinity of Burial Lake (Fig. 3.1), exemplifying the need for future paleomagnetic studies in the region.

Greater chronologic uncertainty in the glacial interval of many of these records (including Burial Lake; Fig. 3.11) makes the correlation of many small-scale features difficult, and given the rather large geographic distances between sites (Fig. 3.1), we hesitate to suggest that synchronous changes in geomagnetic field behavior would be expected to occur. However, we do observe large-scale correlative features in directional PSV across the broader high-latitude Pacific (e.g., I-9 – I-12; Fig. 3.11), and longer period geomagnetic trends can easily be identified. I-9 represents a broad shallow inclination feature (or pair of features) between ~13.5 and 10.5 ka in Burial Lake, deviating from GAD predictions by 28° (and as much as 38° in the case of Hawaiian drill-core, SOH-4; Laj et al., 2002). I-10 represents a series of rapid, large amplitude inclination anomalies occurring between ~22 and ~15 ka, with a maximum amplitude range of 37° for Burial Lake. These follow a long, fairly consistent shallowing inclination trend, beginning around 28.5 ka in the Burial Lake record. The beginning of this trend, as indicated by feature I-11, also corresponds to a brief return to GAD predictions, with inclinations for most records lying shallower than GAD immediately prior and subsequent to this time. By adopting the "Frozen Flux Hypothesis" (Roberts and Scott, 1965; Backus, 1968) and a core dynamic assumption (e.g., Le Mouël, 1984; Bloxham and Jackson, 1991), it is possible to attribute observed changes in PSV to large-scale magnetohydrodynamic motions at the core-mantle boundary (CMB; Hulot et al., 2010). From a geodynamo perspective then, it is somewhat unsurprising that paleomagnetic

records would co-vary between closely spaced sites within the Alaskan Arctic. However, the observation that Burial Lake and other PSV records are similar in character to far-field sites (e.g., Siberia and Hawaii) is unforeseen, and suggests large-scale, coherent core-fluid dynamic regimes, expressed over surface geographical extents >5,000 km, and persisting over glacial-interglacial timescales.

Similar to Holocene comparisons (Fig. 3.9 and 3.10), we find the identification of correlative features in declination somewhat difficult over this longer time scale. Although large amplitude, short-period variations in declination are clearly prevalent in all the records, long period trends are virtually nonexistent, with declinations remaining fairly constant about a mean (Fig. 3.11). Perhaps this is an artifact of rotating core sections about a mean declination of 0° to create a composite record, or perhaps this is truly reflective of the geomagnetic field. If the latter is true, it may be due to the sensitivity of particular surface locations on Earth to the radial component of magnetic flux generated at the CMB (Hulot et al., 2010). It is becoming more evident that the surface expression of magnetic flux at the CMB can be manifested differently in different vector components depending on a site's position relative to magnetic attractors (i.e., flux lobes; Amit et al., 2010, Stoner et al., 2013). In this case, inclination (rather than declination) may be a more dynamic geomagnetic indicator for the Alaskan Arctic and high-latitude Pacific regions. The notion of a particular site/region having a geomagnetic "predilection" for a particular component of the magnetic field vector is not a novel idea. For instance, in the North Atlantic and Europe, declination (rather than inclination) often produces higher amplitude, more distinctive regional features (e.g., the "F-event", Turner and Thompson, 1981), which have been successfully used to correlate PSV records across the region (Strano et al., *in prep*). Though the F-event is clearly evident in Holocene declination records from North America (labeled as D-2 in Fig. 3.10, which occurs ~2.5 ka), it is either absent or less recognizable in Burial Lake and other records from the Alaskan Arctic (Fig 3.9).

3.7.3 Holocene-Pleistocene Geomagnetic Disparities

Two major Holocene-Pleistocene distinctions are observed, particularly evident in inclination anomaly records shown in Figures 3.9 – 3.11. First, Holocene inclinations are

collectively much closer to GAD predictions for individual site latitudes, whereas inclinations throughout most of the Pleistocene are substantially shallower than GAD. Second, regional records show only small deviations from GAD predictions during the Holocene, while larger amplitude directional features are prevalent beyond 10 ka. Considering the paucity of declination data, we compute the root mean square (RMS) of inclination anomalies in each interval (0-10 ka, and >10 ka) providing an indication of Holocene-Pleistocene geomagnetic field variability (Table 3.2). For the records that span both intervals, RMS values, in every case, are higher in the Pleistocene (e.g., 10.48 versus 3.91 for Burial Lake). Pleistocene RMS values average 11.16, compared with 6.65 for Holocene data. Though there are significantly more Holocene data constraining this observation, this suggests that the Pleistocene geomagnetic field is on average, 67.8% more variable than that of the Holocene.

Bearing a resemblance to Holocene-Pleistocene climate variability, the Holocene has certainly been a uniquely "quiet" time period, with no observed reversals or excursions (Cande and Kent, 1995), and subdued secular variation referenced as a distinguishing feature of Pacific hemisphere paleomagnetic records (the Pacific non-dipole low; Doell and Cox, 1972; Peng and King, 1992; Gubbins and Gibbons, 2004). We suggest, however, that this subdued behavior is limited to the Holocene time interval, and as with climate, the Pleistocene environment can be characterized by much more dynamic behavior.

Certainly, these Holocene-Pleistocene discrepancies may be partly attributed to paleomagnetic acquisition processes operating within distinctive sedimentation regimes. Differential sedimentation rates, varying inputs of organic matter, contrasting sediment compositions, etc., could potentially induce artifacts in records spanning the two intervals. However, the same discrepancies are observed in the Hawaiian lava record, SOH-4 (Fig. 3.11; Laj et al., 2002), and therefore cannot simply be explained by changing boundary conditions in a sedimentary environment. We therefore look towards a geomagnetic explanation that may explain both of these observations.

The Holocene geomagnetic field has been shown to be hemispherically asymmetric, with a dipole axis offset to the west, resulting in stronger geomagnetic field intensity in the Western (Pacific) Hemisphere than in the Eastern (Atlantic) Hemisphere

(Hulot et al., 2002; Gallet et al., 2009; Korte et al., 2011). Low secular variation in the Pacific is therefore assumed to be a product of this asymmetry, with higher intensities limiting non-dipole contributions and commanding a more GAD-like representation of the field. By this notion, the Pacific has been formally regarded as a "dipole window." Mathematically described as an "eccentric-dipole", this western offset of the dipole axis has been attributed to lopsided inner-core growth, with dipole axis offset in the direction of fastest inner core crystallization (Olsen and Denguen., 2012). Following on this hypothesis, higher amplitude variations in the Pleistocene could be attributed to faster Eastern Hemisphere growth, and a shift of the dipole axis towards the east. Moreover, global paleointensity estimates (e.g., Guyodo and Valet, 1996; Laj et al., 2002; 2004; Stoner et al., 2002; Knudsen et al., 2008) show diminished Pleistocene field strengths, which may have permitted a "leakage" of non-dipole components, contributing to a more dynamic geomagnetic field. In contrast, field strength has increased during the Holocene, perhaps allowing a more stable, GAD-like field to persist. Of course these global paleointensity fluctuations may also in fact be superimposed on hemispheric tendencies.

3.8 Conclusions

With the addition of the Burial Lake paleomagnetic record, we now have a greater understanding of full-vector paleomagnetic secular variation in the Alaskan Arctic, helping to fill a significant data gap in our growing paleomagnetic database. Having demonstrated the quality of paleomagnetic data, which overcome significant lithologic complexity and bear strong resemblance to other regional records, we argue that it should be included in the next generation of continuous spherical harmonic models, and further developed as a regional stratigraphic dating tool. Although quality of paleomagnetic data appears to suffer, Holocene sediments possess inclinations values consistent with GAD estimates and produce what is perhaps the only reliable interval of RPI. This begs the question of whether postglacial sediments produce a truer geomagnetic signal of origin than their glacial-age counterparts, with differences between glacial-interglacial sedimentation regimes conceivably shedding future light on the poorly understood magnetic acquisition process. While high-coercivity components are traditionally thought to be detrimental to the paleomagnetic record, we demonstrate that in some

cases, this may be a not so forbidden realm, and suggest the paleomagnetic community reassess certain reliability criteria for sediments thought to provide high-fidelity records of PSV. As an example, normalized remanence results for the Burial Lake record suggest that the integrity of RPI signal appears more sensitive to variable magnetic concentration than to high-coercivity contributions. Spanning the last ~37,000 years, Burial Lake provides one of the longest, and more precisely dated PSV records from the region, capable of extending our understanding of geomagnetic variability beyond the Holocene and into the Pleistocene, not only in the Alaskan Arctic, but also across the broader Pacific hemisphere. We identify distinct modes of geomagnetic variability associated with each interval and place them in context with deep Earth processes as well as hemispheric and global paleointensity, which appear the regulate the dipole nature of the field.

3.9 References

Abbott, M.B., Edwards, M.E., Finney, B.P., 2010. A 40,000-yr record of environmental change from Burial Lake in Northwest Alaska. Quaternary Research 74, 156–165.

Amit, H., Aubert, J., Hulot, Gauthier, 2010. Stationary, oscillating or drifting mantle-driven geomagnetic flux patches? Journal of Geophysical Research: Solid Earth (1978–2012) 115.

Andrews, J.T., Jennings, A.E., 1990. Geomagnetic secular variations (inclination) of high latitude fiord cores: eastern Canadian Arctic*. Polar Research 8, 245–259.

Aurnou, J., Andreadis, S., Zhu, L., Olson, P., 2003. Experiments on convection in Earth's core tangent cylinder. Earth and Planetary Science Letters 212, 119–134.

Backus, G.E., 1968. Kinematics of geomagnetic secular variation in a perfectly conducting core. Philosophical Transactions of the Royal Society of London. Series A, Mathematical and Physical Sciences 263, 239–266.

Barletta, F., St-Onge, G, Stoner, J., Lajeunesse, P., Locat, J., 2010. A high-resolution Holocene paleomagnetic secular variation and relative paleointensity stack from eastern Canada. Earth and Planetary Science Letters 298, 162–174.

Barletta, F., St-Onge, G., Channell, J.E., Rochon, A., Polyak, L., Darby, D., 2008. High-resolution paleomagnetic secular variation and relative paleointensity records from the western Canadian Arctic: implication for Holocene stratigraphy and geomagnetic field behaviour. Canadian Journal of Earth Sciences 45, 1265–1281.

Blaauw, M., 2010. Methods and code for "classical" age-modelling of radiocarbon sequences. Quaternary Geochronology 5, 512–518.

Bloxham, J., Gubbins, D., 1985. The secular variation of Earth's magnetic field. Nature 317, 777–781.

Bloxham, J., Jackson, A., 1991. Fluid flow near the surface of Earth's outer core. Rev. Geophys. 29, 97–120.

Brachfeld, S.A., Banerjee, S.K., 2000. A new high-resolution geomagnetic relative paleointensity record for the North American Holocene: A comparison of sedimentary and absolute intensity data. Journal of Geophysical Research: Solid Earth (1978–2012) 105, 821–834.

Butler, R.F., 1984. Paleomagnetism: Magnetic domains to geologic terranes. Originally published by Blackwell in. C. S. G. Gogorza, A. M. Sinito, J. F. Vilas, K. M. Creer, H. Nuñez, 2002. Geomagnetic secular variations over the last 6500 years as recorded by sediments from the lakes of south Argentina. Geophys J 143, 787–798.

Cande, S.C., Kent, D.V., 1995. Revised calibration of the geomagnetic polarity timescale for the Late Cretaceous and Cenozoic. J. Geophys. Res. 100, 6093–6095.

Chulliat, A., Thébault, E., Hulot, G., 2010. Core field acceleration pulse as a common cause of the 2003 and 2007 geomagnetic jerks. Geophys. Res. Lett. 37, L07301.

Clark, P.U., Dyke, A.S., Shakun, J.D., Carlson, A.E., Clark, J., Wohlfarth, B., Mitrovica, J.X., Hostetler, S.W., McCabe, A.M., 2009. The Last Glacial Maximum. Science 325, 710–714.

Clark, P.U., Shakun, J.D., Baker, P.A., Bartlein, P.J., Brewer, S., Brook, E., Carlson, A.E., Cheng, H., Kaufman, D.S., Liu, Z., Marchitto, T.M., Mix, A.C., Morrill, C., Otto-Bliesner, B.L., Pahnke, K., Russell, J.M., Whitlock, C., Adkins, J.F., Blois, J.L., Clark, J., Colman, S.M., Curry, W.B., Flower, B.P., He, F., Johnson, T.C., Lynch-Stieglitz, J., Markgraf, V., McManus, J., Mitrovica, J.X., Moreno, P.I., Williams, J.W., 2012. Global climate evolution during the last deglaciation. Proceedings of the National Academy of Sciences.

Cox, A., 1970. Latitude dependence of the angular dispersion of the geomagnetic field*. Geophysical Journal of the Royal Astronomical Society 20, 253–269.

Creer, K.M., Tucholka, P., 1982. Construction of type curves of geomagnetic secular variation for dating lake sediments from east central North America. Can. J. Earth Sci. 19, 1106–1115.

Davies, M.H., Stoner, J., Mix, A.C., Southon, J., Jaeger, J., Rosen, G.P., Channell, J.E., (*in prep*). Reconstruction Holocene paleomagnetic secular variation from the Gulf of Alaska.

Day, R., Fuller, M., Schmidt, V., 1977. Hysteresis properties of titanomagnetites: grain-size and compositional dependence. Physics of the Earth and Planetary Interiors 13, 260–267.

Doell, R.R., Cox, A., 1972. The Pacific geomagnetic secular variation anomaly and the question of lateral uniformity in the lower mantle. The nature of the solid earth 245–284.

Dorfman, J.M., Stoner, J.S., Finkenbinder, M.S., Abbott, M.B., Xuan, C., St-Onge, G. (*In prep*). A 37,000-year environmental magnetic record of aeolian dust deposition from Burial Lake, Arctic Alaska.

Eisner, W.R., Colinvaux, P.A., 1992. Late Quaternary pollen records from Oil Lake and Feniak Lake, Alaska, USA. Arctic and Alpine Research 56–63.

Evans, M.M.E., Heller, F.A., 2003. Environmental magnetism:, International geophysics series. Academic Press, Incorporated.

Frank, U., Nowaczyk, N., Negendank, J., Melles, M, 2002. A paleomagnetic record from Lake Lama, northern Central Siberia. Physics of the Earth and Planetary Interiors 133, 3–20.

Gallet, Y., Hulot, Gauthier, Chulliat, Arnaud, Genevey, Agnès, 2009. Geomagnetic field hemispheric asymmetry and archeomagnetic jerks. Earth and Planetary Science Letters 284, 179–186.

Geiss, C., Banerjee, S., 2003. A Holocene—Late Pleistocene geomagnetic inclination record from Grandfather Lake, SW Alaska. Geophysical Journal International 153, 497–507.

Gubbins, D., Gibbons, S.J., 2004. Low Pacific secular variation. Timescales of the Paleomagnetic Field, Geophys. Monogr. Ser 145, 279–286.

Guyodo, Y., Valet, J.-P., 1996. Relative variations in geomagnetic intensity from sedimentary records: the past 200,000 years. Earth and Planetary Science Letters 143, 23–36.

Hagstrum, J.T., Champion, D.E., 2002. A Holocene paleosecular variation record from 14C-dated volcanic rocks in western North America. Journal of Geophysical Research: Solid Earth (1978–2012) 107, EPM–8.

Hamilton, T.D., 2001. Quaternary glacial, lacustrine, and fluvial interactions in the western Noatak basin, Northwest Alaska. Quaternary Science Reviews 20, 371–391.

Hamilton, T.D., 2010, Surficial geologic map of the Noatak National Preserve, Alaska: U.S. Geological Survey Scientific Investigations Map 3036, 1 sheet, scale 1:250,000, 1 pamphlet, 21 p.

Hamilton, T.D., Van Etten, D.P., 1984. Late Pleistocene glacial dams in the Noatak valley. In: Conrad, W.L., Elliott, R.L. (Eds.), The United States Geological Survey in Alaska: Accomplishments During 1981. U.S. Geol. Survey Circular 868, pp. 21-23.

Hayashida, A., Ali, M., Kuniko, Y., Kitagawa, H., Torii, M., Takemura, K., 2007. Environmental magnetic record and paleosecular variation data for the last 40 kyrs from the Lake Biwa sediments, Central Japan. Earth, Planets, and Space 59, 807–814.

Heslop, D., Dekkers, M.J., Kruiver, P.P., Van Oorschot, I.H.M., 2002. Analysis of isothermal remanent magnetization acquisition curves using the expectation–maximization algorithm. Geophysical Journal International 148, 58–64.

Hillaire-Marcel, C., 2008. Decadal-to millennial-scale variability of Arctic-Subarctic oceans and adjacent lands: a contribution of the Polar Climate Stability Network of Canada to the International Polar Year. Canadian Journal of Earth Sciences 45, 1199–1201.

Hulot, G., Finlay, C., Constable, C., Olsen, N., Mandea, M., 2010. The magnetic field of planet Earth. Space science reviews 152, 159–222.

Hulot, Gauthier, Eymin, C., Langlais, B., Mandea, M., Olsen, N., 2002. Small-scale structure of the geodynamo inferred from Oersted and Magsat satellite data. Nature 416, 620–623.

Huybers, P., Wunsch, C., 2004. A depth-derived Pleistocene age model: Uncertainty estimates, sedimentation variability, and nonlinear climate change. Paleoceanography 19, PA1028.

Jackson, A., Jonkers, A.R.T., Walker, M.R., 2000. Four centuries of geomagnetic secular variation from historical records. Philosophical Transactions of the Royal Society of London. Series A: Mathematical, Physical and Engineering Sciences 358, 957–990.

King, J.W., and Channel, J.E.T., 1991, Sedimentary magnetism, environmental magnetism, and magnetostratigraphy: Reviews of Geophysics, Supplement, p. 358-370.

King, J.W., Banerjee, S.K., Marvin, J., 1983. A new rock-magnetic approach to selecting sediments for geomagnetic paleointensity studies: Application to paleointensity for

the last 4000 years. Journal of Geophysical Research: Solid Earth (1978–2012) 88, 5911–5921.

Kirschvink, J., 1980. The least-squares line and plane and the analysis of palaeomagnetic data. Geophysical Journal International 62, 699–718.

Knudsen, M.F., Riisager, P., Donadini, Fabio, Snowball, I., Muscheler, R., Korhonen, K., Pesonen, L.J., 2008. Variations in the geomagnetic dipole moment during the Holocene and the past 50 kyr. Earth and Planetary Science Letters 272, 319–329.

Korte, M, Donadini, F, Constable, CG, 2009. Geomagnetic field for 0–3 ka: 2. A new series of time-varying global models. Geochemistry, Geophysics, Geosystems 10.

Korte, M, Genevey, A, Constable, CG, Frank, U., Schnepp, E., 2005. Continuous geomagnetic field models for the past 7 millennia: 1. A new global data compilation. Geochemistry, Geophysics, Geosystems 6.

Korte, Monika, Constable, Catherine, 2003. Continuous global geomagnetic field models for the past 3000 years. Physics of the Earth and Planetary Interiors 140, 73–89.

Korte, Monika, Constable, Catherine, 2011. Improving geomagnetic field reconstructions for 0–3ka. Physics of the Earth and Planetary Interiors 188, 247–259.

Korte, Monika, Constable, Catherine, Donadini, Fabio, Holme, R., 2011. Reconstructing the Holocene geomagnetic field. Earth and Planetary Science Letters 312, 497–505.

Laj, Carlo, Kissel, Catherine, Beer, J., 2004. High resolution global paleointensity stack since 75 kyr (GLOPIS-75) calibrated to absolute values. Timescales of the Paleomagnetic Field, Geophys. Monogr. Ser 145, 255–265.

Laj, Carlo, Kissel, Catherine, Scao, V., Beer, J., Thomas, D.M., Guillou, H., Muscheler, R., Wagner, G., 2002. Geomagnetic intensity and inclination variations at Hawaii for the past 98kyr from core SOH-4 (Big Island): a new study and a comparison with existing contemporary data. Physics of the Earth and Planetary Interiors 129, 205–243.

Le Mouël, J.L., 1984. Outer-core geostrophic flow and secular variation of Earth's geomagnetic field. Nature 311, 734–735.

Lisé-Pronovost, A., St-Onge, G., Brachfeld, S., Barletta, Francesco, Darby, D., 2009. Paleomagnetic constraints on the Holocene stratigraphy of the Arctic Alaskan margin. Global and Planetary Change 68, 85–99.

Lund, S.P., 1996. A comparison of Holocene paleomagnetic secular variation records from North America. J. Geophys. Res. 101, 8007–8024.

Lund, S.P., Banerjee, S.K., 1985. Late Quaternary paleomagnetic field secular variation from two Minnesota Lakes. J. Geophys. Res. 90, 803–825.

Marcott, S.A., Shakun, J.D., Clark, P.U., Mix, A.C., 2013. A Reconstruction of Regional and Global Temperature for the Past 11,300 Years. Science 339, 1198–1201.

Nowaczyk, N.R., Harwart, S., Melles, Martin, 2001. Impact of early diagenesis and bulk particle grain size distribution on estimates of relative geomagnetic palaeointensity variations in sediments from Lama Lake, northern Central Siberia. Geophysical Journal International 145, 300–306.

Olson, P., Deguen, R., 2012. Eccentricity of the geomagnetic dipole caused by lopsided inner core growth. Nature Geoscience 5, 565–569.

Opdyke, M.D., Channell, J.E., 1996. Magnetic stratigraphy. Academic Press.

Oswald, W.W., Anderson, P.M., Brown, T.A., Brubaker, L.B., Feng Sheng Hu, Lozhkin, A.V., Tinner, W., Kaltenrieder, P., 2005. Effects of sample mass and macrofossil type on radiocarbon dating of arctic and boreal lake sediments. Holocene 15, 758–767.

Peck, J., King, J., Colman, S., Kravchinsky, V., 1996. An 84-kyr paleomagnetic record from the sediments of Lake Baikal, Siberia. Journal of geophysical research 101, 11365–11.

Peng, L., King, J.W., 1992. A late Quaternary geomagnetic secular variation record from Lake Waiau, Hawaii, and the question of the Pacific nondipole low. Journal of Geophysical Research: Solid Earth (1978–2012) 97, 4407–4424.

Reimer, P.J., Baillie, M.G.L., Bard, E., Bayliss, A., Beck, J.W., Blackwell, P.G., Ramsey, C.B., Buck, C.E., Burr, G.S., Edwards, R.L., Friedrich, M., Grootes, P.M., Guilderson, T.P., Hajdas, I., Heaton, T.J., Hogg, A.G., Hughen, K.A., Kaiser, K.F., Kromer, B., McCormac, F.G., Manning, S.W., Reimer, R.W., Richards, D.A., Southon, J.R., Talamo, S., Turney, C.S.M., Plicht, J. van der, Weyhenmeyer, C.E., 2011. IntCal09 and Marine09 Radiocarbon Age Calibration Curves, 0-50,000 Years cal BP. Radiocarbon 51, 1111–1150.

Roberts, A.P., Tauxe, L., Heslop, D., 2013. Magnetic paleointensity stratigraphy and high-resolution Quaternary geochronology: successes and future challenges. Quaternary Science Reviews 61, 1–16.

Roberts, P., Scott, S., 2003. On analysis of the secular variation. Magnetohydrodynamics and the Earth's Core: Selected Works of Paul Roberts 10, 15.

Snowball, I., Sandgrena, P., 2002. Geomagnetic field variations in northern Sweden during the Holocene quantified from varved lake sediments and their implications for cosmogenic nuclide production rates. The Holocene 12, 517–530.

Snowball, I., Zillén, L., Ojala, A., Saarinen, T., Sandgren, P., 2007. FENNOSTACK and FENNORPIS: Varve dated Holocene palaeomagnetic secular variation and relative palaeointensity stacks for Fennoscandia. Earth and Planetary Science Letters 255, 106–116.

St-Onge, G., Mulder, T., Francus, P., Long, B., 2007. Chapter Two Continuous Physical Properties of Cored Marine Sediments. Developments in Marine Geology 1, 63–98.

St-Onge, G., Stoner, J.S., Hillaire-Marcel, C., 2003. Holocene paleomagnetic records from the St. Lawrence Estuary, eastern Canada: centennial- to millennial-scale geomagnetic modulation of cosmogenic isotopes. Earth and Planetary Science Letters 209, 113–130.

Stober, J.C., Thompson, R., 1979. An investigation into the source of magnetic minerals in some Finnish lake sediments. Earth and Planetary Science Letters 45, 464–474.

Stoner, J.S., Channell, J.E.T., Mazaud, A., Strano, S.E., Xuan, C., 2013. The influence of high latitude flux lobes on the Holocene paleomagnetic record of IODP Site U1305 and the northern North Atlantic. Submitted to Geochemistry, Geophysics, and Geosystems (G-Cubed).

Stoner, J.S., Jennings, A., Kristjánsdóttir, G.B., Dunhill, G., Andrews, J.T., Hardardóttir, J., 2007. A paleomagnetic approach toward refining Holocene radiocarbon-based chronologies: Paleoceanographic records from the north Iceland (MD99-2269) and east Greenland (MD99-2322) margins. Paleoceanography 22.

Stoner, J.S., Laj, C, Channell, J., Kissel, C, 2002. South Atlantic and North Atlantic geomagnetic paleointensity stacks (0–80ka): implications for inter-hemispheric correlation. Quaternary Science Reviews 21, 1141–1151.

Stoner, J.S., St-Onge, G., 2007. Chapter Three Magnetic Stratigraphy in Paleoceanography: Reversals, Excursions, Paleointensity, and Secular Variation. Developments in Marine Geology 1, 99–138.

Strano, S.E., Stoner, J.S., Xuan, C., Marcott, S.A., Almasi, P. (*in prep*), Paleomagnetic acquisition induced Age Offset and smoothing of Deep-sea Sediment.

Stuiver, M. and Polach, H.A., 1977. Discussion: Reporting of 14C data. Radiocarbon, 19:355-363.

Stuiver, M., Reimer, P. J., and Reimer, R. W. 2005. CALIB 5.0. [program and documentation]. http://calib.qub.ac.uk/calib/

Tauxe, L., 1993. Sedimentary records of relative paleointensity of the geomagnetic field: theory and practice. Reviews of geophysics 31, 319–354.

Thompson, R. 1984: A global review of paleomagnetic results from wet lake sediments. Pg. 145-164 in Haworth, E. Y. & Lund, J. W. G. (eds.): Lake Sediments and Environmental History. University of Minnesota Press, Minneapolis.

Thompson, R., Oldfield, F., 1986. Environmental Magnetism. Allen & Unwin.

Turner, G.M., Turner, G., Thompson, R., 1981. Lake sediment record of the geomagnetic secular variation in Britain during Holocene times. Geophysical Journal International 65, 703–725.

Verosub, K.L., 1977. Depositional and postdepositional processes in the magnetization of sediments. Reviews of Geophysics 15, 129–143.

Verosub, K.L., Mehringer, P.J., Waterstraat, P., 1986. Holocene secular variation in western North America: Paleomagnetic record from Fish Lake, Harney County, Oregon. J. Geophys. Res. 91, 3609–3623.

Xuan, C., Channell, J.E.T., 2009. UPmag: MATLAB software for viewing and processing u channel or other pass-through paleomagnetic data. Geochem. Geophys. Geosyst. 10, Q10Y07.

Xuan, C., Stoner, J.S., Mix, A.C., VanLaningham, S., (*in prep*). Northeast Pacific geomagnetic and environmental change during the last 140 kyr recorded by deep-sea sediment core EW9504-17PC.

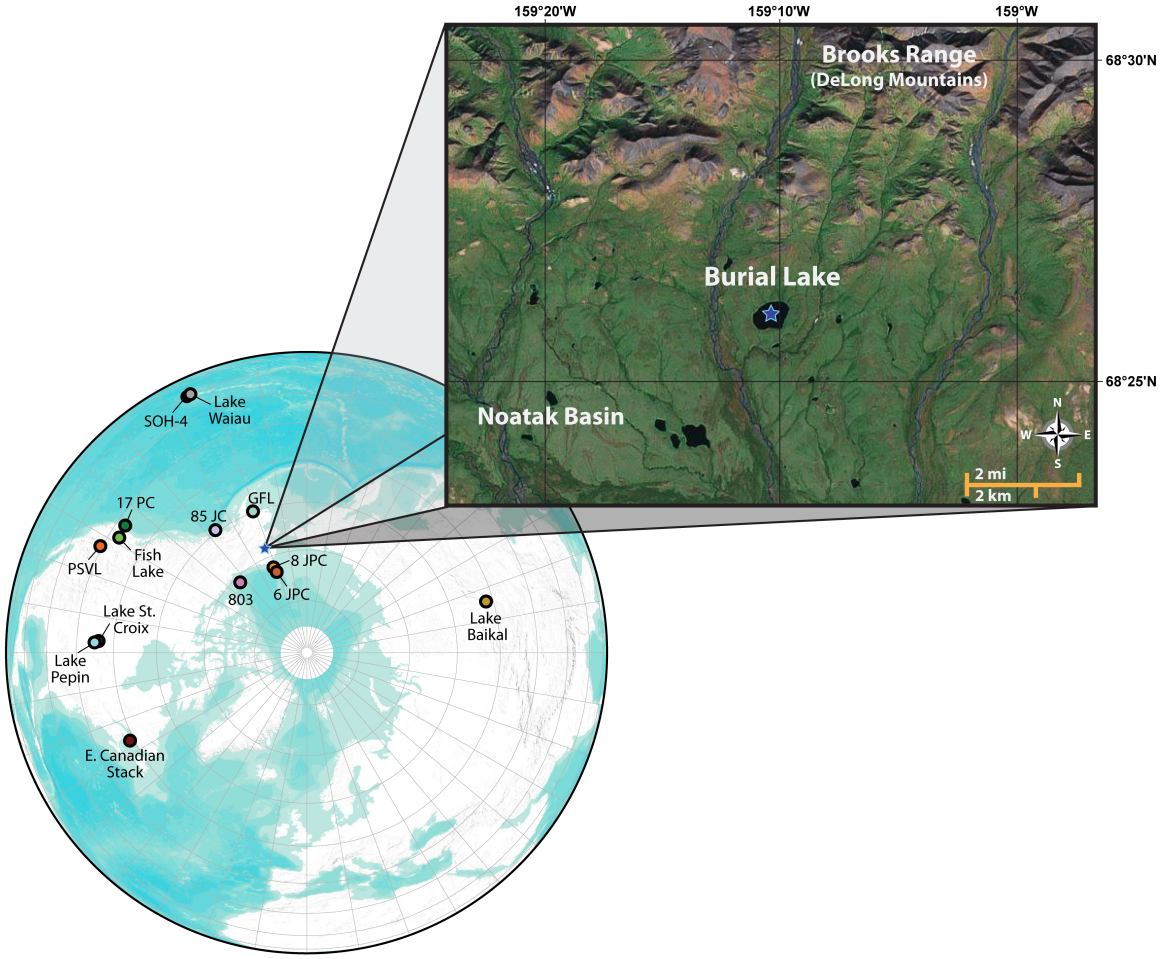

Figure 3.1 – Site location map. Burial Lake (68.43°N, 159.17°W) is located in Noatak Basin in the northwest Brooks Range, Arctic Alaska, at the foot of the DeLong Mountains. Locations of other regional PSV records presented in this study are given, with colors corresponding to profiles in Figures 3.9 – 3.11. These include: cores 8 JPC and 6 JPC (Chukchi Sea; Lisé-Pronovost et al., 2009), 803 (Beaufort Sea; Barletta et al., 2008), 85 JC (Gulf of Alaska; Davies et al., *in prep*), Grandfather Lake (GFL, southwest mainland Alaska; Geiss and Banerjee, 2003), a PSV record from lava flows in western North America (PSVL; Hagstrum and Champion), Fish Lake (Oregon; Verosub et al., 1986), Lake St. Croix (Minnesota; Lund and Banerjee, 1985), Lake Pepin (Minnesota; Brachfeld and Banerjee, 2000); the Eastern Canadian Stack (Laurentian Channel; Barletta et al., 2010), Lake Waiau (Hawaii; Peng and King, 1992), the Hawaiian lava record drilled from the Kilauea volcano (SOH-4; Laj et al., 2002), Lake Baikal (south-central Siberia; Peck et al., 1996), and core 17 PC (Oregon margin; Xuan et al., *in prep*).

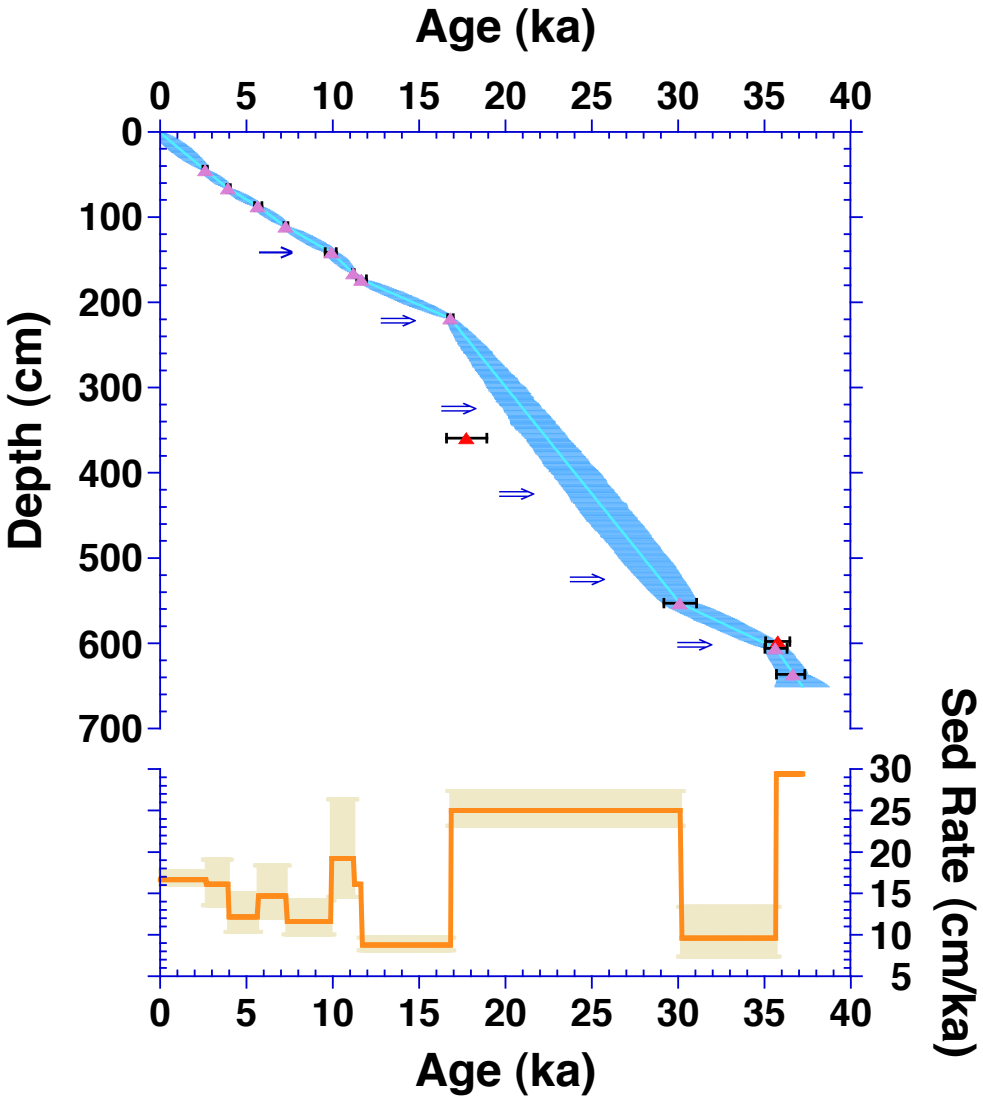

Figure 3.2 – AMS radiocarbon results based on terrestrial macrofossils identified in deep basin cores A10 and C10, which were stratigraphically correlated to produce a composite depth scale (see Appendix A). Radiocarbon ages were calibrated using Calib 6.0 (Stuiver et al., 2005) and the IntCal09 calibration curve (Reimer et al., 2009). Eleven calibrated median radiocarbon ages (pink triangles) are shown with associated 2σ error bars, as well as two dates, which were excluded from the age model (red triangles – see text for explanation). *CLAM* software for "classical" non-Bayesian age-depth modeling (Blaauw, 2010) was used to produce the "best fit" linearly interpolated age (cyan line) for the 6.51 m A10 core. Locations of A10 section breaks are shown for overlapping (→) and abutted (⇒) sections. The blue shaded envelope represents the maximum age variance computed between age control points based on the 2σ calibrated ^{14}C ages. It is the maximum AR1 normalized 1σ standard deviation computed from 10,000 Monte Carlo simulations following a random draw from a normal distribution (Marcott et al., 2013) with uncertainty between age control points based on a random walk model after Huybers and Wunsch, (2004), using a "jitter factor" of 200. The orange line represents sedimentation rate over the ~37,000-year time interval with uncertainty generated using the 2σ calibrated age range of each age control point where feasible.

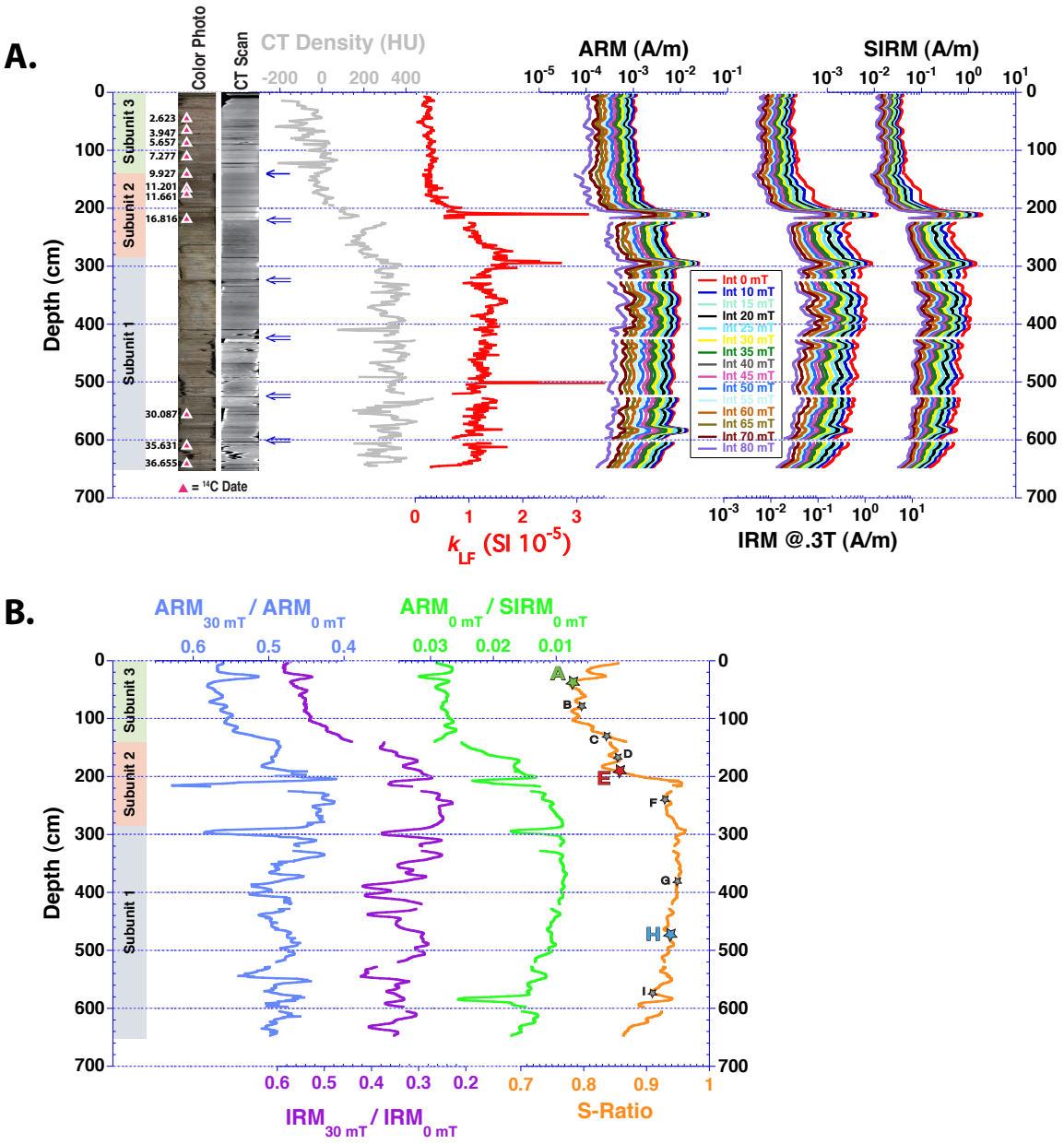

Figure 3.3 – Down-core physical and magnetic results subdivided into lithologic subunits according to Dorfman et al., (*in prep*). Subunit 1 (651-285 cm), Subunit 2 (285-140 cm), and Subunit 3 (140 – 0 cm), respectively correspond to the last glacial period (37.2 – 19.4 ka), the deglacial transition (19.4 – 9.8 ka), and the Holocene (9.8 ka – present). **A)** (From left to right): Color photo with locations of ^{14}C dates and mean calibrated ages for reference, computer tomography (CT) image with locations of A10 section breaks for overlapping (←) and abutted (⇐) sections, CT density, magnetic susceptibility (k_{LF}), anhysteretic remanent magnetization (ARM), isothermal remanent magnetization (IRM), and saturation isothermal remanent magnetization (SIRM), plotted with their respective AF demagnetization steps ranging from 10-80 mT. Note, some parameters are plotted on a log scale. **B)** (From left to right): Demagnetization ratios of ARM_{30mT}/ARM_{0mT} and IRM_{30mT}/IRM_{0mT}, $ARM_{0mT}/SIRM_{0mT}$ (magnetic grain size proxy), and S-Ratios (magnetic mineralogy indicator). Stars and lettering placed over S-Ratios indicate sample locations for IRM acquisition/decomposition, with enlarged colored symbols indicating representative samples in each lithologic subunit.

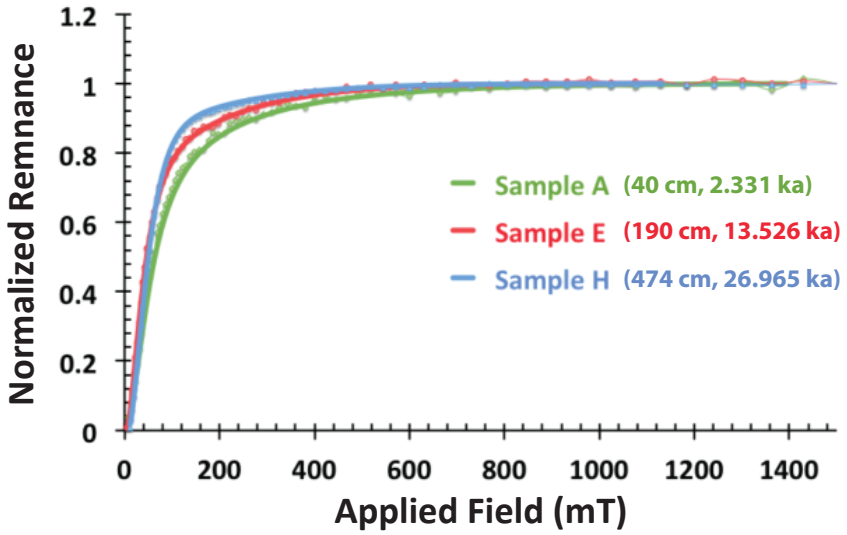

Figure 3.4 – Representative normalized IRM acquisition curves from Subunit 1 (H: 474 cm, 26.965 ka), Subunit 2 (E: 190 cm, 13.526 ka), and Subunit 3 (A: 40 cm, 2.331 ka). Sample A displays higher coercivity behavior than samples E and H, consistent with a distinctive change in mineralogy. Raw data points were smoothed using a MATLAB™ loess filter prior to IRM decomposition as is indicated by the thick solid lines.

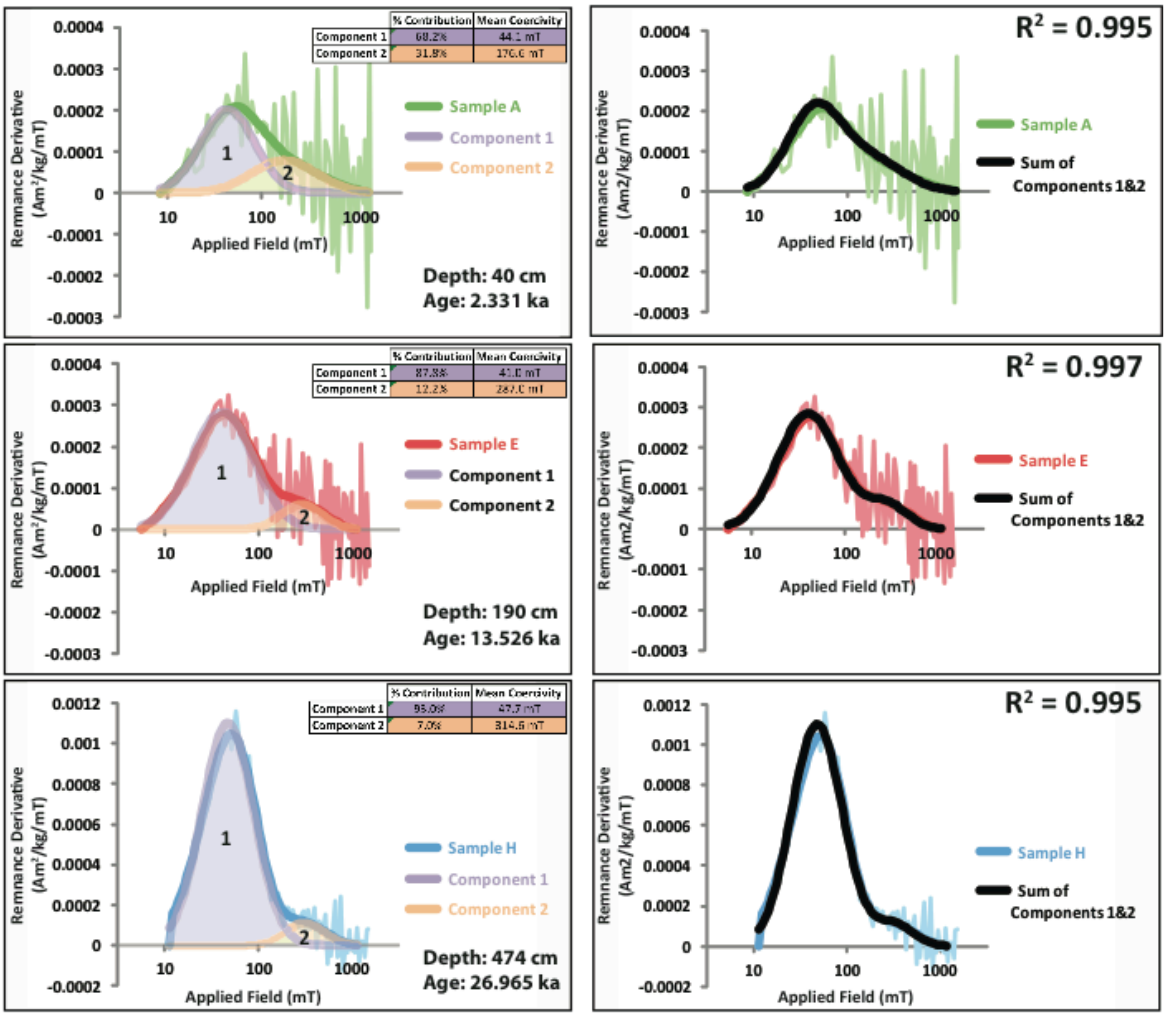

Figure 3.5 – **Left column:** IRM decomposition results based on smoothed data from Figure 3.4. Non-normalized input data for representative samples from Subunit 1 (H: 474 cm, 26.965 ka), Subunit 2 (E: 190 cm, 13.526 ka), and Subunit 3 (A: 40 cm, 2.331 ka) were analyzed using IRMUNMIX V2.2 (Heslop et al., 2002) to decompose curves into their individual component contributions. Raw data is shown behind the smoothed curve for each sample. Note, applied field is plotted on a log scale. Burial Lake sediments are best described by a two-component model, with both low-coercivity and high-coercivity sources present throughout the record. Component 1 (shaded purple) is characterized by low-coercivity minerals, and its relative abundance decreases by ~25% between Subunit 1 and Subunit 3. Despite, this decrease, it still appears to dominate the sediments in each interval. Component 2 (shaded orange) is characteristic of high-coercivity minerals and is ever-present throughout the record, but can easily be masked when low-coercivity components are in high abundance (e.g. sample H in Subunit 1). Relative percent contribution and mean coercivity for each component is tabulated for each sample. **Right column:** The sum of components 1 and 2 compared against the smoothed input data, with R^2 values given for each sample, demonstrating an excellent correlation. Raw data is again shown for reference behind the smoothed curves.

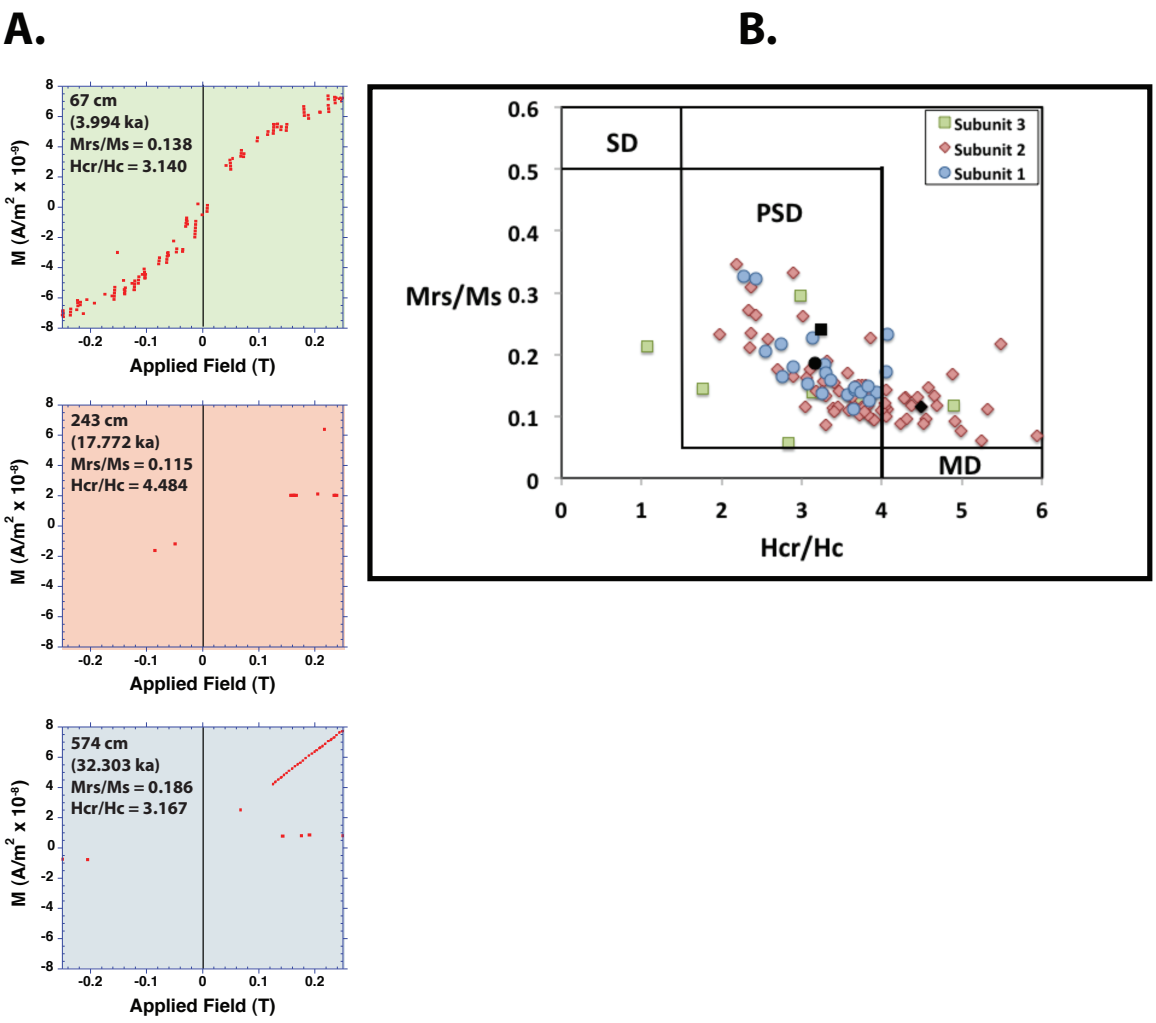

Figure 3.6 – Hysteresis results. **A)** Hysteresis loops generated from alternating gradient magnetometer (AGM) measurements on representative samples from each lithologic subunit. Uncorrected loops are shown (dashed lines) as well as those corrected for high-field paramagnetic/diamagnetic contributions. Shapes of loops demonstrate the presence of low-coercivity ferrimagnetic minerals such as (titano)magnetite, and also exhibit significant paramagnetic contributions. Noisy loops in Subunit 3 are indicative of low ferrimagnetic magnetic concentration. **B)** Hysteresis ratios of Hcr/Hc and Mrs/Ms plotted according to Day et al. (1977) for a number of samples within each subunit, with theoretical boundaries drawn according to the behavior of pure magnetite (Day et al., 1977). Most samples fall within the PSD-MD magnetic grain size rage including values derived from the hysteresis loops depicted here (black symbols), though scatter does occur - likely due to low ferrimagnetic concentration and/or high-coercivity components.

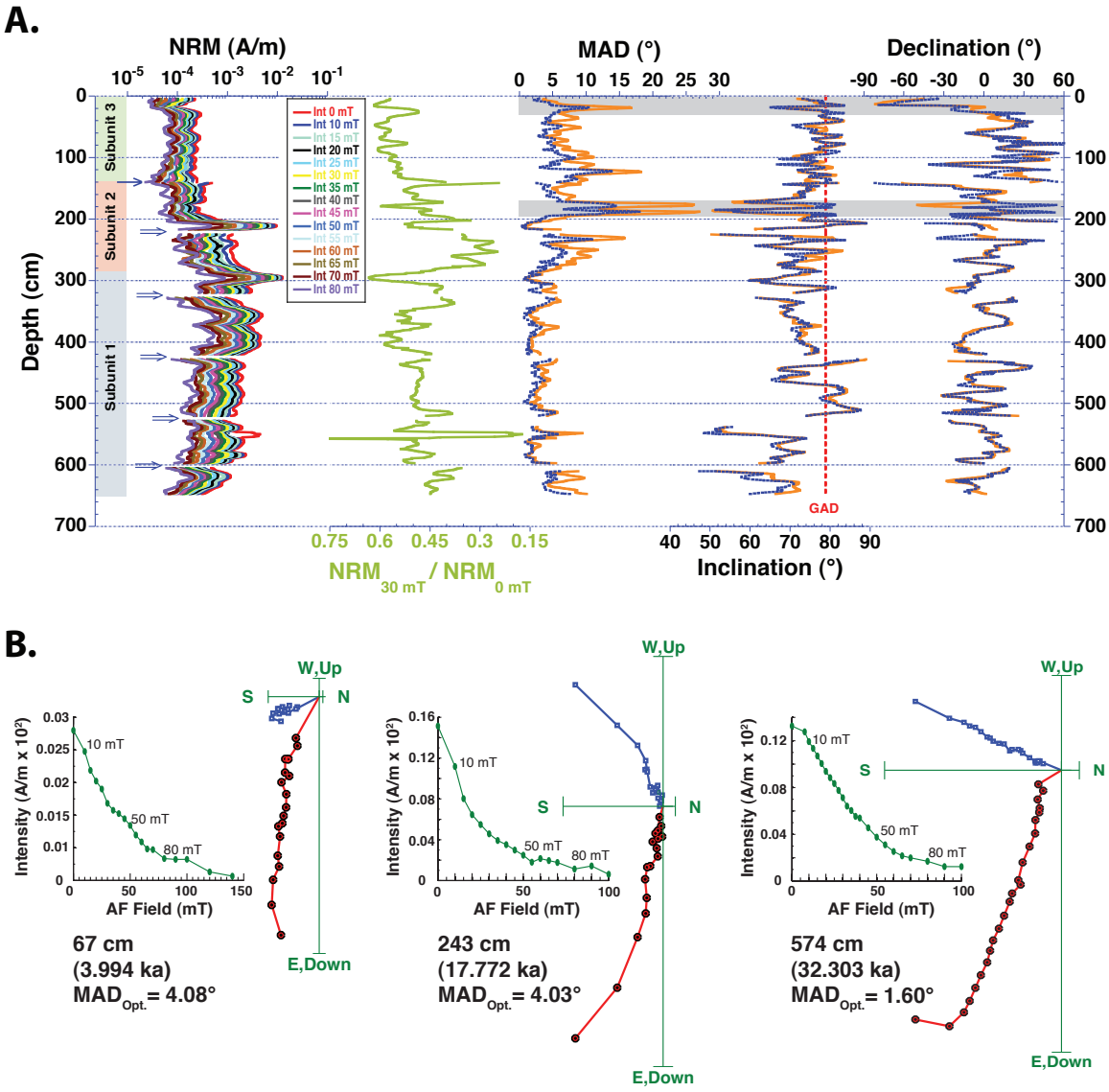

Figure 3.7 – **A)** Down-core paleomagnetic results versus depth: (From left to right) Natural remanent magnetization (NRM) with AF demagnetization steps ranging from 10-80 mT (plotted on a log scale), NRM_{30mT}/NRM_{0mT} demagnetization ratios, maximum angular deviation (MAD) values, component Inclinations with the geocentric axial dipole (GAD) prediction for site latitude (dashed red line), and component Declinations rotated to a mean 0°. MAD values and component directions were calculated based on principal component analysis (PCA), which defines the characteristic remanent magnetizations (ChRM) using both a "consecutive-range" (solid orange lines) and "optimized" (dashed blue lines) approach (see text for details). The interval from 0-25 cm is shaded grey, with aberrant directions and high MAD values, likely resulting from core-top disturbance. The interval from 170-194 cm (also shaded grey) contains high MAD values, and we suggest these data be treated with caution. Locations of A10 section breaks for overlapping (→) and abutted (⇒) sections are shown for reference. **B)** Vector endpoint diagrams (Zijderveld plots) and step-wise demagnetization plots showing demagnetization behavior of representative intervals from each lithologic subunit (same intervals as hysteresis results in Figure 3.6).

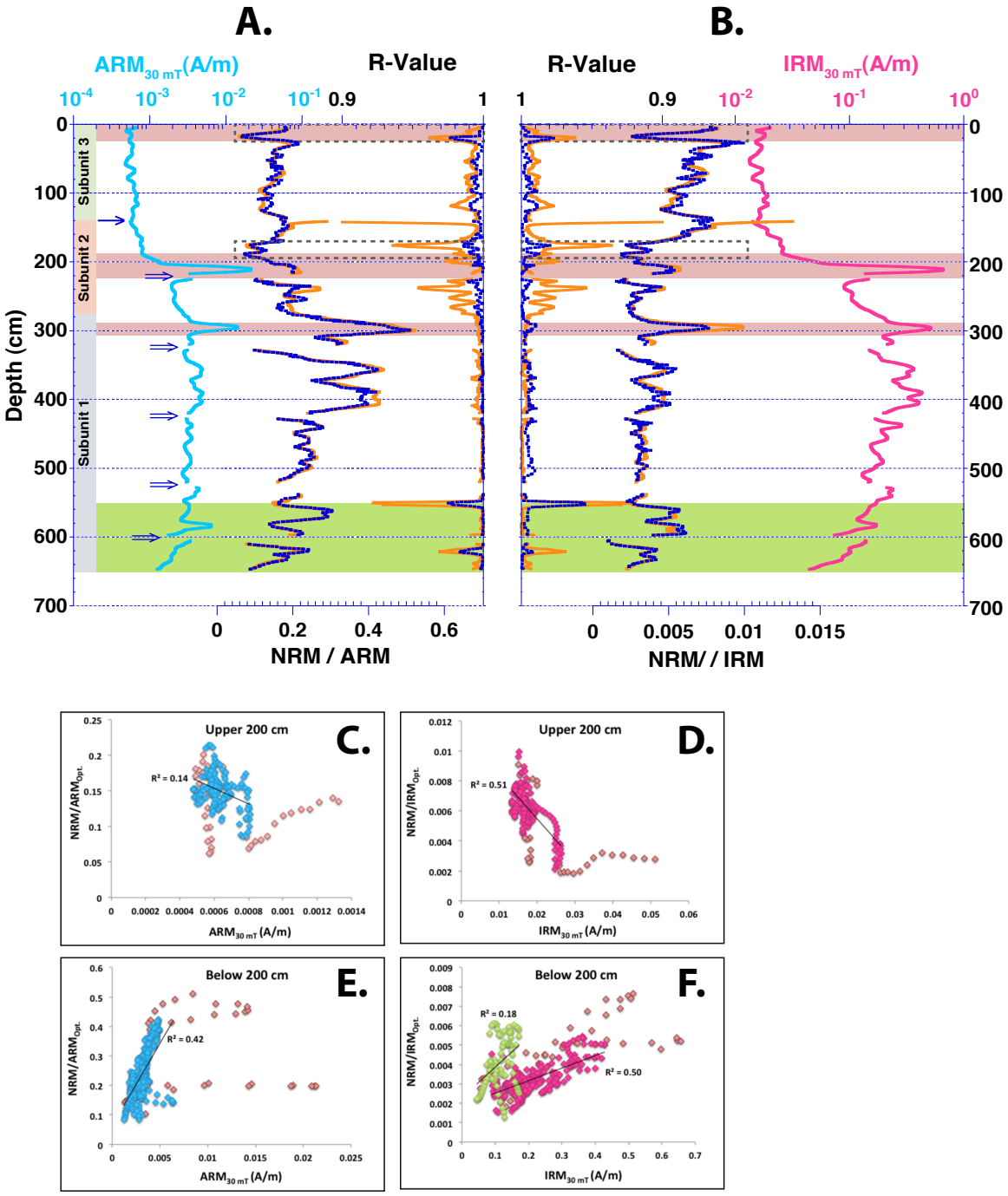
A.
B.
ARM30 mT(A/m)
R-Value
R-Value
IRM30 mT(A/m)
Depth (cm)
Subunit 3
Subunit 2
Subunit 1
NRM / ARM
NRM/ / IRM
C.
Upper 200 cm
R² = 0.14
NRM/ARMOpt.
ARM30 mT (A/m)
D.
Upper 200 cm
R² = 0.51
NRM/IRMOpt.
IRM30 mT (A/m)
E.
Below 200 cm
R² = 0.42
NRM/ARMOpt.
ARM30 mT (A/m)
F.
Below 200 cm
R² = 0.18
R² = 0.50
NRM/IRMOpt.
IRM30 mT (A/m)

Figure 3.8

Figure 3.8 – Normalized remanence results and corresponding R-values for NRM/ARM **(A)** and NRM/IRM **(B)** versus depth, based on the slope method calculations for the "consecutive-range" (solid orange lines) and "optimized" (dashed blue lines) approaches (see text for details). Example 30 mT demagnetization steps for each of the normalizers (ARM and IRM) are provided to assess their resemblance to relative paleointensity (RPI) inferred from the normalized remnance records. Note, these are plotted on a log scale. Locations of A10 section breaks for overlapping (→) and abutted (⇒) sections are shown for reference. Intervals effected by core-top disturbance or rapidly changing magnetic concentration (0-25 cm, 187-226 cm, and 288-304 cm) are shaded pink for reference, and the interval below 550 cm is shaded green, corresponding to sediments with a slight increase in high-coercivity components (see S-Ratios; Fig. 3.3). Dashed-grey boxes correspond to shaded intervals in Figure 3.7. Bi-plots of optimized NRM/ARM versus $NRM_{30\ mT}$ **(C** and **E)** and optimized NRM/IRM versus $IRM_{30\ mT}$ **(D** and **F)** are compared for the both the upper (0-200 cm) and lower (201-651 cm) portions of the record, respectively. R^2 correlation coefficients are given in each case. For RPI to be viable, normalized remnance must not bear any resemblance to their normalizer. Excluding the pink intervals mentioned above, R^2 values demonstrate that the determination of continuous RPI is viable in the top 200 cm of the record, and that ARM is a better normalizer. Strong linear trends preclude us from pursuing RPI estimations in sediments below 200 cm (with the possible exception of sediments below 550 cm). Lithologic variability clearly has not adequately normalized in this portion of the record, with many of the large-amplitude variations in ferrimagnetic concentration still evident in normalized remnance results.

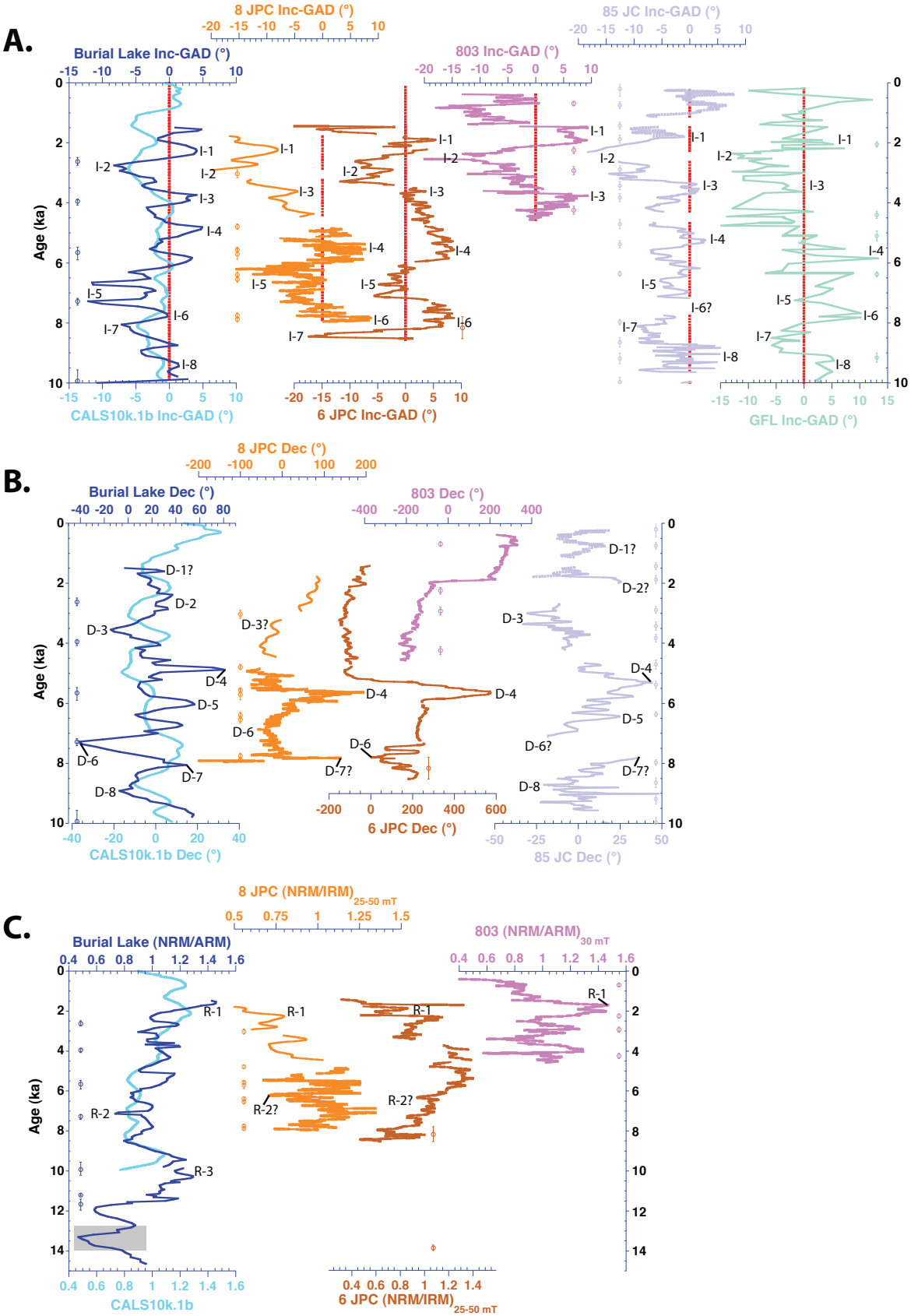
A.
8 JPC Inc-GAD (°)
85 JC Inc-GAD (°)
Burial Lake Inc-GAD (°)
803 Inc-GAD (°)
Age (ka)
CALS10k.1b Inc-GAD (°)
6 JPC Inc-GAD (°)
GFL Inc-GAD (°)
B.
8 JPC Dec (°)
Burial Lake Dec (°)
803 Dec (°)
CALS10k.1b Dec (°)
6 JPC Dec (°)
85 JC Dec (°)
C.
8 JPC (NRM/IRM)25-50 mT
Burial Lake (NRM/ARM)
803 (NRM/ARM)30 mT
CALS10k.1b
6 JPC (NRM/IRM)25-50 mT

Figure 3.9

Figure 3.9 – Full-vector regional comparison of Holocene PSV records the Alaskan Arctic placed on their own chronologies. Inclination (**A**), Declination (**B**), and RPI (**C**) profiles for the Burial Lake record are compared with cores 8 JPC and 6 JPC (Chukchi Sea; Lisé-Pronovost et al., 2009), 803 (Beaufort Sea; Barletta et al., 2008), 85 JC (Gulf of Alaska; Davies et al., *in prep*), and Grandfather Lake (GFL; Southwestern mainland of Alaska; Geiss and Banerjee, 2003). CHSM results from CALS10k.1b (Korte et al., 2011) are also included, explicitly output for the location of Burial Lake. Inclinations are reported as "inclination anomalies", calculated by subtracting the GAD prediction for each site's latitude from the observed inclination, and are shown for the period 10 ka to present, with GAD represented by the vertical red lines at 0°. Declinations are rotated to a mean of 0°, for the period 10 ka to present. RPI is shown for the period 15 ka to present. The interval from ~11.44 to ~13.98 ka is shaded grey for the Burial Lake record, corresponding to high MAD values observed between 170 and 194 cm in Figure 3.7. Correlative features in inclination (I-1 – I-8), declination (D-1 – D-8), and RPI (R-1 – R-3), are identified, some of which are discussed in the text. The radiocarbon chronologies are provided alongside each record, where available, with error bars corresponding to the 2σ age uncertainty.

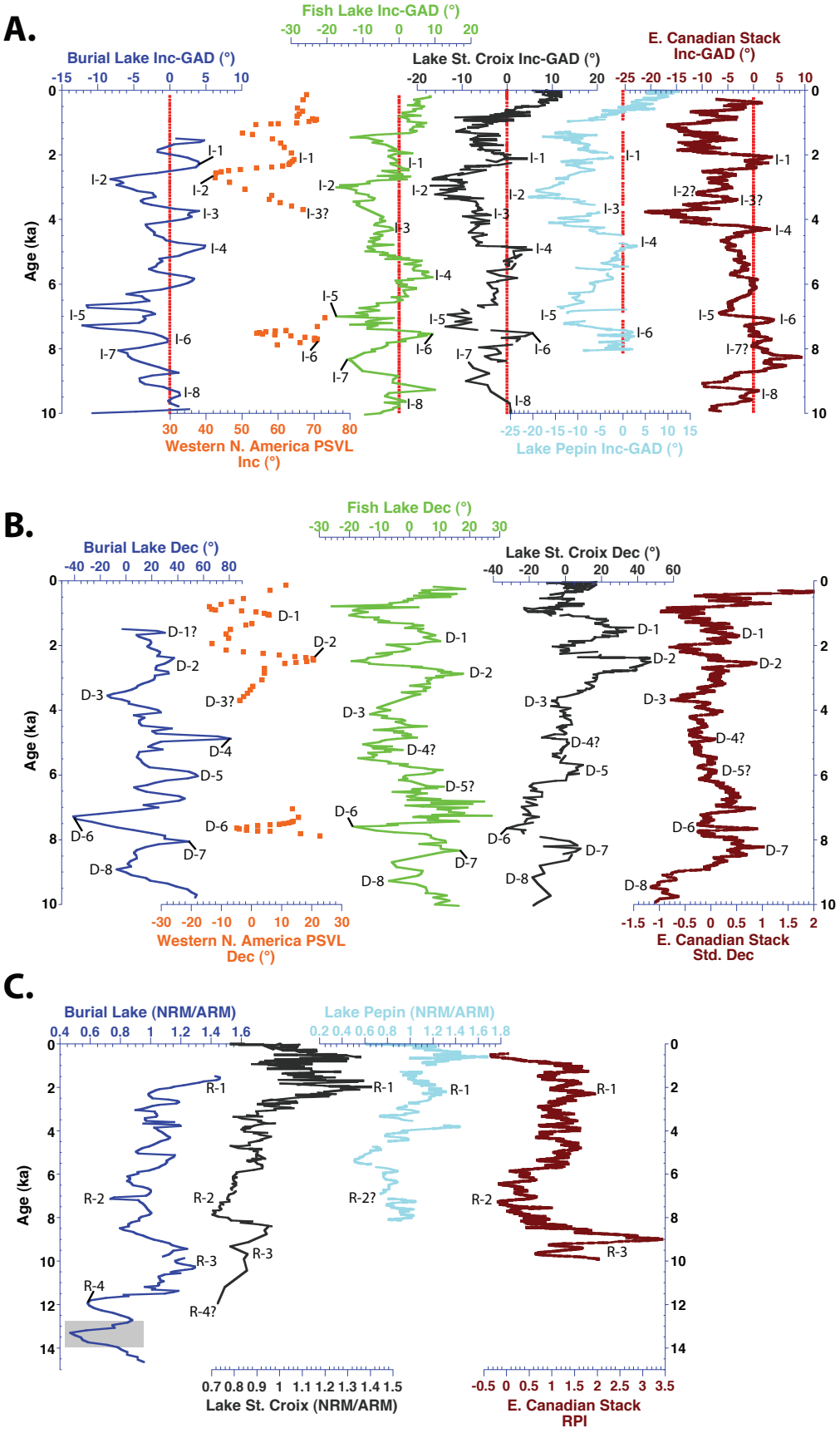
A.
Fish Lake Inc-GAD (°)
Burial Lake Inc-GAD (°)
Lake St. Croix Inc-GAD (°)
E. Canadian Stack Inc-GAD (°)
Age (ka)
Western N. America PSVL Inc (°)
Lake Pepin Inc-GAD (°)
B.
Fish Lake Dec (°)
Burial Lake Dec (°)
Lake St. Croix Dec (°)
Western N. America PSVL Dec (°)
E. Canadian Stack Std. Dec
C.
Burial Lake (NRM/ARM)
Lake Pepin (NRM/ARM)
Lake St. Croix (NRM/ARM)
E. Canadian Stack RPI

Figure 3.10

Figure 3.10 – Full-vector regional comparison of Holocene PSV records North America placed on their own chronologies. Inclination (**A**), Declination (**B**), and RPI (**C**) profiles for the Burial Lake record are compared with PSV derived from lavas in western North America (PSVL; Hagstrum and Champion, 2002), Fish Lake (Oregon; Verosub et al., 1986), Lake St. Croix (Minnesota; Lund and Banerjee, 1985), Lake Pepin (Minnesota; Brachfeld and Banerjee, 2000), and the Eastern Canadian Stack (Laurentian Channel; Barletta et al., 2010). Inclinations are reported as "inclination anomalies", calculated by subtracting the GAD prediction for each site's latitude from the observed inclination, and are shown for the period 10 ka to present, with GAD represented by the vertical red lines at 0°. Declinations are rotated to a mean of 0°, for the period 10 ka to present (except for the Eastern Canadian Stack, which is standardized to a mean of 1). RPI is shown for the period 15 ka to present. The interval from ~11.44 to ~13.98 ka is shaded grey for the Burial Lake record, corresponding to high MAD values observed between 170 and 194 cm in Figure 3.7. Correlative features in inclination (I-1 – I-8), declination (D-1 – D-8), and RPI (R-1 – R-4) are identified, some of which are discussed in the text.

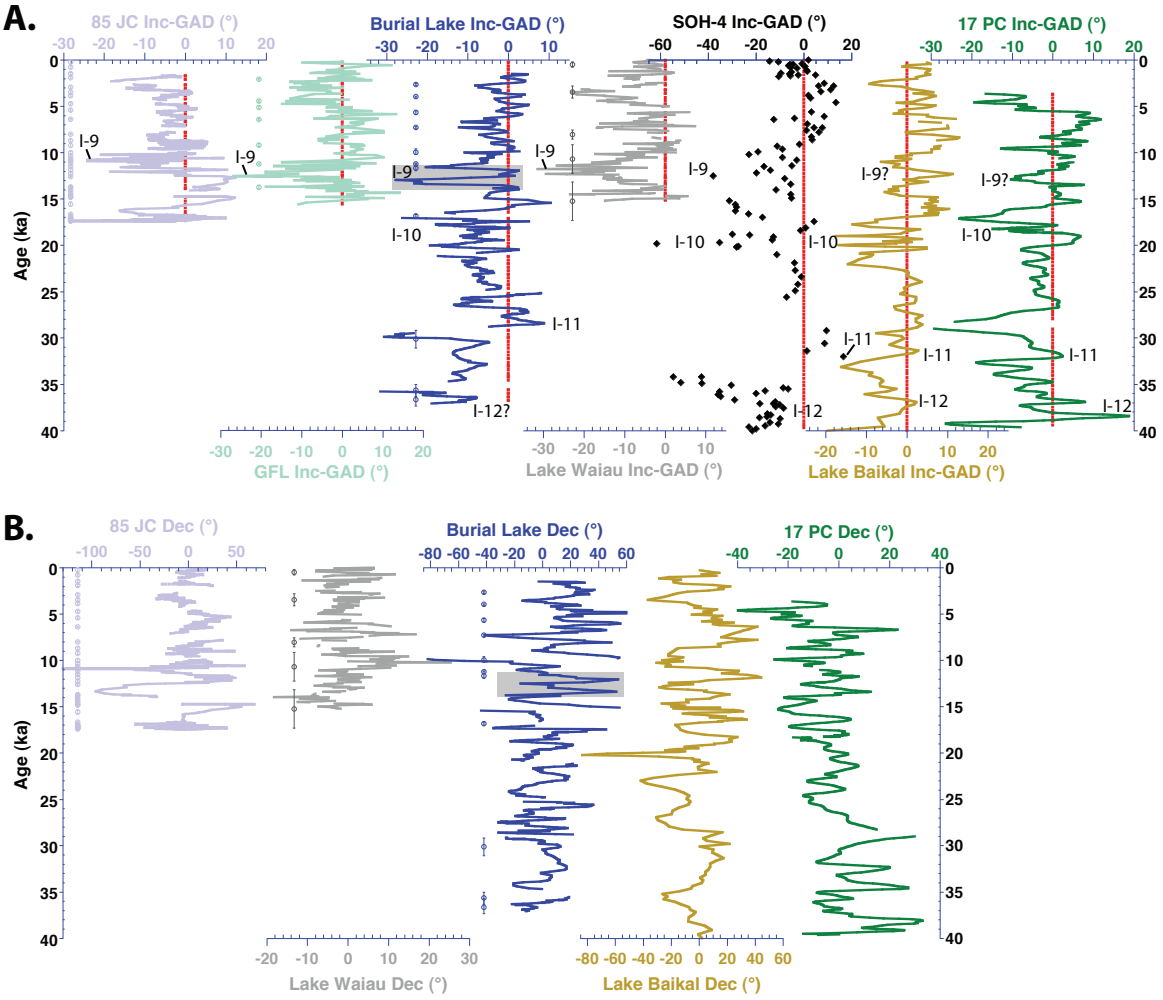

Figure 3.11 – Regional comparison of directional PSV records the Alaskan Arctic and broader high-latitude Pacific placed on their own chronologies for the period 40 ka to present. Inclination (**A**) and Declination (**B**) profiles for the Burial Lake record are compared with extended records from core 85 JC (Gulf of Alaska; Davies et al., *in prep*), and Grandfather Lake (GFL; Southwestern mainland of Alaska; Geiss and Banerjee, 2003), as well as with PSV derived from Lake Waiau (Hawaii; Peng and King, 1992), Hawaiian lava data from the Kilauea volcano (drill core SOH-4; Laj et al., 2002), Lake Baikal (south-central Siberia; Peck et al., 1996), and core 17 PC (Oregon margin; Xuan et al., *in prep*). Inclinations are reported as "inclination anomalies", calculated by subtracting the GAD prediction for each site's latitude from the observed inclination, with GAD represented by the vertical red lines at 0°. Declinations are rotated to a mean of 0°, for the period 10 ka to present. The interval from ~11.44 to ~13.98 ka is shaded grey for the Burial Lake record, corresponding to high MAD values observed between 170 and 194 cm in Figure 3.7. Potential correlative features in inclination (I-9 – I-12) are identified, some of which are discussed in the text. No such features are identified for declination. The radiocarbon chronologies are provided alongside each record, where available, with error bars corresponding to the 2σ age uncertainty. We point out that inclinations mostly vary around GAD for the Holocene (0-10 ka) exhibiting subdued variability, while falling significantly below GAD during the Pleistocene, and exhibiting larger amplitude variations (see text for a discussion of these Holocene-Pleistocene discrepancies).

Table 3.1 – AMS ^{14}C results based on terrestrial macrofossils identified in deep basin cores A10 and C10, which were stratigraphically correlated using physical, geochemical, and magnetics data to produce a common depth scale (see Appendix A). Radiocarbon ages were calibrated using Calib 6.0 (Stuiver et al., 2005) and the IntCal09 calibration curve (Reimer et al., 2009) and are reported with their 2σ uncertainties.

Sample ID (UCIAMS #)	Core-Drive	Drive Depth (cm)	Composite Depth (cm)	Material	Raw Age (^{14}C yr BP)	Error (yr)	Calib Age (yr BP)
89197	A10-D1	45.0	45.0	plant material	2,535	30	2,493 - 2,745
109361	A10-D1	66.5	66.5	wood	3,635	25	3,872 - 4,074
116878	A10-D1	87.5	87.5	plant material	4,910	90	5,470 - 5,896
89198	A10-D1	111.0	111.0	plant material	6,345	25	7,174 - 7,410
109362	A10-D1	141.5	141.5	wood	8,850	110	9,564 - 10,205
89199	A10-D2	84.0	166.0	plant material	9,760	40	11,134 - 11,244
89200	A10-D3	54.0	173.5	seed	10,085	45	11,398 - 11,959
89122	C10-D3	45.0	219.0	wood	13,670	30	16,657 - 16,978
* 109363	A10-D5	35.5	359.5	plant material	14,590	550	16,570 - 18,903
89201	A10-D7	29.0	553.0	seed	25,300	510	29,173 - 31,074
** 89123	C10-D7	64.0	598.0	plant material	31,290	300	35,085 - 36,475
89124	C10-D7	72.0	606.0	wood	31,090	210	35,036 - 36,313
89121	A10-D8	35.5	636.5	wood	32,150	240	35,699 - 37,342

* Sample excluded from age model due to very low carbon yield and presumed modern carbon contamination.

** Sample excluded from age model due to slight age reversal with sample #89124, containing slightly higher carbon yield.

Table 3.2 – Root mean square (RMS) results for various inclination anomaly records presented in this study. RMS is calculated separately for the Holocene (0-10 ka) and Pleistocene (>10 ka) intervals of each record, with higher Pleistocene values indicating a Pleistocene geomagnetic field characterized by increased variability (on average 67.8% more variable than that of the Holocene).

Inclination anomaly record	Holocene (0-10 ka) RMS	Pleistocene (>10 ka) RMS
Burial Lake (this study)	3.91	10.48
8 JPC (Lisé-Pronovost et al., 2009)	5.4	-----
6 JPC (Lisé-Pronovost et al., 2009)	5.9	-----
803 (Barletta et al., 2008)	7.01	-----
85 JC (Davies et al., *in prep*)	5.46	8.2
GFL (Geiss and Banerjee, 2003)	6.29	8.27
Fish Lake (Verosub et al., 1986)	6.39	-----
Lake St. Croix (Lund and Banerjee, 1985)	7.03	-----
Lake Pepin (Brachfeld and Banerjee, 2000)	8.52	-----
E. Canadian Stack (Barletta et al., 2010)	6.45	-----
Lake Waiau (Peng and King, 1992)	9.21	13.7
SOH-4 (Laj et al., 2002)	7.52	22.58
Lake Baikal (Peck et al., 1996)	6.07	6.45
17 PC (Xuan et al., in prep)	7.87	8.46
	Mean = 6.65	**Mean = 11.16**

Chapter 4

General Conclusions and Future Directions

4.1 Thesis Summary

This thesis provides an instructive example of how understanding the magnetic properties of a single sedimentary record can compliment traditional sedimentological methods and shed light on two relatively distinct fields of paleogeology. In this concluding chapter, a summary of the environmental magnetic and paleomagnetic findings is provided, along with a few additional insights that may direct future research.

Through a detailed physical, geochemical, environmental magnetic, and paleomagnetic investigation of Burial Lake sediments, we extend our understanding of paleo-environmental and paleo-geomagnetic variability across the Alaskan Arctic, producing what is currently the oldest continuous lacustrine record in eastern Beringia that spans the last glacial-interglacial cycle. Unlike many records from the Arctic (terrestrial, marine, and lacustrine, combined), which often suffer from difficult chronologies, the Burial Lake record can be well-dated to constrain the climatic and geomagnetic evolution of the region over the last ~37,000 years.

4.2 Environmental Magnetic Conclusions and Future Directions

From a paleo-environmental perspective, the Burial Lake record can be subdivided into three distinct lithologic subunits that correspond to the last glacial period (37.2 – 19.4 ka), the deglacial transition (19.4 – 9.8 ka), and the Holocene (9.8 ka – present), the timing of which are consistent with Northern Hemisphere deglacial climate change (Clark et al., 2009; 2012). Marked declines in CT-density and magnetic concentration through the deglacial transition are accompanied by increases in organic content and biogenic silica. This is consistent with regional proxy data that indicate significant increases in temperature, moisture availability, and terrestrial/aquatic productivity from the glacial period to the Holocene, and are interpreted to partially reflect organic/biogenic dilution of mineralogenic sediment input to Burial Lake.

We model the detrital fraction of Burial Lake sediments as a sum of both low-coercivity and high-coercivity minerals, which can be measured in relative proportion by diagnostic magnetic parameters (e.g., S-Ratios and IRM acquisition/decomposition). The low-coercivity component is interpreted as a magnetite-rich aeolian dust source, whereas the high-coercivity component is interpreted to derive from an ever-present source of locally weathered hematite-rich bedrock.

The overall reduction in aeolian dust observed from the glacial period to the Holocene appears to be forced in part by the ameliorating climatic conditions associated with the deglacial transition, which limited wide-spread landscape deflation and production of dust, which occurred more commonly during the glacial period when regional climate was characterized by much colder, winder and drier conditions, and vegetative cover was less prevalent. The similarity of Burial Lake S-Ratios to regional lake-level reconstructions implies that dust flux is regulated to a large degree by general aridity, and suggests that S-Ratios may be a sensitive indicator to variations in moisture availability, and are potentially capable of reconstructing lake levels throughout the region at a much higher resolution.

We also demonstrate the importance of newly exposed continental shelves as potential far-field sources of dust during the glacial period that were inundated by sea level rise following the LGM, thus leading to the observed reduction in dust flux at Burial Lake and further contributing to the decline in ferrimagnetic concentration. Though late Holocene variations in dust input at Burial Lake are certainly not related to sea level rise (as sea levels had stabilized by ~7 ka), earlier trends in Burial Lake dust flux appear to be more strongly linked to sea level and regional climate variability than to Brooks Range glacier activity, another potential source of dust to Burial Lake. As the Alaskan loess is typically assumed to be glaciogenic in origin, this is a surprising finding, and along with evidence for an otherwise unexplained late Holocene increase in dust flux from ~2 ka, suggests that we consider other potential far-field sources of glacier-derived material (e.g., southeast Alaska).

Given the fact that we have not yet obtained samples of material from the surrounding catchment to ground truth our description of local high-coercivity material, as well as the difficulties involved in magnetically fingerprinting sources of dust (which

are by nature, far removed from the lake itself), our interpretation of the low and high-coercivity sources of sediment to Burial Lake is currently limited to what can be achieved through measurements made on bulk samples from within the lake, compared with previous studies of the Alaskan loess and regional descriptions of Brooks Range bedrock geology. However, we have only just scratched the surface of what can be learned regarding dust transport and sediment sourcing to Burial Lake, and this thesis has opened the door for future dust and paleoclimate-related environmental magnetic studies in Alaska. Future comparison of regional sediment samples from the Burial Lake catchment to various examples of Alaskan loess could allow us to verify the magnetic properties of local versus far-field sources.

We also continue efforts to analyze the magnetic properties of Burial Lake sediments on a particle size-specific basis. Magnetic properties of sediments commonly possess strong particle size-dependence (Oldfield et al., 1985; Oldfield and Yu, 1994; Rosenbaum and Reynolds, 2004; Hatfield and Maher, 2008, 2009; Rosenbaum et al., 2012; Hatfield et al., 2013). Bulk measurements therefore aggregate the magnetic contributions of all clastic size fractions and source lithologies into a single measurement that can be difficult to unravel and interpret in terms of source or transport pathway. The IRM acquisition results presented in this study are an instructive example, and without the use of IRM decomposition techniques, identifying the relative contributions of low-coercivity and high-coercivity components would have been much more tasking. IRM acquisition applied on a particle size-specific basis could verify the coercivity differences between local and far-traveled (aeolian) sources. Intuitively, far-travelled dust should have a very fine grain size, compared to sediments too coarse to be transported by wind, and therefore locally-derived. We would then expect the fine material to contain a low-coercivity magnetic signature, characteristic of magnetite, and the coarse material to contain a higher-coercivity magnetic signature, characteristic of hematite. Furthermore, upon decomposition, we would expect results to be best fit by a single component model, having either a low or high-coercivity depending on the grain size of the sample measured.

While this approach has not yet been tested, grain size-specific hysteresis experiments made on the Princeton Measurements Corporation™ MicroMag model 3900

VSM at Western Washington University, reveal that Burial Lake sediments do in fact display strong particle size-dependent properties, which may have important implications for understanding the Alaskan loess. Hysteresis properties measured on sieved physical grain size separates (Fig. 4.1) show a clear discrepancy between physical and magnetic grain size. Using hysteresis data from the more reliable glacial-age sediments (i.e., Subunit 1), which are composed dominantly of magnetite and therefore should be accurately represented on a plot of Mrs/Ms versus Hcr/Hc (according to Day et al., 1977), we show that the finest magnetic grains are comprised within the coarsest (>63 μm) physical size fraction and the coarsest magnetic grains are comprised within the finest (<20 μm) physical size fraction. As expected, the bulk sample data point lies closest to the <20 μm sample data point, since this fine grained material comprises the majority of the bulk sample. This inverse relationship is consistent throughout all other measured samples from the glacial period. Whereas this trend exists to some degree for samples from the deglacial transition and Holocene (i.e., Subunits 2 and 3), it is not as clearly defined, likely due to changing mineralogy, and compounded by noisy hysteresis measurements on weaker samples and the influence of biogenic components (i.e., diatoms) on physical grain size determinations. Nonetheless, this shows that while magnetic measurements add an extra dimension to interpretation, they cannot strictly be used as a traditional sedimentological proxy. This provides cautionary evidence that care must be taken if the magnetic characteristics of the Alaskan loess are used to infer certain physical environmental processes, for instance wind intensity or other sediment transport regimes.

4.3 Paleomagnetic Conclusions and Future Directions

Given our thorough investigation of Burial Lake lithology, we are better able to characterize the magnetic mineral assemblage serving as the paleomagnetic recorder, and comprehend the effect that variable lithology may have on the resultant paleomagnetic record. Recognizing the decrease in ferrimagnetic concentration that occurs through the deglacial transition, and the resulting high-coercivity nature of Holocene sediments, we use optimized methods for calculating component directions and RPI that isolate the component of the NRM, which is carried by the more reliable low-coercivity magnetic

minerals, which are consistent with (titano)magnetite in the PSD-MD magnetic grain size range.

We obtain a record of directional PSV for the entirety of the Burial Lake record (~37,000 ka), with continuous, reliable RPI reconstructed for the last ~14,700 ka, both of which, are consistent with regional records of PSV in the Alaskan Arctic and North America, as well as with spherical harmonic predictions. Aware of the potential age-offset between the sediment and the magnetization and potential smoothing that may result from a post-depositional "lock-in" effect, the well-constrained chronology of the Burial Lake record allows us to more accurately estimate the ages of particular correlative geomagnetic features throughout the region. In doing so, we provide an independently dated template that can be further developed as a regional stratigraphic dating tool. Although few long records exist for regional comparison beyond the Holocene, the Burial Lake record appears similar in character to PSV recorded at far-field sites (e.g., Hawaii and Siberia), suggesting a somewhat coherent geomagnetic field across the broader high-latitude Pacific. We interpret this behavior to reflect large-scale coherent core-fluid dynamic regimes, which appear consistent over glacial-interglacial time scales. Throughout these comparisons, inclination, rather than declination, appears to be a more sensitive indicator of regional field variability, perhaps related to the location of Burial Lake relative to areas of concentrated flux (i.e., flux lobes) emitted from the outer core.

The uncommon length of the Burial Lake directional record allows us to comment on regional differences between Holocene and Pleistocene field variability. Two major discrepancies are observed. First, component inclinations vary around GAD predictions during the Holocene, but lay significantly shallower than GAD prior to 10 ka, during the Pleistocene. Second, while inclinations exhibit only small deviations from GAD predictions during the Holocene, much larger amplitude features are prevalent during the Pleistocene. These observations hold true for other extended records of inclination, including data from lava flows, and therefore cannot strictly be related to lithology and the sediment magnetic acquisition process. As an estimate of field variability, we calculate RMS values in each record, demonstrating that Pleistocene inclination anomalies are on average ~68% more variable than those in the Holocene. Following on

the "eccentric dipole" hypothesis, we suggest that subdued secular variation and GAD-like behavior in the Pacific during the Holocene is a product of higher geomagnetic intensities and/or the offset of the dipole axis towards the Pacific hemisphere. Comparatively, increased Pleistocene variability is perhaps related to lower overall intensities and/or a shift of the dipole axis to the east.

Future efforts to refine the Burial Lake paleomagnetic record will involve incorporating paleomagnetic results from core C10 (and perhaps D10, if a proper absolute or tuned chronology can be established) to create a composite record of PSV. The addition of this data will help to constrain PSV in the intervals of the A10 record that are affected by core disturbance or masked due to u-channel edge effects. Furthermore, if we choose to average overlapping intervals between the three records to create a composite "stack", uncertainty can be estimated for component directions and RPI.

Lastly, we hope to take a more quantitative approach towards investigating how the Burial Lake record compares with other regional records of PSV through more rigorous analysis in both the time and frequency domains. The simplest of tests would be to perform linear regressions and calculate correlation coefficients between the Holocene portions of the records, where geomagnetic features are more clearly defined within the Alaskan Arctic and North American regions. Another approach may be to use cross-spectral analysis to estimate the degree of coherence between records. Spectral techniques will prove particularly valuable for addressing the frequency content of the longer records in the broader high-latitude Pacific over the last 40 ka. While we may not expect the geomagnetic field to vary coevally between widely spaced sites over this entire time frame, a wavelet analysis may highlight intervals of coherent behavior, and shed light on the spectral power of the records.

4.4 References

Clark, P.U., Dyke, A.S., Shakun, J.D., Carlson, A.E., Clark, J., Wohlfarth, B., Mitrovica, J.X., Hostetler, S.W., McCabe, A.M., 2009. The Last Glacial Maximum. Science 325, 710–714.

Clark, P.U., Shakun, J.D., Baker, P.A., Bartlein, P.J., Brewer, S., Brook, E., Carlson, A.E., Cheng, H., Kaufman, D.S., Liu, Z., Marchitto, T.M., Mix, A.C., Morrill, C., Otto-Bliesner, B.L., Pahnke, K., Russell, J.M., Whitlock, C., Adkins, J.F., Blois, J.L.,

Clark, J., Colman, S.M., Curry, W.B., Flower, B.P., He, F., Johnson, T.C., Lynch-Stieglitz, J., Markgraf, V., McManus, J., Mitrovica, J.X., Moreno, P.I., Williams, J.W., 2012. Global climate evolution during the last deglaciation. Proceedings of the National Academy of Sciences.

Day, R., Fuller, M., Schmidt, V., 1977. Hysteresis properties of titanomagnetites: grain-size and compositional dependence. Physics of the Earth and Planetary Interiors 13, 260–267.

Hatfield, R.G., Maher, B.A., 2008. Suspended sediment characterization and tracing using a magnetic fingerprinting technique: Bassenthwaite Lake, Cumbria, UK. The Holocene 18, 105–115.

Hatfield, R.G., Maher, B.A., 2009. Fingerprinting upland sediment sources: particle size-specific magnetic linkages between soils, lake sediments and suspended sediments. Earth surface processes and landforms 34, 1359–1373.

Hatfield, R.G., Stoner, J.S., Carlson, A.E., Reyes, A.V., Housen, B.A., 2013. Source as a controlling factor on the quality and interpretation of sediment magnetic records from the northern North Atlantic. Earth and Planetary Science Letters 368, 69–77.

Oldfield, F., Maher, B., Donoghue, J., Pierce, J., 1985. Particle-size related, mineral magnetic source sediment linkages in the Rhode River catchment, Maryland, USA. Journal of the Geological Society 142, 1035–1046.

Oldfield, F., Yu, L., 1994. The influence of particle size variations on the magnetic properties of sediments from the north-eastern Irish Sea. Sedimentology 41, 1093–1108.

Rosenbaum, J.G., Reynolds, R.L., 2004. Basis for paleoenvironmental interpretation of magnetic properties of sediment from Upper Klamath Lake (Oregon): effects of weathering and mineralogical sorting. Journal of Paleolimnology 31, 253–265.

Rosenbaum, J.G., Reynolds, R.L., Colman, S.M., 2012. Fingerprinting of glacial silt in lake sediments yields continuous records of alpine glaciation (35 15ka), western USA. Quaternary Research.

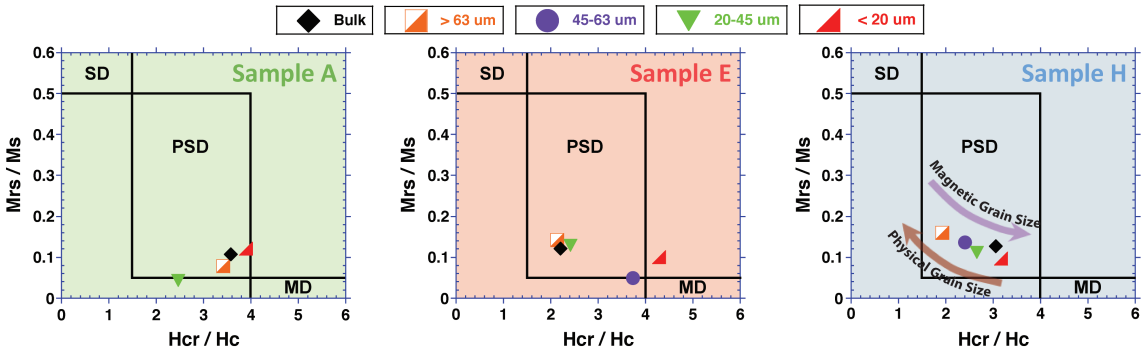

Figure 4.1 – Particle size-specific hysteresis results for representative samples in Subunit 3 (A: 40 cm, 2.331 ka), Subunit 2 (E: 190 cm, 13.526 ka), and Subunit 1 (H: 474 cm, 26.965 ka), corresponding to the Holocene, deglacial transition, and last glacial period, respectively. Ratios of Mrs/Ms and Hcr/Hc, are plotted within theoretical domain state (magnetic grain size) boundaries, drawn according to the behavior of pure magnetite (Day et al., 1977). Bulk sample results are shown along with those for sieved physical grain size separates (>63, 45-63, 20-45, and <20 μm), demonstrating the discrepancy between physical and magnetic grain size wherein the finest magnetic grains are often contained within the coarsest grain size fraction, and vice versa. Sample H from the glacial period, shows this inverse relationship most clearly, where the data are to be most trusted due to the higher concentrations of low-coercivity minerals (i.e., magnetite), and relative lack of biogenic components (i.e., diatoms).

BIBLIOGRAPHY

Abbott, M.B., Edwards, M.E., Finney, B.P., 2010. A 40,000-yr record of environmental change from Burial Lake in Northwest Alaska. Quaternary Research 74, 156–165.

Abbott, M.B., Finney, B.P., Edwards, M.E., Kelts, K.R., 2000. Lake-Level Reconstruction and Paleohydrology of Birch Lake, Central Alaska, Based on Seismic Reflection Profiles and Core Transects. Quaternary Research 53, 154–166.

Ager, T.A., 1975. Late quaternary environmental history of the Tanana Valley, Alaska. Research Foundation and the Institute of Polar Studies, The Ohio State University, Columbus, Ohio.

Amit, H., Aubert, J., Hulot, Gauthier, 2010. Stationary, oscillating or drifting mantle-driven geomagnetic flux patches? Journal of Geophysical Research: Solid Earth (1978–2012) 115.

Anderson, N., Rippey, B., 1988. Diagenesis of magnetic minerals in the recent sediments of a eutrophic lake. Limnology and Oceanography 1476–1492.

Andrews, J.T., Jennings, A.E., 1990. Geomagnetic secular variations (inclination) of high latitude fiord cores: eastern Canadian Arctic*. Polar Research 8, 245–259.

Aurnou, J., Andreadis, S., Zhu, L., Olson, P., 2003. Experiments on convection in Earth's core tangent cylinder. Earth and Planetary Science Letters 212, 119–134.

Backus, G.E., 1968. Kinematics of geomagnetic secular variation in a perfectly conducting core. Philosophical Transactions of the Royal Society of London. Series A, Mathematical and Physical Sciences 263, 239–266.

Badding, M.E., Briner, J.P., Kaufman, D.S., 2013. 10Be ages of late Pleistocene deglaciation and Neoglaciation in the north-central Brooks Range, Arctic Alaska. J. Quaternary Sci. 28, 95–102.

Barclay, D.J., Wiles, G.C., Calkin, P.E., 2009. Holocene glacier fluctuations in Alaska. Quaternary Science Reviews 28, 2034–2048.

Barletta, F., St-Onge, G, Stoner, J., Lajeunesse, P., Locat, J., 2010. A high-resolution Holocene paleomagnetic secular variation and relative paleointensity stack from eastern Canada. Earth and Planetary Science Letters 298, 162–174.

Barletta, F., St-Onge, G., Channell, J.E., Rochon, A., Polyak, L., Darby, D., 2008. High-resolution paleomagnetic secular variation and relative paleointensity records from

the western Canadian Arctic: implication for Holocene stratigraphy and geomagnetic field behaviour. Canadian Journal of Earth Sciences 45, 1265–1281.

Begét, J.E., 1990. Middle Wisconsinan Climate Fluctuations Recorded in Central Alaskan Loess. Géographie physique et Quaternaire 44, 3–13.

Begét, J.E., 2001. Continuous Late Quaternary proxy climate records from loess in Beringia. Quaternary Science Reviews 20, 499–507.

Begét, J.E., Stone, D.B., Hawkins, D.B., 1990. Paleoclimatic forcing of magnetic susceptibility variations in Alaskan loess during the late Quaternary. Geology 18, 40–43.

Berger, A., Loutre, M.F., 1991. Insolation values for the climate of the last 10 million years. Quaternary Science Reviews 10, 297–317.

Bigelow, N., Begét, J., Powers, R., 1990. Latest Pleistocene increase in wind intensity recorded in eolian sediments from central Alaska. Quaternary Research 34, 160–168.

Bigelow, N.H., 1997. Late-Quaternary climate and vegetation in interior Alaska. University of Alaska, Fairbanks, Fairbanks, AK.

Bigelow, N.H., Edwards, M.E., 2001. A 14,000 yr paleoenvironmental record from Windmill Lake, Central Alaska: Lateglacial and Holocene vegetation in the Alaska range. Quaternary Science Reviews 20, 203–215.

Bird, B., Abbott, M., Finney, B., Kutchko, B., 2009. A 2000 year varve-based climate record from the central Brooks Range, Alaska. J Paleolimnol 41, 25–41.

Blaauw, M., 2010. Methods and code for "classical" age-modelling of radiocarbon sequences. Quaternary Geochronology 5, 512–518.

Blott, S.J., Pye, K., 2001. GRADISTAT: a grain size distribution and statistics package for the analysis of unconsolidated sediments. Earth Surf. Process. Landforms 26, 1237–1248.

Bloxham, J., Gubbins, D., 1985. The secular variation of Earth's magnetic field. Nature 317, 777–781.

Bloxham, J., Jackson, A., 1991. Fluid flow near the surface of Earth's outer core. Rev. Geophys. 29, 97–120.

Brachfeld, S.A., Banerjee, S.K., 2000. A new high-resolution geomagnetic relative paleointensity record for the North American Holocene: A comparison of sedimentary and absolute intensity data. Journal of Geophysical Research: Solid Earth (1978–2012) 105, 821–834.

Bradley, R.S., 1999. Paleoclimatology: reconstructing climates of the Quaternary. Academic Press.

Briner, J.P., Kaufman, D.S., 2008. Late Pleistocene mountain glaciation in Alaska: key chronologies. J. Quaternary Sci. 23, 659–670.

Broecker, W.S., 1994. Massive iceberg discharges as triggers for global climate change. Nature 372, 421–424.

Butler, R.F., 1984. Paleomagnetism: Magnetic domains to geologic terranes. Originally published by Blackwell in. C. S. G. Gogorza, A. M. Sinito, J. F. Vilas, K. M. Creer, H. Nuñez, 2002. Geomagnetic secular variations over the last 6500 years as recorded by sediments from the lakes of south Argentina. Geophys J 143, 787–798.

Cande, S.C., Kent, D.V., 1995. Revised calibration of the geomagnetic polarity timescale for the Late Cretaceous and Cenozoic. J. Geophys. Res. 100, 6093–6095.

Carlson, L.J., Finney, B.P., 2004. A 13 000-year history of vegetation and environmental change at Jan Lake, east-central Alaska. Holocene 14, 818–827.

Chulliat, A., Thébault, E., Hulot, G., 2010. Core field acceleration pulse as a common cause of the 2003 and 2007 geomagnetic jerks. Geophys. Res. Lett. 37, L07301.

Clark, P.U., Dyke, A.S., Shakun, J.D., Carlson, A.E., Clark, J., Wohlfarth, B., Mitrovica, J.X., Hostetler, S.W., McCabe, A.M., 2009. The Last Glacial Maximum. Science 325, 710–714.

Clark, P.U., Shakun, J.D., Baker, P.A., Bartlein, P.J., Brewer, S., Brook, E., Carlson, A.E., Cheng, H., Kaufman, D.S., Liu, Z., Marchitto, T.M., Mix, A.C., Morrill, C., Otto-Bliesner, B.L., Pahnke, K., Russell, J.M., Whitlock, C., Adkins, J.F., Blois, J.L., Clark, J., Colman, S.M., Curry, W.B., Flower, B.P., He, F., Johnson, T.C., Lynch-Stieglitz, J., Markgraf, V., McManus, J., Mitrovica, J.X., Moreno, P.I., Williams, J.W., 2012. Global climate evolution during the last deglaciation. Proceedings of the National Academy of Sciences.

Cox, A., 1970. Latitude dependence of the angular dispersion of the geomagnetic field. Geophysical Journal of the Royal Astronomical Society 20, 253–269.

Creer, K.M., Tucholka, P., 1982. Construction of type curves of geomagnetic secular variation for dating lake sediments from east central North America. Can. J. Earth Sci. 19, 1106–1115.

Davies, M.H., Mix, A.C., Stoner, J.S., Addison, J.A., Jaeger, J., Finney, B., Wiest, J., 2011. The deglacial transition on the southeastern Alaska Margin: Meltwater input, sea level rise, marine productivity, and sedimentary anoxia. Paleoceanography 26, PA2223.

Davies, M.H., Stoner, J., Mix, A.C., Southon, J., Jaeger, J., Rosen, G.P., Channell, J.E., (*in prep*). Reconstruction Holocene paleomagnetic secular variation from the Gulf of Alaska.

Day, R., Fuller, M., Schmidt, V., 1977. Hysteresis properties of titanomagnetites: grain-size and compositional dependence. Physics of the Earth and Planetary Interiors 13, 260–267.

Dekkers, M.J., 1997. Environmental magnetism: an introduction. Geologie en Mijnbouw 76, 163–182.

Doell, R.R., Cox, A., 1972. The Pacific geomagnetic secular variation anomaly and the question of lateral uniformity in the lower mantle. The nature of the solid earth 245–284.

Dorfman, J.M., Stoner, J.S., Finkenbinder, M.S., Abbott, M.B., Xuan, C., St-Onge, G. (*In prep*). Timing and extent of aeolian dust deposition: A 37,000-year record of environmental magnetic variability from Burial Lake, Arctic Alaska.

Dunlop, D.J., Özdemir, Ö., 2001. Rock magnetism: fundamentals and frontiers. Cambridge University Press.

Eisner, W.R., Colinvaux, P.A., 1992. Late Quaternary pollen records from Oil Lake and Feniak Lake, Alaska, USA. Arctic and Alpine Research 56–63.

Elias, S.A., Hamilton, T.D., Edwards, M.E., Begét, J.E., Krumhardt, A.P., Lavoie, C., 1999. Late Pleistocene environments of the western Noatak basin, northwestern Alaska. Bull Geol Soc Am 111, 769–789.

Elias, S.A., Short, S.K., Birks, H.H., 1997. Late Wisconsin environments of the Bering Land Bridge. Palaeogeography, Palaeoclimatology, Palaeoecology 136, 293–308.

Ellersieck, I., Curtis, S.M., Mayfield, C.F., and Tailleur, I.L., 1984, Reconnaissance geologic map of south-central Misheguk Mountain Quadrangle, Alaska: U.S. Geological Survey Miscellaneous Investigations Series Map 1504, 2 sheets, scale 1:63,360.

Ellis, J.M., Calkin, P.E., 1984. Chronology of Holocene glaciation, central Brooks Range, Alaska. Geological Society of America Bulletin 95, 897–912.

Evans, M.E., Jensen, B.J.L., Kravchinsky, V.A., Froese, D.G., 2011. The Kamikatsura event in the Gold Hill loess, Alaska. Geophys. Res. Lett. 38, L13302.

Evans, M.M.E., Heller, F.A., 2003. Environmental magnetism: International geophysics series. Academic Press, Incorporated.

Farrians, O., J., 1965. Permafrost map of Alaska: U.S. Geological Survey Miscellaneous Geologic Investigations Map I-445.

Finkenbinder, M.S., Abbott, M.B., Stoner, J.S., Dorfman, J.M., (*in prep*), A multi-proxy geochemical investigation of late-Quaternary paleoenvironmental change from Burial Lake, Noatak National Preserve, Alaska.

Frank, U., Nowaczyk, N.R, Negendank, J., Melles, M, 2002. A paleomagnetic record from Lake Lama, northern Central Siberia. Physics of the Earth and Planetary Interiors 133, 3–20.

Frank, U., Nowaczyk, N.R., 2008. Mineral magnetic properties of artificial samples systematically mixed from haematite and magnetite. Geophysical Journal International 175, 449–461.

Gallet, Y., Hulot, Gauthier, Chulliat, Arnaud, Genevey, Agnès, 2009. Geomagnetic field hemispheric asymmetry and archeomagnetic jerks. Earth and Planetary Science Letters 284, 179–186.

Geiss, C., Banerjee, S., 2003. A Holocene—Late Pleistocene geomagnetic inclination record from Grandfather Lake, SW Alaska. Geophysical Journal International 153, 497–507.

Gubbins, D., Gibbons, S.J., 2004. Low Pacific secular variation. Timescales of the Paleomagnetic Field, Geophys. Monogr. Ser 145, 279–286.

Guyodo, Y., Valet, J.-P., 1996. Relative variations in geomagnetic intensity from sedimentary records: the past 200,000 years. Earth and Planetary Science Letters 143, 23–36.

Hagstrum, J.T., Champion, D.E., 2002. A Holocene paleosecular variation record from 14C-dated volcanic rocks in western North America. Journal of Geophysical Research: Solid Earth (1978–2012) 107, EPM–8.

Hamilton, T.D., 1982. A late Pleistocene glacial chronology for the southern Brooks Range: Stratigraphic record and regional significance. Geological Society of America Bulletin 93, 700–716.

Hamilton, T.D., 1994, Late Cenozoic glaciation of Alaska, in Plafker, George, and Berg, H.C., The Geology of Alaska: Geological Society of America, p. 813-844.

Hamilton, T.D., 2001. Quaternary glacial, lacustrine, and fluvial interactions in the western Noatak basin, Northwest Alaska. Quaternary Science Reviews 20, 371–391.

Hamilton, T.D., 2003. Surficial geology of the Dalton Highway (Itkillik-Sagavanirktok Rivers) area, southern Arctic foothills, Alaska. Alaska Dept. of Natural Resources, Division of Geological and Geophysical Surveys, [Fairbanks, Alaska].

Hamilton, T.D., 2009, Guide to surficial geology and river-bluff exposures, Noatak National Preserve, northwestern Alaska: U.S. Geological Survey Scientific Investigations Report 2008-5125, 116 p. [http://pubs.usgs.gov/sir/2008/5125/].

Hamilton, T.D., 2010, Surficial geologic map of the Noatak National Preserve, Alaska: U.S. Geological Survey Scientific Investigations Map 3036, 1 sheet, scale 1:250,000, 1 pamphlet, 21 p.

Hamilton, T.D., and Labay, K.A., 2011, Surficial geologic map of the Gates of the Arctic National Park and Preserve, Alaska: U.S. Geological Survey Scientific Investigations Map 3125, pamphlet 19 p., scale 1:300,000, available at http://pubs.usgs.gov/sim/3125/.

Hamilton, T.D., Van Etten, D.P., 1984. Late Pleistocene glacial dams in the Noatak valley. In: Conrad, W.L., Elliott, R.L. (Eds.), The United States Geological Survey in Alaska: Accomplishments During 1981. U.S. Geol. Survey Circular 868, pp. 21-23.

Hayashida, A., Ali, M., Kuniko, Y., Kitagawa, H., Torii, M., Takemura, K., 2007. Environmental magnetic record and paleosecular variation data for the last 40 kyrs from the Lake Biwa sediments, Central Japan. Earth, Planets, and Space 59, 807–814.

Heslop, D., Dekkers, M.J., Kruiver, P.P., Van Oorschot, I.H.M., 2002. Analysis of isothermal remanent magnetization acquisition curves using the expectation–maximization algorithm. Geophysical Journal International 148, 58–64.

Hillaire-Marcel, C., 2008. Decadal-to millennial-scale variability of Arctic-Subarctic oceans and adjacent lands: a contribution of the Polar Climate Stability Network of Canada to the International Polar Year. Canadian Journal of Earth Sciences 45, 1199–1201.

Hopkins, D.M., 1982. Aspects of the paleogeography of Beringia during the late Pleistocene. Paleoecology of Beringia. Academic Press, New York 3–28.

Hostetler, S.W., Clark, P.U., Bartlein, P.J., Mix, A.C., Pisias, N.J., 1999. Atmospheric transmission of North Atlantic Heinrich events. J. Geophys. Res. 104, 3947–3952.

Hulot, G., Eymin, C., Langlais, B., Mandea, M., Olsen, N., 2002. Small-scale structure of the geodynamo inferred from Oersted and Magsat satellite data. Nature 416, 620–623.

Hulot, G., Finlay, C., Constable, C., Olsen, N., Mandea, M., 2010. The magnetic field of planet Earth. Space science reviews 152, 159–222.

Hutchins, D.A., Bruland, K.W., 1998. Iron-limited diatom growth and Si:N uptake ratios in a coastal upwelling regime. Nature 393, 561–564.

Huybers, P., Wunsch, C., 2004. A depth-derived Pleistocene age model: Uncertainty estimates, sedimentation variability, and nonlinear climate change. Paleoceanography 19, PA1028.

Imbrie, J., Northwestern University (Evanston, I.), Research, U.S.O. of N., 1963. Factor and Vector Analysis Programs for Analyzing Geologic Data. Northwestern University.

Irving, E., Major, A., 1964. Post-Depositional Detrital Remanent Magnetization in a Synthetic Sediment. Sedimentology 3, 135–143.

Jackson, A., Jonkers, A.R.T., Walker, M.R., 2000. Four centuries of geomagnetic secular variation from historical records. Philosophical Transactions of the Royal Society of London. Series A: Mathematical, Physical and Engineering Sciences 358, 957–990.

Karlin, R., and Levi, S., 1983. Diagenesis of magnetic minerals in recent hemipelagic sediments. Nature 303: 327-330.

King, J.W., and Channel, J.E.T., 1991, Sedimentary magnetism, environmental magnetism, and magnetostratigraphy: Reviews of Geophysics, Supplement, p. 358-370.

King, J.W., Banerjee, S.K., Marvin, J., 1983. A new rock-magnetic approach to selecting sediments for geomagnetic paleointensity studies: Application to paleointensity for the last 4000 years. Journal of Geophysical Research: Solid Earth (1978–2012) 88, 5911–5921.

Kirschvink, J., 1980. The least-squares line and plane and the analysis of palaeomagnetic data. Geophysical Journal International 62, 699–718.

Knudsen, M.F., Riisager, P., Donadini, Fabio, Snowball, I., Muscheler, R., Korhonen, K., Pesonen, L.J., 2008. Variations in the geomagnetic dipole moment during the Holocene and the past 50 kyr. Earth and Planetary Science Letters 272, 319–329.

Kohfeld, K.E., Harrison, S.P., 2001. DIRTMAP: the geological record of dust. Earth-Science Reviews 54, 81–114.

Korte, M, Donadini, F, Constable, CG, 2009. Geomagnetic field for 0–3 ka: 2. A new series of time-varying global models. Geochemistry, Geophysics, Geosystems 10.

Korte, M, Genevey, A, Constable, CG, Frank, U., Schnepp, E., 2005. Continuous geomagnetic field models for the past 7 millennia: 1. A new global data compilation. Geochemistry, Geophysics, Geosystems 6.

Korte, Monika, Constable, Catherine, 2003. Continuous global geomagnetic field models for the past 3000 years. Physics of the Earth and Planetary Interiors 140, 73–89.

Korte, Monika, Constable, Catherine, 2011. Improving geomagnetic field reconstructions for 0–3ka. Physics of the Earth and Planetary Interiors 188, 247–259.

Korte, Monika, Constable, Catherine, Donadini, Fabio, Holme, R., 2011. Reconstructing the Holocene geomagnetic field. Earth and Planetary Science Letters 312, 497–505.

Kurek, J., Cwynar, L.C., Ager, T.A., Abbott, M.B., Edwards, M.E., 2009. Late Quaternary paleoclimate of western Alaska inferred from fossil chironomids and its relation to vegetation histories. Quaternary Science Reviews 28, 799–811.

Lagroix, F., Banerjee, S.K., 2002. Paleowind directions from the magnetic fabric of loess profiles in central Alaska. Earth and Planetary Science Letters 195, 99–112.

Laj, Carlo, Kissel, Catherine, Beer, J., 2004. High resolution global paleointensity stack since 75 kyr (GLOPIS-75) calibrated to absolute values. Timescales of the Paleomagnetic Field, Geophys. Monogr. Ser 145, 255–265.

Laj, Carlo, Kissel, Catherine, Scao, V., Beer, J., Thomas, D.M., Guillou, H., Muscheler, R., Wagner, G., 2002. Geomagnetic intensity and inclination variations at Hawaii for the past 98kyr from core SOH-4 (Big Island): a new study and a comparison with existing contemporary data. Physics of the Earth and Planetary Interiors 129, 205–243.

Larsen, C.F., Motyka, R.J., Freymueller, J.T., Echelmeyer, K.A., Ivins, E.R., 2005. Rapid viscoelastic uplift in southeast Alaska caused by post-Little Ice Age glacial retreat. Earth and Planetary Science Letters 237, 548–560.

Le Mouël, J.L., 1984. Outer-core geostrophic flow and secular variation of Earth's geomagnetic field. Nature 311, 734–735.

Lisé-Pronovost, A., St-Onge, G., Brachfeld, S., Barletta, Francesco, Darby, D., 2009. Paleomagnetic constraints on the Holocene stratigraphy of the Arctic Alaskan margin. Global and Planetary Change 68, 85–99.

Liu, X.M., Hesse, P., Rolph, T., Begét, J.E., 1999. Properties of magnetic mineralogy of Alaskan loess: evidence for pedogenesis. Quaternary International 62, 93–102.

Lohmann, K.J., Putman, N.F., Lohmann, C.M., 2012. The magnetic map of hatchling loggerhead sea turtles. Current Opinion in Neurobiology 22, 336–342.

Lowrie, W., 1990. Identification of ferromagnetic minerals in a rock by coercivity and unblocking temperature properties. Geophys. Res. Lett. 17, 159–162.

Lund, S.P., 1996. A comparison of Holocene paleomagnetic secular variation records from North America. J. Geophys. Res. 101, 8007–8024.

Lund, S.P., Banerjee, S.K., 1985. Late Quaternary paleomagnetic field secular variation from two Minnesota Lakes. J. Geophys. Res. 90, 803–825.

Marcott, S.A., Shakun, J.D., Clark, P.U., Mix, A.C., 2013. A Reconstruction of Regional and Global Temperature for the Past 11,300 Years. Science 339, 1198–1201.

Mayfield, C.F., Curtis, S.M., Ellersieck, I., and Tailleur, I.L., 1984, Reconnaissance geologic map of southeastern Misheguk Mountain Quadrangle, Alaska: U.S. Geological Survey Miscellaneous Investigations Series Map 1503, 2 sheets, scale 1:63,360.

Merrill, R.T., McElhinny, M.W., McFadden, P.L., 1998. The magnetic field of the earth: paleomagnetism, the core, and the deep mantle. Academic Press.

Mikolajewicz, U., Crowley, T.J., Schiller, A., Voss, R., 1997. Modelling teleconnections between the North Atlantic and North Pacific during the Younger Dryas. Nature 387, 384–387.

Muhs, D.R., Ager, T.A., Arthur Bettis III, E., McGeehin, J., Been, J.M., Begét, J.E., Pavich, M.J., Stafford Jr., T.W., Stevens, D.A.S.P., 2003a. Stratigraphy and palaeoclimatic significance of Late Quaternary loess–palaeosol sequences of the Last Interglacial–Glacial cycle in central Alaska. Quaternary Science Reviews 22, 1947–1986.

Muhs, D.R., Ager, T.A., Been, J., Bradbury, J.P., Dean, W.E., July 2003b. A late quaternary record of eolian silt deposition in a maar lake, St. Michael Island, western Alaska. Quaternary Research 60, 110–122.

Muhs, D.R., Budahn, J.R., 2006. Geochemical evidence for the origin of late Quaternary loess in central Alaska. Can. J. Earth Sci. 43, 323–337.

North Greenland Ice Core Project members, 2004. High-resolution record of Northern Hemisphere climate extending into the last interglacial period. Nature 431, 147–151.

Nowaczyk, N.R., Harwart, S., Melles, Martin, 2001. Impact of early diagenesis and bulk particle grain size distribution on estimates of relative geomagnetic palaeointensity variations in sediments from Lama Lake, northern Central Siberia. Geophysical Journal International 145, 300–306.

Olsen, N., Mandea, M., 2007. Will the magnetic North Pole move to Siberia? Eos Trans. AGU 88, 293–293.

Olson, P., Deguen, R., 2012. Eccentricity of the geomagnetic dipole caused by lopsided inner core growth. Nature Geoscience 5, 565–569.

Opdyke, M.D., Channell, J.E., 1996. Magnetic stratigraphy. Academic Press.

Opdyke, N.D., Mejia, V., 2004. Earth's magnetic field. Geophysical Monograph Series 145, 315–320.

Oswald, W.W., Anderson, P.M., Brown, T.A., Brubaker, L.B., Feng Sheng Hu, Lozhkin, A.V., Tinner, W., Kaltenrieder, P., 2005. Effects of sample mass and macrofossil type on radiocarbon dating of arctic and boreal lake sediments. Holocene 15, 758–767.

Peck, J., King, J., Colman, S., Kravchinsky, V., 1996. An 84-kyr paleomagnetic record from the sediments of Lake Baikal, Siberia. Journal of geophysical research 101, 11365–11.

Peng, L., King, J.W., 1992. A late Quaternary geomagnetic secular variation record from Lake Waiau, Hawaii, and the question of the Pacific nondipole low. Journal of Geophysical Research: Solid Earth (1978–2012) 97, 4407–4424.

Péwé, T.L., 1955. Origins of the upland silt near Fairbanks, Alaska. Geological Society of America Bulletin 66, 699–724.

Rasmussen, S.O., Andersen, K.K., Svensson, A.M., Steffensen, J.P., Vinther, B.M., Clausen, H.B., Siggaard-Andersen, M.-L., Johnsen, S.J., Larsen, L.B., Dahl-Jensen, D., Bigler, M., Röthlisberger, R., Fischer, H., Goto-Azuma, K., Hansson, M.E., Ruth, U., 2006. A new Greenland ice core chronology for the last glacial termination. J. Geophys. Res. 111, D06102.

Rea, D.K., 1994. The paleoclimatic record provided by eolian deposition in the deep sea: The geologic history of wind. Rev. Geophys. 32, 159–195.

Reimer, P.J., Baillie, M.G.L., Bard, E., Bayliss, A., Beck, J.W., Blackwell, P.G., Ramsey, C.B., Buck, C.E., Burr, G.S., Edwards, R.L., Friedrich, M., Grootes, P.M., Guilderson, T.P., Hajdas, I., Heaton, T.J., Hogg, A.G., Hughen, K.A., Kaiser, K.F., Kromer, B., McCormac, F.G., Manning, S.W., Reimer, R.W., Richards, D.A., Southon, J.R., Talamo, S., Turney, C.S.M., Plicht, J. van der, Weyhenmeyer, C.E., 2011. IntCal09 and Marine09 Radiocarbon Age Calibration Curves, 0-50,000 Years cal BP. Radiocarbon 51, 1111–1150.

Roberts, A.P., Tauxe, L., Heslop, D., 2013. Magnetic paleointensity stratigraphy and high-resolution Quaternary geochronology: successes and future challenges. Quaternary Science Reviews 61, 1–16.

Roberts, P., Scott, S., 2003. On analysis of the secular variation. Magnetohydrodynamics and the Earth's Core: Selected Works of Paul Roberts 10, 15.

Slack, J.F., Dumoulin, J.A., Schmidt, J.M., Young, L.E., Rombach, C.S., 2004. Paleozoic Sedimentary Rocks in the Red Dog Zn-Pb-Ag District and Vicinity, Western Brooks Range, Alaska: Provenance, Deposition, and Metallogenic Significance. Economic Geology 99, 1385–1414.

Snowball, I., Muscheler, R., 2007. Palaeomagnetic intensity data: an Achilles heel of solar activity reconstructions. The Holocene 17, 851–859.

Snowball, I., Sandgrena, P., 2002. Geomagnetic field variations in northern Sweden during the Holocene quantified from varved lake sediments and their implications for cosmogenic nuclide production rates. The Holocene 12, 517–530.

Snowball, I., Zillén, L., Ojala, A., Saarinen, T., Sandgren, P., 2007. FENNOSTACK and FENNORPIS: Varve dated Holocene palaeomagnetic secular variation and relative palaeointensity stacks for Fennoscandia. Earth and Planetary Science Letters 255, 106–116.

St-Onge, G., Mulder, T., Francus, P., Long, B., 2007. Chapter Two Continuous Physical Properties of Cored Marine Sediments. Developments in Marine Geology 1, 63–98.

St-Onge, G., Stoner, J.S., Hillaire-Marcel, C., 2003. Holocene paleomagnetic records from the St. Lawrence Estuary, eastern Canada: centennial- to millennial-scale geomagnetic modulation of cosmogenic isotopes. Earth and Planetary Science Letters 209, 113–130.

St-Onge, G., Stoner, J.S., Hillaire-Marcel, C., 2003. Holocene paleomagnetic records from the St. Lawrence Estuary, eastern Canada: centennial- to millennial-scale geomagnetic modulation of cosmogenic isotopes. Earth and Planetary Science Letters 209, 113–130.

Stober, J.C., Thompson, R., 1979. An investigation into the source of magnetic minerals in some Finnish lake sediments. Earth and Planetary Science Letters 45, 464–474.

Stoner, J.S., Channell, J.E.T., Mazaud, A., Strano, S.E., Xuan, C., 2013. The influence of high latitude flux lobes on the Holocene paleomagnetic record of IODP Site U1305 and the northern North Atlantic. Submitted to Geochemistry, Geophysics, and Geosystems (G-Cubed).

Stoner, J.S., Jennings, A., Kristjánsdóttir, G.B., Dunhill, G., Andrews, J.T., Hardardóttir, J., 2007. A paleomagnetic approach toward refining Holocene radiocarbon-based chronologies: Paleoceanographic records from the north Iceland (MD99-2269) and east Greenland (MD99-2322) margins. Paleoceanography 22.

Stoner, J.S., Laj, C, Channell, J., Kissel, C, 2002. South Atlantic and North Atlantic geomagnetic paleointensity stacks (0–80ka): implications for inter-hemispheric correlation. Quaternary Science Reviews 21, 1141–1151.

Stoner, J.S., St-Onge, G., 2007. Chapter Three Magnetic Stratigraphy in Paleoceanography: Reversals, Excursions, Paleointensity, and Secular Variation. Developments in Marine Geology 1, 99–138.

Strano, S.E., Stoner, J.S., Xuan, C., Marcott, S.A., Almasi, P. (*in prep*), Paleomagnetic acquisition induced Age Offset and smoothing of Deep-sea Sediment.

Stuiver, M. and Polach, H.A., 1977. Discussion: Reporting of 14C data. Radiocarbon, 19:355-363.

Stuiver, M., Reimer, P. J., and Reimer, R. W. 2005. CALIB 5.0. [program and documentation]. http://calib.qub.ac.uk/calib/

Tauxe, L., 1993. Sedimentary records of relative paleointensity of the geomagnetic field: theory and practice. Reviews of geophysics 31, 319–354.

Tauxe, L., Butler, R.F., Van der Voo, R., Banerjee, S.K., 2010. Essentials of paleomagnetism. University of California Press.

Tegen, I., Lacis, A.A., Fung, I., 1996. The influence on climate forcing of mineral aerosols from disturbed soils. Nature 380, 419–422.

Thellier, E., Thellier, O., 1959. Sur l'intensité du champ magnétique terrestre dans le passé historique et géologique. [s.n.], Lille.

Thompson, R. 1984: A global review of paleomagnetic results from wet lake sediments. Pg. 145-164 in Haworth, E. Y. & Lund, J. W. G. (eds.): Lake Sediments and Environmental History. University of Minnesota Press, Minneapolis.

Thompson, R., Oldfield, F., 1986. Environmental Magnetism. Allen & Unwin.

Turner, G.M., Turner, G., Thompson, R., 1981. Lake sediment record of the geomagnetic secular variation in Britain during Holocene times. Geophysical Journal International 65, 703–725.

Valet, J., 2003. Time variations in geomagnetic intensity. Reviews of Geophysics 41.

Verosub, K.L., 1977. Depositional and postdepositional processes in the magnetization of sediments. Reviews of Geophysics 15, 129–143.

Verosub, K.L., Mehringer, P.J., Waterstraat, P., 1986. Holocene secular variation in western North America: Paleomagnetic record from Fish Lake, Harney County, Oregon. J. Geophys. Res. 91, 3609–3623.

Viau, A.E., Gajewski, K., Sawada, M.C., Bunbury, J., 2008. Low- and high-frequency climate variability in eastern Beringia during the past 25 000 years. Canadian Journal of Earth Sciences 45, 1435–1453.

Vlag, P.A., Oches, E.A., Banerjee, S.K., Solheid, P.A., 1999. The paleoenvironmental-magnetic record of the Gold Hill Steps loess section in central Alaska. Physics and Chemistry of the Earth, Part A: Solid Earth and Geodesy 24, 779–783.

Wooller, M., Kurek, J., Gaglioti, B., Cwynar, L., Bigelow, N., Reuther, J., Gelvin-Reymiller, C., Smol, J., 2012. An ~11,200 year paleolimnological perspective for emerging archaeological findings at Quartz Lake, Alaska. J Paleolimnol 48, 83–99.

Xuan, C., Channell, J.E.T., 2009. UPmag: MATLAB software for viewing and processing u channel or other pass-through paleomagnetic data. Geochem. Geophys. Geosyst. 10, Q10Y07.

Xuan, C., Stoner, J.S., Mix, A.C., VanLaningham, S., (*in prep*). Northeast Pacific geomagnetic and environmental change during the last 140 kyr recorded by deep-sea sediment core EW9504-17PC.

APPENDIX

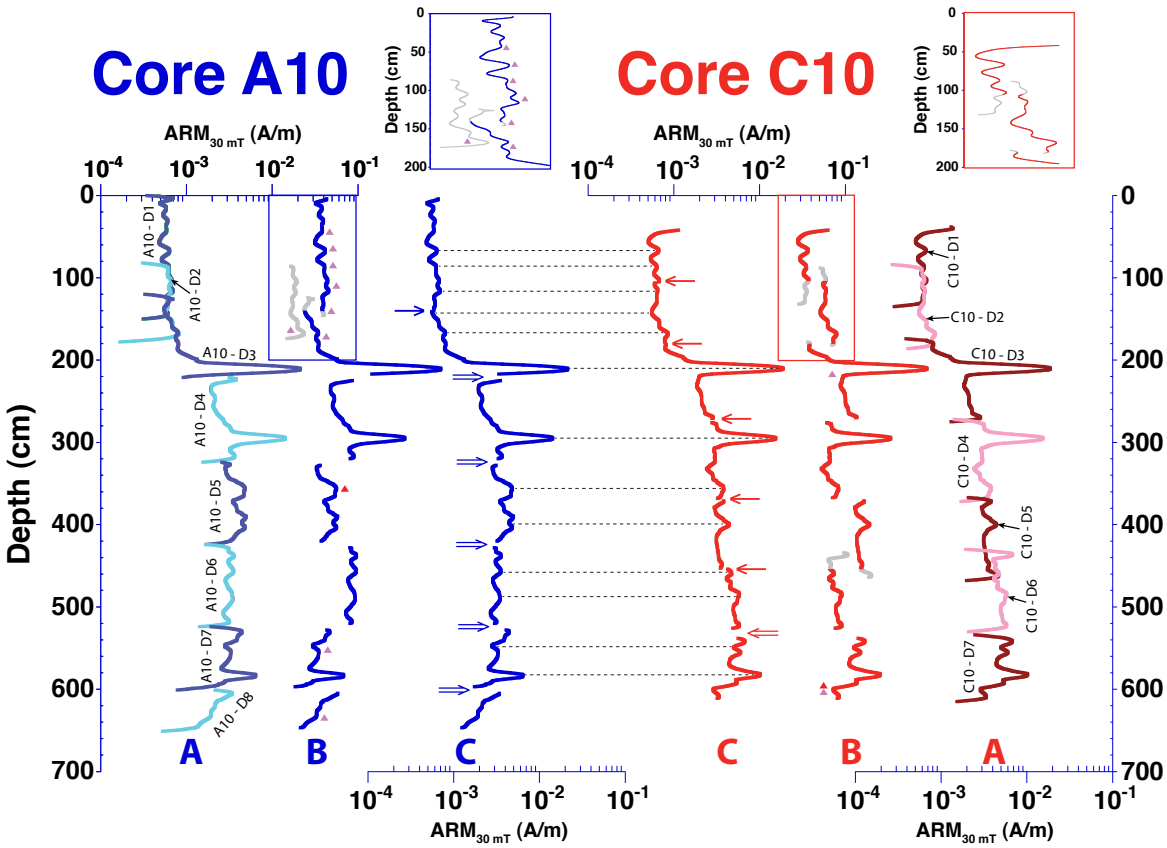

Appendix A – A10/C10 stratigraphic comparison and composite depth scale construction diagram. ARM_{30mT} values are plotted for cores A10 (**left side**) and C10 (**right side**) demonstrating their stratigraphic correlation on a common depth scale after C10 drives were "hung" to match the A10 record. Note, values are plotted on a log scale. **A)** Data for individual drives are shown in alternating colors, including magnetometer edge effects. **B)** Edge effects are removed and drives are offset to better show the alignment of features between overlapping drives. Grey segments show the drives or portions of drives that were not used in the final composite record of each core. Insets are shown for the upper 200 cm of each core (blue and red boxes), with values scaled to show variance. Locations of radiocarbon dates are shown, with pink triangles corresponding to accepted ages and red triangles corresponding to rejected ages (see Chapters 2 and 3 for a discussion of the Burial Lake radiocarbon chronology). **C)** Data are recompiled to show the final composite record of each core. Locations of section breaks are shown for overlapping sections (→) and for sections that are either abutted or contain a data gap (⇒). Tie points show the agreement of features between the final composite versions of each core. Note, the final C10 composite record is not utilized in this report, and we mainly focus on results from the 6.51 m A10 core. The stratigraphic correlation does however allow us to incorporate C10 radiocarbon dates in the age-depth model for the A10 core.